



Norwegian University of
Science and Technology

Numerical modeling of pool spreading, heat transfer and evaporation in liquefied natural gas (LNG)

Øystein Myrmo

Master of Science in Energy and Environment

Submission date: June 2011

Supervisor: Ivar Ståle Ertesvåg, EPT

Co-supervisor: Rune Natten Kleiveland, ComputIT AS

Nils Inge Lilleheie, ComputIT AS

Kjell Erik Rian, ComputIT AS

Norwegian University of Science and Technology
Department of Energy and Process Engineering

MASTEROPPGAVE

for
Øystein Myrmo

Våren 2011

Numerisk modellering av dam-spredning, varmeoverføring og fordamping i flytende naturgass (LNG)

*Numerical modeling of pool spreading, heat transfer and evaporation
in liquefied natural gas (LNG)*

Bakgrunn og formål

Ved NTNUs Institutt for energi- og prosesssteknikk har det i en årrekke vært arbeidet med matematisk modellering og numerisk simulering av turbulent strømming og forbrenning. Metodene og modellene som er utviklet gjennom denne forskningsaktiviteten, har blitt anvendt på en rekke industrielle problemstillinger.

For å kunne beregne brann så realistisk og nøyaktig som mulig er det nødvendig med detaljert kunnskap om de fysiske og kjemiske prosessene som opptrer. Videre må en ha gode modeller for disse prosessene og for sammenhengen mellom dem.

I forbindelse med instituttets og ComputIT AS sitt engasjement innenfor sikkerhetsrelatert forbrenningsteknikk, ønsker vi gjennom dette prosjektet å studere matematiske modeller for de ulike fysiske og kjemiske fenomenene som opptrer ved utslipp og forbrenning av LNG. Oppgaven er en videreføring av masteroppgaven høsten 2010.

Oppgaven bearbeides ut fra følgende punkter:

- Videre litteraturstudium omkring varmeoverføring, fordamping/koking og dam-spredning. Varmeutveksling ved faseovergang for blandinger er særlig relevant.
- Vurdere numerisk vertøy (program) for å beregne spredning og fordamping av LNG-dammer. Sette seg inn i og presentere det valgte programet.
- Gjennomføre beregninger av spredning og fordamping basert på eksisterende modeller, og prøve ut nye/modifiserte modeller. Diskutere resultatene.
- Diskutere eventuelle forbedringer av de matematiske modellene for spredning og fordamping av LNG.

En fremdriftsplan (*Planlagte aktiviteter med tidsplan for fremdrift*) for hele oppgaven skal forelegges faglærer/veileder(e) for kommentarer innen 14 dager etter utlevering av oppgaveteksten.

Besvarelsen redigeres mest mulig som en forskningsrapport med innholdsfortegnelse, et sammendrag på norsk, konklusjon, litteraturliste, etc. Ved utarbeidelsen av teksten skal kandidaten legge vekt på å gjøre teksten oversiktlig og velkrevet. Med henblikk på lesing av besvarelsen er det viktig at de nødvendige henvisninger for korresponderende steder i tekst, tabeller og figurer anføres på begge steder. Ved bedømmelsen legges det stor vekt på at resultatene er grundig bearbeidet, og at de oppstilles tabellarisk og/eller grafisk på en oversiktlig måte og diskuteres utførlig.

Det forutsettes at kandidaten på eget initiativ etablerer et tilfredsstillende kontaktforhold med faglærer og veileder(e).

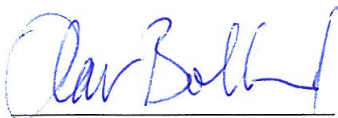
Kandidaten skal rette seg etter arbeidsreglement ved ComputIT AS, samt etter eventuelt andre pålegg fra den ansvarlige ledelse. Det tillates ikke at kandidaten griper inn i betjeningen av anlegg, installasjoner og lignende uten etter avtale med ansvarshavende.

I henhold til ”Utfyllende regler til studieforskriften for teknologistudiet/sivilingeniørstudiet” ved NTNU § 20, forbeholder instituttet seg retten til å benytte alle resultater i undervisnings- og forskningsformål, samt til publikasjoner.

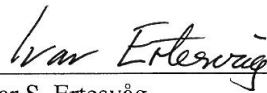
Sluttrapport for oppgaven skal leveres innbundet i 3 komplette eksemplarer med et ”løsblad” med konsentrert sammendrag med forfatternavn og oppgavetittel for eventuell referering i tidsskrifter (maksimalt én maskinskrevet side med dobbel linjeavstand. Ytterligere kopier av rapporten til evt. medveileder(e)/kontaktpersoner skal avtales med, og evt. leveres direkte til, de respektive. Til faglærer/instituttet innleveres også en komplett kopi på CD-ROM i Word-format eller tilsvarende.

Sluttrapporten skal innleveres til Instituttet *innen 14. juni 2011*.

Institutt for energi- og prosesssteknikk, 17. januar 2011



Olav Bolland
Instituttleder



Ivar S. Ertesvåg
Faglærer/veileder

Medveiledere/kontaktpersoner:
Kjell Erik Rian, ComputIT AS
Rune Kleiveland, ComputIT AS
Nils Inge Lilleheie, ComputIT AS

Preface

This master's thesis ends my five years at Energy and Environmental Engineering at NTNU and in total nineteen years of education. The thesis is written in collaboration with the Department of Energy and Process Engineering at NTNU and Computational Industry Technologies AS (ComputIT).

There is really no end to such work, in the sense that every time you do an analysis you end up with several new and exciting results to follow up. Because of this, things never turn out quite as you expected and it is more clear at the end what should have been done and what should not. The endless amount of interesting work you want to do, which you do not have the time for, can sometimes be overwhelming. Nevertheless, such experiences are part of my education and they are likely to prove good lessons for future work.

I would like to thank my supervisors, both Ivar Ståle Ertesvåg at NTNU and Nils Inge Lilleheie, Kjell Erik Rian and Rune Natten Kleiveland at ComputIT. You have opened a new world in computing to me through your Linux skills, Nils Inge, and given me insights that will undoubtedly prove useful in the future. Your knowledge of what is expected from theses like this has really been invaluable, Kjell Erik. It has also been great to have you, Rune, as a mentor for the physical understanding of the problems I have run into through the year I have worked here.

A special thank goes to Tarjei Bærland for our interesting, yet somewhat heated, discussions at ComputIT when working late hours. Fortunately, I won them all.

Trondheim, June 12, 2011



Øystein Myrmo

Abstract

This master's thesis is a continuation of previous theses written at ComputIT AS. It treats heat transfer to LNG pools boiling on water through two heat transfer models, LNGSIM1 and LNGSIM2. LNGSIM1 utilizes heat transfer correlations for pure liquids in combination with physical data of the mixture, while LNGSIM2 uses LNGSIM1 and a simple model for the concentration boundary layer.

Both models are implemented in the CFD software Kameleon FireEx (KFX) and thereafter tested and validated against experimental data from the Burro test series. Comparisons with experimental data show that LNGSIM1 often produces correct trends in the downstream gas concentrations. The results are, however, often shifted in time, indicating that the heat transfer in the beginning of the spill is too low. LNGSIM2 is constructed to increase the heat transfer compared to LNGSIM1, hence vaporizing the LNG faster to better fit the experimental data in time. The choice of the constant C_{SIM2} in LNGSIM2 greatly affects the heat transfer, and it is found to fit experimental data best for $0.70 < C_{\text{SIM2}} < 0.80$.

An attempt to approximate LNG as pure methane produced erroneous results due to the heat flux remaining constant throughout the spill. Another attempted approximation was the use of a constant heat transfer coefficient. This produced very low heat fluxes towards the end of the spill, making it impossible for the gas concentrations to reach a zero value within the experimental time interval. The use of these simplifications are therefore not advised.

A study of rapid phase transitions (RPT) is conducted using a simple criterion for when an RPT can occur. Comparison with a theoretical study gives promising results for describing when, where and why an RPT occur. This can be used to estimate when to release the pressure wave of an RPT.

Investigations of the pool boiling correlations for pure liquids conclude that the way of calculating the transition boiling regime results in too high heat fluxes in that regime. To address this, a parameter study using LNGSIM1 and a factor ζ is performed in order to reduce the transition boiling heat fluxes. The optimum values of ζ are thereafter combined with the optimum values of C_{SIM2} .

Combining ζ and C_{SIM2} reveals that most of the investigated values of ζ overrides the wanted effect of C_{SIM2} , hence warranting new approaches to reduce the overestimated transition boiling heat fluxes. Nevertheless, LNGSIM1 and LNGSIM2 with $0.70 < C_{\text{SIM2}} < 1.00$ appear to be good alternatives to the current heat transfer model in KFX, since the heat transfer coefficient is continuously calculated based on compositions and boiling regimes, whereas the KFX model requires a constant heat transfer coefficient as input.

Sammendrag

Denne masteroppgaven er en fortsettelse av tidligere oppgaver skrevet hos ComputIT AS. Den omhandler varmeoverføring til LNG som koker på vann gjennom to modeller, LNGSIM1 og LNGSIM2. LNGSIM1 bruker korrelasjoner for varmeoverføring ved koking av rene stoffer med fysiske data for blandingen, mens LNGSIM2 bruker LNGSIM1 og en enkel modell for konsentrasjonsgrensesjiktet.

Begge modellene er implementert i CFD-programvaren Kameleon FireEx og deretter testet og validert mot eksperimentaldata fra testserien Burro. Sammenligning med eksperimentaldata viser at LNGSIM1 ofte gir riktige trender i gasskonsentrasjonene nedstrøms, men resultatene er ofte forflyttet i tid. Dette indikerer at varmeoverføringen i begynnelsen av utslippet er for lav. LNGSIM2 er laget for å øke varmeoverføringen i forhold til LNGSIM1, for på den måten å fordampe LNG-et raskere slik at gasskonsentrasjonene passer tidsmessig bedre med eksperimentaldata. Valget av konstanten C_{SIM2} i LNGSIM2 påvirker varmeoverføringen i stor grad. Denne passer eksperimentaldata best for $0.70 < C_{SIM2} < 0.80$.

Et forsøk på å tilnærme LNG som rent metan ga feilaktige svar på grunn av at varmekraften holdt seg konstant gjennom hele utslippet. En annen tilnærming var å bruke et konstant varmeovergangstall. Dette ga veldig lave varmekraft mot slutten av utslippet, noe som gjorde det umulig for gasskonsentrasjonene å nå en nullverdi innenfor eksperimentaldatens tidsintervall. Bruken av disse forenklingene er derfor ikke anbefalt.

Et studie av rask faseovergang (RPT) er utført ved bruk av et enkelt kriterium for når en RPT kan oppstå. Sammenligning med et annet teoretisk studie gir lovende resultater for å beskrive når, hvor og hvorfor en RPT oppstår. Dette kan bli brukt til å estimere når trykkbølgen fra en RPT kan slippes løs.

Undersøkelser av korrelasjonene for koking av rene stoffer konkluderer med at måten å regne ut overgangsregimet på resulterer i for høye varmekraft i det regimet. For å ta hensyn til dette er et parameterstudie av LNGSIM1 med en faktor ζ gjennomført for å redusere varmekraftene i overgangsregimet. De optimale verdiene av ζ er deretter kombinert med de optimale verdiene for C_{SIM2} .

Kombinasjonen av ζ og C_{SIM2} avslører at de fleste undersøkte verdiene av ζ overstyrer den ønskede effekten av C_{SIM2} . Dette gir behov for nye måter å redusere de overestimerte varmekraftene i overgangsregimet. Den nåværende varmeoverføringsmodellen i KFX trenger et konstant varmeovergangstall som input. LNGSIM1 og LNGSIM2 med $0.70 < C_{SIM2} < 1.00$ later derfor til å være gode alternativer til denne, siden disse beregner varmeovergangstallet kontinuerlig basert på sammensetninger og kokeregimer.

Contents

Preface	V
Abstract	VII
Sammendrag	IX
Contents	XI
Nomenclature	XV
1 Introduction	1
1.1 Motivation	1
1.2 Limitations and restrictions	1
1.3 Report outline	2
2 Definitions and basic physics	3
2.1 Introduction	3
2.2 Heat transfer	4
2.3 Boiling regimes	6
2.4 Mass transfer	10
2.5 Liquid-vapor equilibrium	10
2.6 Ice and hydrate formation	12
2.7 Definitions of non-dimensional quantities	13
2.8 General transport equations	15
2.9 Models in KFX	15
2.10 Numerics in KFX	18
3 Validation of pool boiling correlations	21
3.1 Heat transfer calculations	21
3.2 Comparison with experimental data for pure liquids	27
3.3 Comparison with experimental data for mixtures	32
3.4 Summary and conclusions	33

4	Boiling of mixtures	35
4.1	Properties in boiling of mixtures	35
4.2	Nucleate boiling of mixtures	37
4.3	Film boiling of mixtures	39
4.4	Transition boiling of mixtures	41
4.5	Rapid phase transitions	42
5	Pool boiling heat transfer models	45
5.1	LNGSIM1	45
5.2	LNGSIM2	45
6	Spreading of cryogenic liquid on water	49
6.1	The Shallow Water Equations	49
7	Simulations	53
7.1	The Burro test series	53
7.2	Setting up the Burro case	54
7.3	Burro 8	55
7.4	Simulations using LNGSIM1	56
7.5	Simulations using LNGSIM2	60
7.6	Effect of changing the transition boiling heat flux	63
7.7	Rapid phase transitions	66
7.8	Pool area and evaporation rate	69
7.9	Sensitivity analyses	71
7.10	Optimizing the heat transfer model	78
8	Conclusions and further work	81
8.1	Conclusions	81
8.2	Further work	83
	References	84
	Appendices:	89
A	Heat transfer correlations for pool boiling of pure liquids	89
A.1	Nucleate boiling heat transfer	89
A.2	Critical heat flux	90
A.3	Transition boiling heat transfer	90
A.4	Minimum heat flux	91
A.5	Film boiling heat transfer	92
B	Physical properties of selected fluids at T_{boil}	95
B.1	Physical properties of methane	96
B.2	Physical properties of ethane	97
B.3	Physical properties of propane	98
B.4	Physical properties of butane	99
B.5	Physical properties of the vapor film	100

C	Thermodynamic properties of mixtures	101
C.1	Thermodynamic properties of liquid mixtures	101
C.2	Thermodynamic properties of vapor mixtures	102

Nomenclature

Abbreviations

CFD	Computational Fluid Dynamics
EDC	Eddy Dissipation Concept
KFX	Kameleon FireEx
LFL	Lower flammability limit
LNG	Liquefied Natural Gas
NIST	National Institute of Standards and Technology
PDE	Partial Differential Equation
RPT	Rapid Phase Transition
UFL	Upper flammability limit

Greek symbols

α	Thermal diffusivity = $\frac{K}{\rho c_p}$	(m ² /s)
α_e	Equivalent thermal diffusivity = $\frac{K_v \Delta T_w}{2h_{ig} \rho_v}$	(m ² /s)
α_{rel}	Relative volatility	(-)
β	Coefficient of volume expansion (= $1/T$ for perfect gas)	(1/K)
Γ	General diffusion coefficient	(-)
γ	Surface-liquid interaction parameter = $\sqrt{(k_w \rho_w c_{pw}) / (k_l \rho_l c_{pl})}$	(-)
δ_{ij}	Kronecker delta	(-)
ε	Dissipation rate of mean turbulence energy	(m ² /s ³)
ζ	Exponent in transition boiling, Eq. (7.1)	(-)
λ_{crit}	Critical wave length = $2\pi B$	(m)
μ	Dynamic viscosity = $\rho\nu$	(kg/ms)

μ_{eff}	Effective diffusion coefficient = $\mu + \mu_{\text{turb}}$	(kg/ms)
ν	Kinematic viscosity	(m ² /s)
ξ	Fraction of cold liquid in contact with the hot surface	(-)
ρ	Mass density	(kg/m ³)
σ	Surface tension	(N/m)
σ_ε	Turbulent Prandtl number for ε (= 1.3)	(-)
σ_k	Turbulent Prandtl number for k (= 1.0)	(-)
σ_ρ	Turbulent Prandtl number for the buoyancy term (= 0.7)	(-)
σ_{SB}	Stefan-Boltzmann's constant = $5.670 \cdot 10^{-8}$	(W/m ² K ⁴)
τ	Viscous drag between ground/pool and air/pool	(-)
ϕ	General quantity	(-)

Roman symbols

$\partial b/\partial x$	Slope of ground in x-direction	(-)
$\partial b/\partial y$	Slope of ground in y-direction	(-)
A	Area	(m ²)
a	Acceleration	(m/s ²)
Ar	Archimedes number	(-)
B	Laplace's reference length = $\sqrt{\frac{\sigma}{g(\rho_l - \rho_v)}}$	(-)
Bu	Buoyancy term	(-)
Bo_{mix}^*	Properties profile parameter = $\rho_l R_a^2 g / \sigma$	(-)
C	Courant number	(-)
$C_{\varepsilon,i}$	Model constants in the the k - ε model	(-)
c_p	Specific heat capacity	(J/kgK)
C_{SIM2}	Factor used for the concentration boundary layer in LINGSIM2	(-)
$C_{\text{vp},1}$	Constant in Eq. (2.16)	(-)
$C_{\text{vp},2}$	Constant in Eq. (2.16)	(K)
\bar{D}	Determinant of Fick matrix of diffusion coefficients	(m ⁴ /s ²)
d	Diameter	(m)

D_{AB}	Diffusion coefficient of the species in a binary mixture	(m ² /s)
E	Emissivity	(-)
\tilde{f}_i	Body forces	(-)
F_{ij}	Flux tensor	(-)
f_1	General function for latent heat in Eq. (A.27)	(-)
f_2	General function for latent heat in Eq. (A.29)	(-)
$f_{\varepsilon i}$	Low Reynolds number corrections in the k - ε model	(-)
g	Gravitational acceleration	(m/s ²)
Ga	Galileo number = $\frac{g\lambda_{\text{crit}}^3}{\nu^2}$	(-)
Gr	Grashof number (= $\frac{g\beta(T_s - T_b)L^3}{\nu^2}$)	(1/K)
Gr*	Generalized Grashof number = $\frac{g\rho_v^2 L^3}{\mu_v^2} \frac{\rho_l - \rho_v}{\rho_v}$	(-)
h	Heat transfer coefficient	(W/m ² K)
h_{fg}	Latent heat of vaporization (formation of gas from liquid)	(kJ/kg)
h'_{fg}	Modified heat of vaporization = $h_{\text{fg}} + 0.5c_{pv}\Delta T_w$	(kJ/kg)
h''_{fg}	Modified heat of vaporization = $h_{\text{fg}} + \frac{19}{20}c_{pv}\Delta T_w$	(kJ/kg)
j_ϕ	Diffusive transport of the general quantity ϕ	(-)
Ja_m	Modified Jakob number = $(\rho_l c_{pl} \Delta T_{\text{eff}} / \rho_v h_{\text{fg}})$	(-)
K	Thermal conductivity	(W/mK)
k	Turbulence energy = $0.5\tilde{u}_i''^2$	(J/kg)
L	Characteristic length scale	(m)
M	Molar weight	(kg/kmol)
m''	Mass per area of liquid pool	(kg/m ²)
\dot{m}	Mass flow	(kg/s)
\dot{m}''_{vap}	Mass evaporated per area of liquid pool	(kg/m ² s)
\dot{m}_{vap}	Mass evaporated from liquid pool	(kg/s)
n	Arbitrary direction (x, y, z or r)	(m)
n_s	Number of species in a mixture	(-)

Nu	Nusselt number	(-)
P	Production term	(-)
p	Pressure	(N/m ²)
p_i	Partial pressure of component i	(Pa)
Pr	Prandtl number = $\frac{\mu c_p}{K}$	(-)
Pr^*	Generalized Prandtl number = $\frac{\nu_v}{\alpha_e}$	(-)
R	Radius	(m)
r	Length in r-direction	(m)
Ra	Rayleigh number $GrPr = \frac{g\beta(T_s - T_b)L^3}{\nu^2} Pr$	(-)
R_a	Centre line average	(m)
R_u	Gas constant	(kJ/kgK)
S_i	Source term in Eqs. (6.1) and (6.3)	(-)
T	Temperature	(K)
T^*	Dew point temperature	(K)
ΔT^*	Dimensionless temperature in Eq. (A.11)	(-)
q	Field variable vector	(-)
\dot{q}	Heat flux	(W/m ²)
\dot{Q}_{cond}	Conductive heat	(W)
\dot{q}_{cond}	Conductive heat flux	(W/m ²)
\dot{Q}_{conv}	Convective heat	(W)
\dot{q}_{conv}	Convective heat flux	(W/m ²)
\dot{q}_{rad}	Radiative heat flux	(W/m ²)
u	Velocity	(m/s)
u'	Reynolds fluctuation in velocity	(m/s)
u''	Favre fluctuation in velocity	(m/s)
\bar{u}	Reynolds averaged velocity	(m/s)
\tilde{u}	Favre averaged velocity = $\overline{\rho u''} / \bar{\rho}$	(m/s)
v	Specific volume	(m ³ /kg)

X	Mole fraction in the liquid phase	(-)
x	Length in x-direction	(m)
X'	Mass fraction in liquid phase	(-)
X^*	Equilibrium mole fraction in the liquid phase	(-)
X'^*	Equilibrium mass fraction in the liquid phase	(-)
Y	Mole fraction in the vapor phase	(-)
y	Length in y-direction	(m)
Y'	Mass fraction in vapor phase	(-)
Y^*	Equilibrium mole fraction in the vapor phase	(-)
Y'^*	Equilibrium mass fraction in the vapor phase	(-)
z	Length in z-direction	(m)

Subscripts and superscripts

1	Most volatile component in a binary mixture
2	Least volatile component in a binary mixture
*	Equilibrium
AB	Diffusion between component A and B
amb	Ambience
atm	Atmospheric pressure = 1.01325 bar
boil	Boiling point
cond	Conduction
conv	Convection
crit	Critical wave length
cr	Critical (maximum) heat flux
diff	Diffusion
eff	Effective diffusion coefficient
eff	Effective temperature difference for mixtures
mass	Mass diffusion
min	Minimum (Leidenfrost) heat flux

<i>mix</i>	Mixture
<i>rad</i>	Radiation
<i>SL</i>	Superheat limit (thermodynamic stability limit)
<i>turb</i>	Turbulence quantity
<i>vap</i>	Vaporization
<i>vf</i>	Vapor film at arithmetic mean between saturated liquid and wall
<i>vp</i>	Vapor pressure
ϕ	Transportation of the general quantity ϕ
σ	Reduced temperature in Eq. (B.1)
<i>c</i>	Critical point (triple point)
<i>f</i>	Film boiling
<i>I</i>	Interface between vapor film and liquid or hot surface and liquid
<i>i</i>	Component <i>i</i>
<i>j</i>	Component <i>j</i>
<i>k</i>	Component <i>k</i>
<i>l</i>	Liquid
<i>m</i>	Field variable number <i>m</i>
<i>n</i>	Nucleate boiling
<i>p</i>	Center position of a control volume
<i>s</i>	Saturated
<i>t</i>	Transition boiling
<i>v</i>	Vapor
<i>w</i>	Wall or water
<i>x</i>	Value decomposed in the x-direction
<i>y</i>	Value decomposed in the y-direction

1 Introduction

The world's need for energy is steadily increasing as the population grows and more people are improving their standard of living. Recent events like the disaster in Japan have also turned our focus towards other sources of energy, LNG being a frequently mentioned partial solution to the increasing energy demand.

1.1 Motivation

When handling LNG in any way, lots of hazardous situations may arise if it is accidentally spilled into the ambience. The LNG's cold nature might cause severe tissue damage to people and constructions or embrittlement to materials and ship hull. As the LNG meets the ambience it will start to boil and evaporate, thereby threatening humans and wildlife with asphyxiation. The evaporated LNG can also be ignited, possibly causing explosions, fireballs and pool fires. To be able to predict hazards from LNG spills it is therefore imperative to know the evaporation rate of the LNG, and thus also the heat transfer from the surroundings.

In the event of no ignition, the LNG will continue to evaporate, and after some time, rapid phase transitions (RPTs) are known to occur. These RPTs release high pressure waves up to a maximum of 36 bars [1] and are therefore often referred to as mechanical or physical explosions, as they are not combustion related. If an RPT occurs it will greatly change the distance to the LFL and the UFL and thereby greatly increase the likelihood of any hazardous situation.

Large-scale experiments of pool boiling of LNG on water are both expensive and threatening to the environment. Therefore, it might rather be better to spend the resources on mathematical modeling and simulations of the events. To be able to predict the hazards correctly, however, one needs mathematical models that fits experimental data adequately. This thesis is an attempt to construct a pool boiling heat transfer model that fits experimental data from the Burro test series.

1.2 Limitations and restrictions

This work assumes no ice formation and constant water temperature when LNG is spilled onto water. These assumptions will create relatively small errors if there are large amounts of water present, due to natural convection currents within the water. The discussion is also limited to spills on an unconfined water surface regarding the previous assumptions. Furthermore, it is assumed that the water surface can be treated as a horizontal wall (i.e. there are no waves, currents etc.

in the water). If the text does not state otherwise, the discussion is always about pool boiling of LNG upon water. Other phenomena that would disturb the LNG pool, for example pool fires and explosions, are also disregarded.

1.3 Report outline

Chapter 2 introduces relevant background theory and important physical parameters and concepts used throughout the entire text. In Ch. 3, an in-depth study of the pool boiling heat transfer correlations for pure liquids found in a previous study [2] is performed. Ch. 4 extends the discussion to multicomponent boiling and RPTs before Ch. 5 introduces the two heat transfer models, LNGSIM1 and LNGSIM2. In Ch. 6, the pool spreading model incorporated in KFX is presented. Ch. 7 discusses simulations conducted with LNGSIM1 and LNGSIM2, using the conclusions from Ch. 3, and compares the results with experimental data from the Burro test series. Conclusions and suggestions for future work are presented in Ch. 8.

Appendix A lists the pool boiling correlations for pure liquids found in a previous study [2]. These correlations found the basis of the discussions in Chs. 3, 5 and 7. In App. B, physical properties of the hydrocarbons used in the calculations in Ch. 3 are listed, while App. C lists the correlations used to calculate the mixture properties of LNG in LNGSIM1 and LNGSIM2.

2 Definitions and basic physics

This chapter treats some of the basic topics needed to understand the physics in pool boiling of a cryogenic liquid on water. Some relations from the CFD software KFX, which are used to conduct the simulations in Ch. 7, are given in Secs. 2.9 and 2.10.

2.1 Introduction

Figure 2.1 shows the qualitative overview of heat transfer to a cryogenic liquid pool resting upon water. \dot{q}_{conv} represents the net convective heat flux to the cryogenic liquid from the interaction between the air and the cryogen (wind) and between the water and the cryogen (waves, currents and pool spreading). \dot{q}_{rad} represents the net radiative heat flux to the cryogenic liquid from the sun, possible fires or other sources. Conductive heat transfer internally in the cryogen, \dot{q}_{cond} , will also be present in pool boiling of a mixture whereas in pool boiling of a pure substance it will not (see Ch. 4). All of these heat transfer mechanisms contribute to the evaporation rate, \dot{m}_{vap} , but the heat transfer from the water is by far the most important one, unless another source of radiation (e.g. a fire) is present [3].

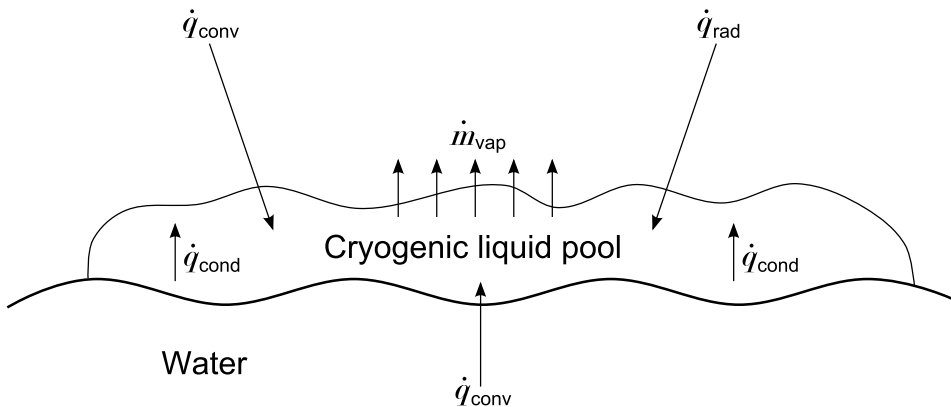


Figure 2.1: Qualitative overview of the heat transfer mechanisms to and mass evaporation in a cryogenic liquid pool resting upon water.

2.2 Heat transfer

There are several physical mechanisms transporting energy as heat, namely heat conduction, heat convection and heat radiation. These mechanisms can work together or by themselves, depending on the physical problem.

2.2.1 Heat conduction

If temperature gradients exist in a solid material or a stagnant fluid, heat will be transferred by conduction from areas with relatively high temperatures to areas with relatively low temperatures. The energy transfer will continue until thermal equilibrium and isothermal state is achieved in the medium considered. This is often referred to as the zeroth law of thermodynamics. Temperature differences are the driving force for heat conduction, and the larger the temperature differences, the larger the heat flux. The fundamental law describing conductive heat transfer is Fourier's law, given as [4]

$$\dot{Q}_{\text{cond}} = -KA \frac{\partial T}{\partial n} = -KA \frac{\Delta T}{L} \quad (2.1)$$

or

$$\dot{q}_{\text{cond}} = -K \frac{\partial T}{\partial n} = -K \frac{\Delta T}{L}. \quad (2.2)$$

In Eqs. (2.1) and (2.2) n is an arbitrary direction in which heat is transferred. The thermal conductivity, K , is a property of the medium involved, which can be regarded as a heat resistance coefficient (small values of K insulate while large values increase the conductive heat transfer). The minus sign is present describe that heat is transferred from high temperature zones to low temperature zones. In monoatomic gases, K is proportional to the square root of the temperature ($K \sim T^{0.5}$) [5], while for pure liquids near or below their normal boiling points, K decreases linearly with increasing temperature ($K \sim T$) [6].

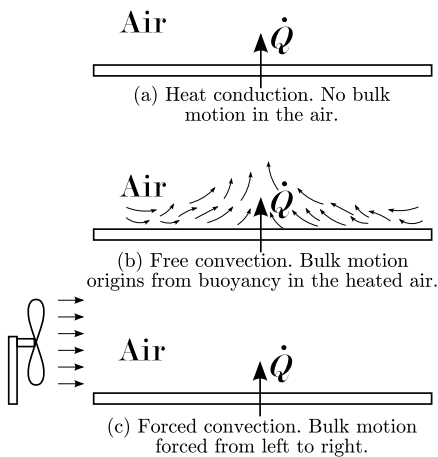


Figure 2.2: Basic heat transfer mechanisms. Heat is transferred through a plate into air at different conditions.

However, as the air is heated, density gradients are established, hence forcing a bulk motion in the fluid, a physical phenomenon called natural convection.

Figure 2.2a shows conduction of heat through stagnant air. The conductive heat transfer will continue for as long as the air is kept totally still.

2.2.2 Heat convection

Heat is always transferred by conduction in solid materials and stagnant fluids. When a bulk fluid motion is present, however, it will bring warmer and cooler parts together, effectively enhancing the heat transfer by replacing regions of heated fluid with fresh, cool one. The fluid motion can be natural due to density differences and buoyancy in the heated fluid as seen in Fig. 2.2b (free convection) or forced by an external device as seen in Fig. 2.2c (forced convection). Forced convection is frequently applied in process equipment like heat exchangers and boilers or in central heating and air conditioning in buildings. Examples of natural convection are the air near a burning candle rising or the water in a lake circulating because of density differences.

In the case of an LNG pool boiling on water there is no forced convection except for possible winds, but some natural convection effects are present. For example, the water will cool and drop downwards as it loses heat to the cold LNG. This effect allows for higher heat transfer to the cryogenic liquid pool by constantly removing cold water and introducing warmer water instead. If there is a small amount of water below the cryogenic liquid pool, however, there is little space for these effects and the water temperature may drop below the freezing point and create an ice shield (see Sec. 2.6).

The governing equation of heat convection is Newton's law of cooling, written as [4]

$$\dot{Q}_{\text{conv}} = hA(T_w - T_l) = hA\Delta T \quad (2.3)$$

or

$$\dot{q}_{\text{conv}} = h(T_w - T_l) = h\Delta T. \quad (2.4)$$

In the same manner as in heat conduction, temperature differences are the driving force in heat convection. Analogous to the thermal conductivity K in Eqs. (2.1) and (2.2), h is the heat transfer coefficient for cases involving convection. h is not as trivial to determine as K , however, as it is dependent on several fluid properties as well as flow properties and boiling regime.

Determining the heat transfer coefficient is one of the main problems in pool boiling of LNG. If h is known, the heat transfer to the liquid pool is also known and thus the vaporization rate and mass loss from the pool are known as well. This enables us to assess other hazardous situations in more detail.

2.2.3 Heat radiation

Radiative heat transfer is fundamentally different from heat conduction and heat convection, but the driving force is still temperature differences. If a hot object is suspended in an evacuated room with walls colder than the object itself, it will still transfer heat to the walls even though heat conduction and heat convection is impossible. The heat is rather transferred through energetic waves or particles.

The maximum rate of radiative heat an object can emit is given by Stefan-Boltzmann's law [4],

$$\dot{q}_{\text{rad}} = \sigma_{\text{SB}}T^4, \quad (2.5)$$

which describes the so-called blackbody radiation from the object under consideration. All real surfaces emit less than the blackbody radiation heat flux, which is described by the emissivity E as [4]

$$\dot{q}_{\text{rad}} = E\sigma_{\text{SB}}T^4. \quad (2.6)$$

The emissivity of an object, be it a gas, a liquid or a solid surface, is heavily dependent on the surface material or fluid properties and is therefore non-trivial to determine. If a model for the emissivity exists, however, it is easy to determine the radiative heat transfer by using Eq. (2.6).

Every object and medium are always emitting radiative heat to some extent, though there is not necessarily a net emission from an object. This is also true for both an LNG pool and the LNG vapor above it; they exchange heat with each other, the sky, the sun, the water and so forth. The LNG vapor might in fact shield the LNG pool from radiation from the sun or a fire by absorbing the incoming radiation. This behavior is heavily dependent on the radiation and the absorption characteristics of the LNG vapor, but this is a research field of its own.

2.3 Boiling regimes

Boiling is a process that includes a phase change from liquid to vapor, which occurs when a liquid is heated to or above its boiling point temperature at a given pressure. Depending on the temperature difference between the hot object transferring heat to the liquid and the liquid itself, the boiling regime changes.

2.3.1 Introduction

The boiling regimes are usually divided into natural convection boiling, nucleate boiling, transition boiling and film boiling. Fig. 2.3 shows a typical boiling curve for water at atmospheric pressure, including the various boiling regimes. Boiling curves for other liquids, both pure substances and mixtures, will be qualitatively similar.

An LNG pool boiling on a water surface is a temperature controlled system because the heat flux to the LNG is varied throughout the boiling process. This is due to the temperature difference between the water and the LNG changing, because the concentrations continuously changes, thereby changing the boiling point as well. When time passes, the boiling curve is also altered due to the change in liquid composition. This implies that the heat flux to the liquid pool is always decided by the temperature difference and the heat transfer coefficient at a given time and position. Such behavior complicates computations as it is necessary to recalculate heat transfer coefficients for the given boiling regime for all time steps and positions.

Determining the heat transfer coefficient in the various boiling regimes is a nontrivial task because the liquid composition strongly affects both the boiling regime and the heat transfer coefficient within that regime. Studies have shown that the heat flux in the film boiling regime increases in mixtures compared to pure liquids [7, 8]. The reason for this is explained in Ch. 4. In the nucleate boiling

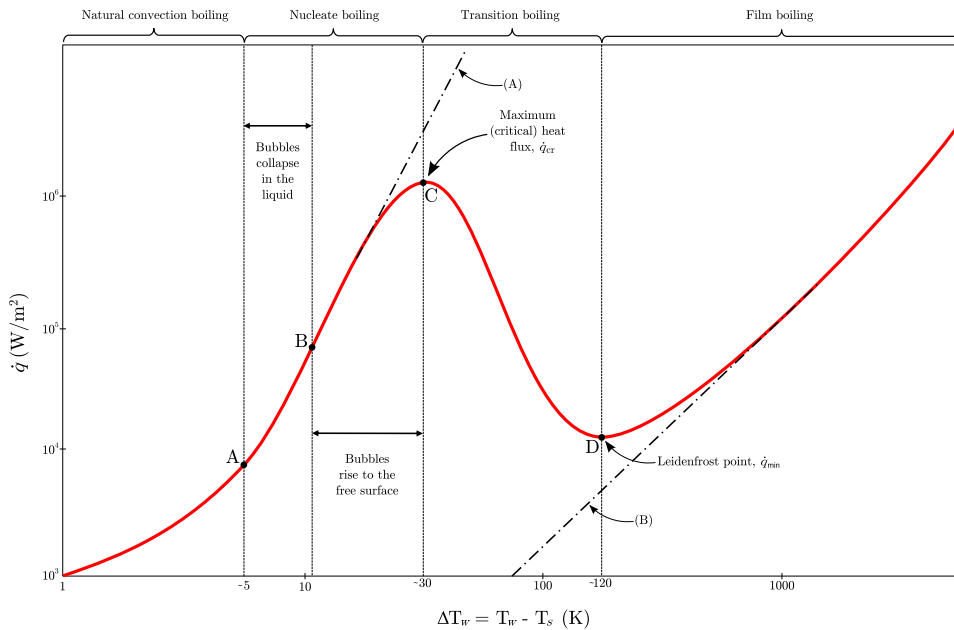


Figure 2.3: Boiling curve for water at atmospheric pressure. (A) is the principal extrapolation of the nucleate boiling heat flux. (B) is the principal extrapolation of the film boiling heat flux.

regime, on the other hand, the heat transfer coefficient for boiling of mixtures is found to be less than for pure substances (e.g. [9], which refers to lots of other papers).

2.3.2 Natural convection boiling

Bubbles will not emerge in a boiling process until the liquid is heated to a few degrees above the saturation temperature. The boiling regime until this point is called natural convection boiling because superheating of the liquid near the hot surface causes internal natural convection currents. Hot liquid rise towards the free surface while cold liquid drops to fill the space left by the hot one. A boiling process of natural convection boiling is shown in Fig. 2.4. The superheated liquid is in a metastable condition and it will therefore evaporate when it rises to the free surface. Natural convection boiling occurs until point A in Fig. 2.3.

2.3.3 Nucleate boiling

When the temperature difference between the heat source and the liquid is large enough (point A in Fig. 2.3), bubbles start forming at nucleation sites. Nucleation sites are impurities in the hot surface, for example small gaps where vapor is contained, or areas with different wetting properties that maintains established vapor pockets. From point A to B in Fig. 2.3 bubbles are formed but dissipated

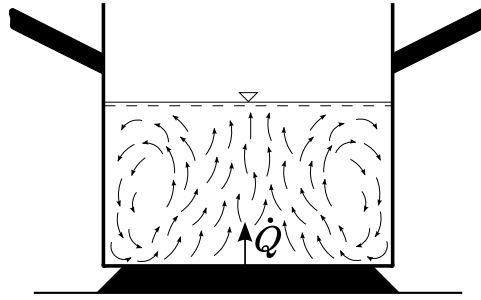


Figure 2.4: Natural convection boiling. Heat is transferred to the liquid at low ΔT_w and low heat flux.

in the liquid before they reach the free surface. Fresh, cold liquid fills up the space vacated by the vapor bubbles, thus increasing the heat transfer coefficient compared to natural convection boiling.

For a bubble to exist, the vapor in it needs to be slightly superheated and the vapor pressure has to be above a certain limit, lest the bubble collapses under the pressure from the liquid. These physical limits implies that there is a small thermal boundary layer near the heater surface in nucleate boiling (see App. A.1.1).

If the temperature difference is increased further, to a point between B and C in Fig. 2.3, bubbles are formed at such rate that they form continuous vapor strips towards the free surface where the vapor is released. In this region heat transfer is enhanced in the same way as between point A and B, but when the boiling process draws near to point C the bubble production is so large that fresh liquid has trouble reaching the heater surface. This makes the heat flux reach a maxima in point C, named maximum or critical heat flux.

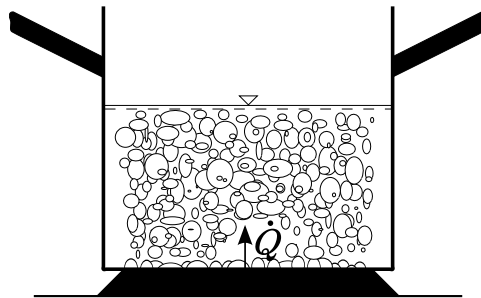


Figure 2.5: Nucleate boiling. Heat is transferred to the liquid at low ΔT_w and high heat flux.

Nucleate boiling is a desirable boiling regime in industrial applications because of the high heat flux at relatively low ΔT_w and it is therefore also the most studied one.

2.3.4 Transition boiling

When ΔT_w is increased beyond point C in Fig. 2.3, the vapor production becomes so high that areas on the heater surface become continuously covered by a vapor film. These vapor films act as thermal resistances, effectively decreasing the heat flux. As ΔT_w is increased further, an increasing part of the boiling area is covered by a vapor film, and at point D the whole area of the heater surface is covered by a continuous vapor film, which is the film boiling regime. It is therefore common to regard transition boiling as a mix between nucleate boiling and film boiling, as visualized in Fig. 2.6. When disregarding the lowest temperature differences, the heat flux is at its lowest at point D, named the minimum or Leidenfrost point.

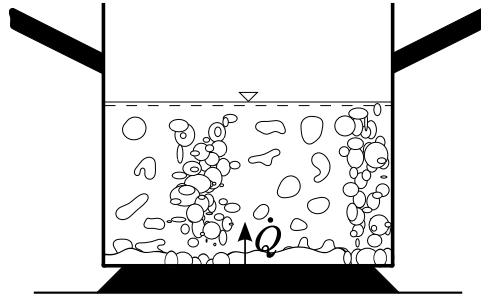


Figure 2.6: Transition boiling. Heat flux decreases with increasing ΔT_w because of the growing vapor film.

2.3.5 Film boiling

When the heater surface is fully covered by a vapor film at point D in Fig. 2.3, the boiling process is said to be in the film boiling regime (see Fig. 2.7). Beyond point D the boiling process is always in this regime.

Most attempts to establish correlations for the heat transfer in the film boiling regime are based on the use of Taylor instabilities. These instabilities occur because the liquid resting on top of the vapor film is heavier than the vapor itself [10, 11]. A perturbation of the vapor-liquid interface will therefore increase in amplitude until some vapor is released as bubbles, while liquid replaces the removed vapor and the interface is restabilized. Vapor is generated from the liquid at the vapor-liquid interface or from droplets entrained in the vapor film, adding to the vapor film thickness. However, the vapor film thickness and Taylor instabilities are connected so that the film thickness will never grow above a critical one [12].

Pool boiling of pure liquid methane on water boils in the stable film boiling regime while pure ethane and ethane rich mixtures boil in the transitional boiling regime [8]. It is common to assume that typical LNG mixtures on water boil in the film boiling regime due to the large initial temperature difference ($\sim 170 - 190$ K). This assumption is not strictly verified, however, and it is questioned on the basis of experimental data by Bøe [8].

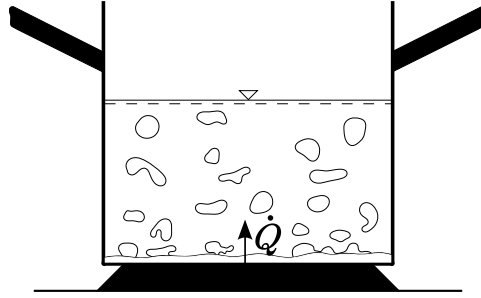


Figure 2.7: Film boiling. Heat is transferred to the liquid at high ΔT_w , but the heat flux is low due to the heat resistance in the vapor film.

2.4 Mass transfer

In the same manner as heat is transferred along temperature gradients, mass is transported along concentration gradients. If one region of a stationary fluid has high concentrations of a certain species relative to another, mass will be transported from that high concentration region to the low concentration zone. This is called mass diffusion, which can be regarded as nature being conservative, trying to level differences in the same manner as for example temperature and pressure.

The governing law for mass diffusion, Fick's law, is given as [4]

$$\dot{m}_{\text{diff}} = -D_{\text{AB}}A \frac{\partial X}{\partial n} = -D_{\text{AB}}A \frac{\Delta X}{L}. \quad (2.7)$$

The analogy to Fourier's law of heat conduction, Eq. (2.1) is clear; both are gradient models representing transportation from regions with high temperature or concentration to regions with low temperatures or concentrations.

Heat convection involves transfer of heat when a bulk fluid motion is present. If an LNG pool has a strong bulk motion, the internal mass convection can be described in a similar manner by [4]

$$\dot{m}_{\text{conv}} = h_{\text{mass}}A(X_I - X_b). \quad (2.8)$$

Eq. (2.8) is analogous to Newton's law of cooling, Eq. (2.3), as they both involve a transfer coefficient, an area and a driving force represented as a concentration difference or a temperature difference.

2.5 Liquid-vapor equilibrium

In Sec. 4.3 equilibrium data are needed to conduct calculations of pool boiling correlations for mixtures. The problem requires the fractions of both the liquid and the vapor phases as a function of the temperature to be solved. For a vapor mixture the basic relations

$$\sum_{i=1}^{n_s} Y_i = 1, \quad (2.9)$$

$$p_i = Y_i p \quad (2.10)$$

and

$$p = \sum_{i=1}^{n_s} p_i \quad (2.11)$$

are valid. Another useful relation is Raoult's law, relating the mole fractions in the liquid and the vapor phase with the total and the vapor pressure as [6]

$$Y_i p = X_i p_{vp_i}. \quad (2.12)$$

Eq. (2.12) assumes that the medium considered is an ideal solution, meaning that the components in the liquid mixture are similar (e.g. a mixture of n-butane and isobutane). This implies that Raoult's law most often is a rough approximation.

For a binary mixture, combining Eqs. (2.9) – (2.12) readily reduces the problem to

$$X_1 = \frac{p - p_{vp2}}{p_{vp1} - p_{vp2}}, \quad (2.13)$$

where subscripts 1 and 2 refers to the most and the least volatile components in the mixture, respectively. Eqs. (2.12) and (2.13) form the foundation for establishing phase equilibrium diagrams for binary mixtures (Fig. 2.8). Thus, to connect the mole fractions in the liquid and the vapor phases to the temperature, only the vapor pressures and the total pressure must be known.

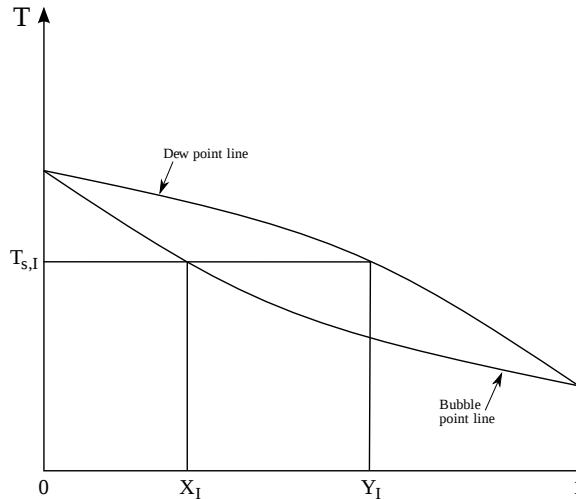


Figure 2.8: Phase equilibrium diagram for a binary mixture at its boiling point and constant pressure.

Clapeyron's equation [13],

$$\left(\frac{dp}{dT} \right)_s = \frac{h_{fg}}{T(v_v - v_l)}, \quad (2.14)$$

describes the thermodynamics in a phase change from liquid to vapor. Eq. (2.14) emerges readily from a basic Tds relation in combination with a Maxwell relation [13]. It assumes an isothermal phase change, which restrains the pressure to remain constant during the evaporation. By further assuming $v_v \gg v_l$ and employing the ideal gas relation $v = R_u T/p$, Eq. (2.14) reduces to

$$\left(\frac{dp}{dT}\right)_s = \frac{h_{fg}}{R_u T^2/p} \quad (2.15)$$

which by applying the chain rule can be rearranged to

$$\left(\frac{d \ln(p)}{dT}\right)_s = \frac{h_{fg}}{R_u T^2}. \quad (2.16)$$

Integration of Eq. (2.16) with the assumption that h_{fg} is independent of the temperature, Clapeyron's equation is reduced to the general form [6]

$$\ln p_{vp} = C_{vp,1} - \frac{C_{vp,2}}{T}. \quad (2.17)$$

[6] also gives a more applicable form of Eq. (2.17),

$$\ln p_{vpi} - \ln p_{ci} = \frac{T_{boil}}{T_{ci}} \frac{\ln p_{ci} - \ln p_{atm}}{1 - \frac{T_{boil}}{T_{ci}}} \left(1 - \frac{T_{ci}}{T}\right), \quad (2.18)$$

which written in a more compact form becomes

$$\ln p_{vpi} = \ln p_{ci} + \left[\frac{T_{boil}(T - T_{ci})}{T(T_{ci} - T_{boil})}\right] [\ln p_{ci} - \ln p_{atm}]. \quad (2.19)$$

Equation (2.19) gives satisfactory results in the region between the boiling point and the triple (critical) point, but long extrapolations above the critical point or below the boiling point can lead to large errors[6]. Values for T_c , p_c and T_{boil} for methane, ethane, propane and buthane are given in App. B.

Using Eqs. (2.12), (2.13) and (2.19) thereby enables the calculation of phase equilibrium data for binary mixtures (Fig. 2.8) which are needed for the pool boiling correlations for mixtures in Ch. 4.

2.6 Ice and hydrate formation

In small scale laboratory experiments of pool boiling of LNG on water, ice is often reported as the water cools below the freezing point due to the strictly confined spaces used. As Valencia-Chavez and Reid [14] also notes, this is not likely to happen for LNG spills on open sea due to natural convection effects in the water. In large scale experiments including LNG spilled on water, it is difficult to observe any ice without measurement equipment because of water droplets entrained in the LNG vapor (mist) decreasing the visibility.

An interesting point by Drake, Jeje and Reid [15] is that ice formation might be hydrates. Investigating small scale laboratory experiments, they found a weight

gain in the water straight after all the LNG had evaporated with a subsequent net weight loss in the water when the temperature had restabilized. This might indicate, they pointed out, that some hydrocarbons were still in the water, perhaps as hydrates, but when the temperature increased they dissolved and disappeared as vapor.

2.7 Definitions of non-dimensional quantities

The use of non-dimensional quantities is attractive because it is easy to scale a problem using the same correlation for the non-dimensional quantity. For convective heat transfer in flow over a flat plate, for example, the length of the plate heavily affects the resulting overall heat transfer coefficient, making direct calculations troublesome. If one instead uses the Nusselt number (Sec. 2.7.4) the same calculations can be used for any length of the flat plate.

2.7.1 The Reynolds number

The Reynolds number describes the ratio between inertia forces and viscous forces. It is defined as [4]

$$\text{Re} = \frac{\rho u L}{\mu}, \quad (2.20)$$

where ρ , u and μ are the fluid's mass density, velocity and viscosity, respectively, and L is a characteristic length of the geometry. Thus, if a flow has large velocity, density and/or length scale (i.e. large momentum) compared to viscosity, the Reynolds number will be large and the flow turbulent. On the other hand, if the viscous forces are large compared to the inertia forces the flow becomes laminar. The transition between laminar and turbulent flow is gradual and dependent on the geometry of the problem.

2.7.2 The Prandtl number

The Prandtl number describes the ratio between molecular diffusivity of momentum and molecular diffusivity of heat. It is defined as [4]

$$\text{Pr} = \frac{\nu}{\alpha} = \frac{\mu c_p}{K}, \quad (2.21)$$

where ν , α , μ , c_p and K are the fluid's kinematic viscosity, thermal diffusivity, dynamic viscosity, specific heat capacity and thermal conductivity, respectively. Most gases have a Prandtl number in the range 0.7 - 1.0. A fluid with high Prandtl number diffuses heat slowly (e.g. oils) while a fluid with low Prandtl number diffuses heat rapidly (e.g. liquid metals) [4].

2.7.3 The Grashof number

The Grashof number describes the natural convection effects in a fluid. It is defined as the ratio between buoyancy forces and viscous forces [4],

$$\text{Gr} = \frac{g\beta(T_s - T_b)L^3}{\nu^2}, \quad (2.22)$$

where g is the gravitational acceleration, β is a coefficient of volume expansion and T is the temperature. The flow regime in natural convection is governed by the Grashof number. A high Grashof number implies that the natural convection flow is turbulent, while a low Grashof number implies that the flow is laminar [4].

2.7.4 The Nusselt number

A convenient form of expressing heat transfer coefficients is the dimensionless Nusselt number. It is defined as the ratio between the convective and the conductive heat fluxes, Eqs. (2.4) and (2.2), respectively [4]

$$\text{Nu} = \frac{\dot{q}_{\text{conv}}}{\dot{q}_{\text{cond}}} = \frac{h\Delta T}{K\Delta T/L} = \frac{hL}{K}. \quad (2.23)$$

The most common problem in heat transfer physics is the calculation of the heat transfer coefficient, h , since the heat flux thereafter can be calculated by either Eq. (2.3) or (2.4). Thus, if a correlation for the Nusselt number is known (e.g. Eq. (A.19), (A.27) or (A.29)), the heat transfer coefficient can easily be calculated by rearranging Eq. (2.23).

2.7.5 The Rayleigh number

The product of the Grashof number and the Prandtl number arises in the definition of the Nusselt number when natural convection is included. Thus, the so-called Rayleigh number is defined as [4]

$$\text{Ra} = \text{GrPr} = \frac{g\beta(T_s - T_b)L^3}{\nu^2} \text{Pr}. \quad (2.24)$$

One example of such use is Eq. (A.19), though this expression uses a generalized Grashof number (Gr^*) and Prandtl number (Pr^*).

2.7.6 Relative volatility

When dealing with fluid mixtures, the relative volatility between two components i and j is often involved. It is defined as [16]

$$\alpha_{\text{rel}} = \frac{(Y_i/X_i)}{(Y_j/X_j)}, \quad (2.25)$$

where X and Y refers to the mole fractions in the liquid and the vapor phases, respectively.

α_{rel} describes the interaction between the various components in a mixture. For example, in the initial stage of the boiling process of a liquid mixture consisting of 95% methane and 5% ethane, $Y_{\text{CH}_4} \approx 1$, $X_{\text{CH}_4} \approx 0.95$, $Y_{\text{C}_2\text{H}_6} \approx 0$ and $X_{\text{C}_2\text{H}_6} \approx 0.05$, resulting in a high relative volatility of methane. This happens because the LNG vapor consists of nearly 100% methane early in the boiling process (Valencia-Chavez and Reid [14] found that $Y_{\text{CH}_4} > 99\%$ until about $X_{\text{CH}_4} \leq 20\%$). A high relative volatility thus implies that the vapor mixture contains a lot of the most volatile component.

2.8 General transport equations

Transport equations are partial differential equations (PDEs) describing transportation of one or more physical quantities (e.g. mass, momentum, energy) in time and space. In this and the two subsequent sections, Einstein's summation rule is applied, meaning that equal subscripts of i , j or l implies summation over that subscript. x_i , x_j and x_l refers to directions. A general form for transport equations is [17]

$$\frac{\partial}{\partial t}(\rho\phi) + \frac{\partial}{\partial x_j}(\rho\phi u_j) = \frac{\partial}{\partial x_j}(-j_{\phi j}) + S_\phi, \quad (2.26)$$

where $-j_{\phi j}$ is often modeled by the gradient model

$$-j_{\phi j} = \Gamma_\phi \frac{\partial \phi}{\partial x_j}. \quad (2.27)$$

The first term on the left hand side in Eq. (2.26) is the transient (time-dependent) term, which incorporates transportation of the quantity ϕ with time (zero for steady state). The second term represents convective transportation of ϕ (i.e. transportation with the flow). On the right hand side, the first term, often modeled as in Eq. (2.27), describes diffusive transportation of ϕ (e.g. viscous diffusion, turbulent diffusion, mass diffusion). S_ϕ is the source or sink term, describing loss or gain of ϕ , for example LNG added to the liquid pool from an LNG tank (source) or dissipation of turbulence energy (sink).

In turbulence modeling, Reynolds decomposition, $u_i = \bar{u}_i + u'_i$, modeling the velocity u_i as a mean velocity \bar{u}_i plus a fluctuation u'_i or Favre decomposition, $u_i = \tilde{u}_i + u''_i$, which includes density changes, are often used. This sometimes creates additional terms like production and redistribution in Eq. (2.26) (e.g. production of turbulence energy and redistribution of turbulence energy between the different stress components).

2.9 Models in KFX

Kameleon FireEx (KFX) is a CFD-tool for turbulent flow and combustion, fire simulation and gas dispersion, developed by ComputIT AS. This section briefly describes the most important models and numerics used in the software. There are lots of models and submodels in KFX, as is the case for any comprehensive CFD

software. It is important that the incorporated models are as close to reality as possible, weighted against the computing time. The information in this section is collected from the KFX Theory Manual, [18], and [17].

2.9.1 Turbulence model

KFX uses an extended version of the k - ε model for the turbulence. The k - ε model, Eqs. (2.30) and (2.31), describe transportation of turbulence energy and dissipation rate through transport equations (Sec. 2.8).

The momentum equations are given as

$$\frac{\partial(\bar{\rho}\tilde{u}_i)}{\partial t} + \frac{\partial(\bar{\rho}\tilde{u}_i\tilde{u}_j)}{\partial x_j} = -\frac{\partial\tilde{p}}{\partial x_i} + \frac{\partial}{\partial x_j} \left(\tilde{\tau}_{ij} - \bar{\rho}\widetilde{u_i''u_j''} \right) + \bar{\rho}\tilde{f}_i, \quad (2.28)$$

where \tilde{f}_i are body forces (volume forces) and the mass weighted Reynolds stresses, $-\bar{\rho}\widetilde{u_i''u_j''}$, are modeled as

$$-\bar{\rho}\widetilde{u_i''u_j''} = \mu_{\text{turb}} \left(\frac{\partial\tilde{u}_i}{\partial x_j} + \frac{\partial\tilde{u}_j}{\partial x_i} \right) - \frac{2}{3} \left(\bar{\rho}k + \frac{\partial\tilde{u}_l}{\partial x_l} \right) \delta_{ij}. \quad (2.29)$$

In KFX, there are two additional effects included compared to the standard k - ε model; low Reynolds number effects and buoyancy effects. The equation for the turbulence energy, k , (the k -equation) is written as

$$\frac{\partial(\bar{\rho}k)}{\partial t} + \frac{\partial(\bar{\rho}\tilde{u}_i k)}{\partial x_i} = \frac{\partial}{\partial x_i} \left(\left(\mu + \frac{\mu_{\text{turb}}}{\sigma_k} \right) \frac{\partial k}{\partial x_i} \right) + \bar{\rho}P_k - \bar{\rho}\varepsilon + B. \quad (2.30)$$

The dissipation rate of turbulence energy, ε , is determined from

$$\begin{aligned} \frac{\partial(\bar{\rho}\varepsilon)}{\partial t} + \frac{\partial(\bar{\rho}\tilde{u}_i\varepsilon)}{\partial x_i} &= \frac{\partial}{\partial x_i} \left(\left(\mu + \frac{\mu_{\text{turb}}}{\sigma_\varepsilon} \right) \frac{\partial\varepsilon}{\partial x_i} \right) + C_{\varepsilon 1}f_{\varepsilon 1}\rho P_k \frac{\varepsilon}{k} \\ &\quad - C_{\varepsilon 2}f_{\varepsilon 2}\rho \frac{\varepsilon^2}{k} + C_{\varepsilon 1}C_{\varepsilon 3} \frac{\varepsilon}{k} B. \end{aligned} \quad (2.31)$$

Equations (2.30) and (2.31) is written using Einstein's summation rule, where x_i and x_j refer to directions. P_k is the production of mean turbulence energy, k , from the mean flow. It is expressed as

$$\bar{\rho}P_k = \mu_{\text{turb}} \left(\frac{\partial\tilde{u}_i}{\partial x_j} + \frac{\partial\tilde{u}_j}{\partial x_i} \right) \frac{\partial\tilde{u}_j}{\partial x_i} - \frac{2}{3} \left(\bar{\rho}k + \mu_{\text{turb}} \frac{\partial\tilde{u}_l}{\partial x_l} \right) \frac{\partial\tilde{u}_i}{\partial x_i}. \quad (2.32)$$

The buoyancy term is given and modeled as

$$B = \bar{\rho}\widetilde{u_i''\rho''}g_i = -\Gamma_{\rho,\text{turb}} - \frac{\mu_{\text{turb}}}{\sigma_\rho} \frac{\partial\bar{\rho}}{\partial x_i} g_i. \quad (2.33)$$

μ_{turb} is the turbulent diffusion coefficient or eddy viscosity, given as

$$\mu_{\text{turb}} = C_D f_\mu \rho \frac{k^2}{\varepsilon}, \quad (2.34)$$

where

$$f_{\mu} = \exp\left(-\frac{2.5}{1 + \text{Re}_{\text{turb}}/50}\right) \quad (2.35)$$

and

$$\text{Re}_{\text{turb}} = \frac{\rho k^2}{\mu \varepsilon}. \quad (2.36)$$

In the ε -equation, Eq. (2.31), the low Reynolds number correction terms are given as

$$f_{\varepsilon 1} = 1.0 \quad (2.37)$$

and

$$f_{\varepsilon 2} = 1.0 - 0.3 \exp(-\text{Re}_{\text{turb}}^2). \quad (2.38)$$

The constants in the k - ε model are given in Table 2.1. $C_{\varepsilon 3}$ is flagging the buoyancy situation by being 0 for the stable case and 1 for the unstable case.

Table 2.1: Constants in the k - ε model in KFX.

C_D	σ_k	σ_{ε}	$C_{\varepsilon 1}$	$C_{\varepsilon 2}$	σ_{ρ}
0.09	1.0	1.3	1.44	1.92	0.7

There are differences between the k - ε model in KFX and the “standard” k - ε model. In order to calculate heat fluxes from fluids to solid materials, KFX uses wall laws. Laws of the wall are supposed to take the effect of low velocities (i.e. low Reynolds numbers) near walls, as are the implemented low Reynolds modifications to the k - ε model in KFX. These two modifications are therefore usually not combined. Also, the buoyancy term is not included in the “standard” k - ε model.

2.9.2 Combustion model

The combustion model implemented in KFX uses the Eddy Dissipation Concept (EDC). EDC couples the mean flow and the chemical reactions in the flow’s fine structure through a cascade model and a reactor model using a turbulence model (e.g. the k - ε model) [17]. The first version of EDC was presented in 1976 and it has been continuously developed and improved since then [18]. KFX also incorporates a soot model beside EDC; the Eddy Dissipation Soot Model.

2.9.3 Pool spreading model

For calculations of pool spreading of a liquid pool on solid ground or water, KFX uses an extended version of the shallow water equations, which also handles multi-component liquids by using a conservation equation for each species. The shallow water equations are a version of Navier-Stokes that has been integrated in the vertical direction. The extended shallow water equations used in KFX are discussed in more detail in Ch. 6.

2.10 Numerics in KFX

In order to perform calculations of any sorts on a computer, the equations to be solved need to be discretized.

2.10.1 Finite Volume Method

To represent and evaluate the transport equations as a set of algebraic equations, KFX uses a method called the Finite Volume Method (FVM). In CFD, FVM is the most common technique because of its clear relationship between the physical conservation laws and the numerical implementation [19]. FVM can be summarized in three steps: (1) volume integration of the governing fluid flow equations; (2) discretization of the resulting integral equations into a system of algebraic equations; and (3) solving of the discretized equations by an iterative method.

The conservation of a general flow variable ϕ can be summarized as

$$\left[\begin{array}{l} \text{Rate of change} \\ \text{of } \phi \text{ in the} \\ \text{control volume} \\ \text{with respect to} \\ \text{time} \end{array} \right] = \left[\begin{array}{l} \text{Net rate of} \\ \text{increase of } \phi \text{ due} \\ \text{to convection} \\ \text{into the control} \\ \text{volume} \end{array} \right] + \left[\begin{array}{l} \text{Net rate of} \\ \text{increase of } \phi \text{ due} \\ \text{to diffusion into} \\ \text{the control} \\ \text{volume} \end{array} \right] + \left[\begin{array}{l} \text{Net rate of} \\ \text{creation of } \phi \\ \text{inside the} \\ \text{control volume} \end{array} \right].$$

This describes the same as the general transport equation in Sec. 2.8.

2.10.2 SIMPLEC

KFX uses a staggered grid to solve the flow conservation equations, meaning that the control volumes for p , u_x , u_y and u_z are shifted relative to each other. This is done to avoid interpolation of the pressure in the momentum equations, thereby eluding unphysical checkerboard effects [19].

When the discrete equations on the staggered grid are established, it is time to solve them. There are several possibilities, but KFX uses the SIMPLEC algorithm (Semi Implicit Method for Pressure Linked Equations Consistent). The solution chart is as follows, given a pressure field and a velocity field from the previous time step [19]:

1. Guess or use the previous initial velocity and pressure fields as preliminary values.
2. Solve the momentum equations.
3. Solve an equation for the pressure correction.
4. Correct the preliminary velocities and pressures using the pressure correction.
5. Check that convergence is fulfilled. If so, proceed to point 6, else, repeat from point 2 until it is.

6. Solve the equations for other scalar variables (energy equation, k - ε equations etc.).
7. Execute the necessary corrections between each time step (update density on the basis of temperature etc.).
8. Proceed to point 1 for a new time step.

The difference between the SIMPLEC algorithm and the “standard” SIMPLE algorithm is that SIMPLE neglects some terms in the pressure correction equation that SIMPLEC does not. SIMPLEC does also neglect some terms, however, but those are less significant than the ones neglected in SIMPLE. The choice of algorithm may effect both numerical stability and convergence rate, but if the solution procedure converges, SIMPLE and SIMPLEC will produce the same results.

2.10.3 The Courant number

A dimensionless number often used in numerical analysis of fluid flows is the Courant number, defined as [20]

$$C = \bar{u} \frac{\Delta t}{\Delta x}. \quad (2.39)$$

Too high Courant numbers might lead to too fast propagations of the flow information, hence producing wrong results. In KFX, both a maximum Courant number and a maximum time step are chosen to ensure that the information does not propagate too fast for the numerics.

3 Validation of pool boiling correlations

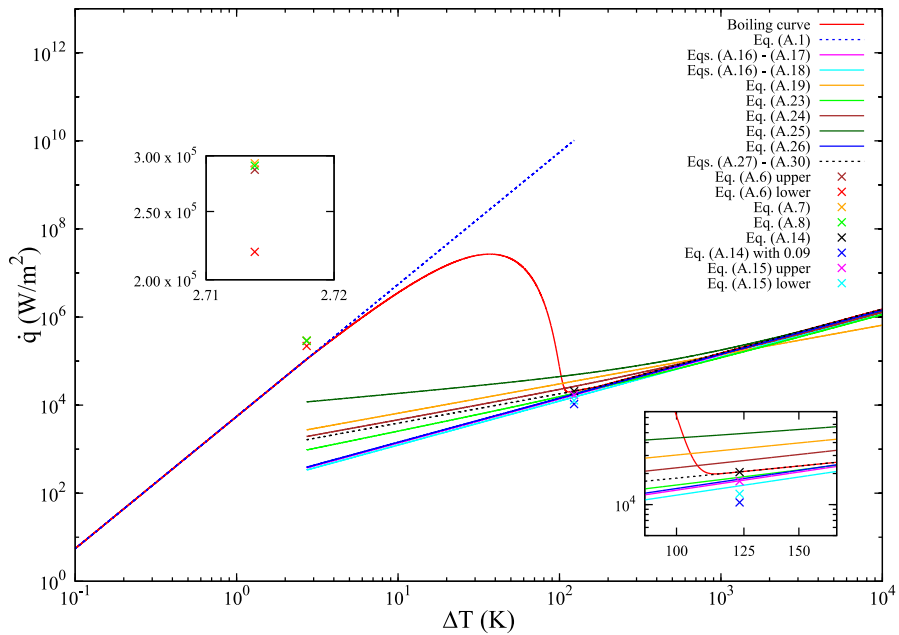
A previous study [2] concluded that it is not correct to use correlations for pool boiling of pure liquids (see App. A) to describe the boiling process of mixtures. These correlations can, however, be used as estimations for the heat transfer coefficient rather than guessing it. In comprehensive calculation programs (e.g. CFD programs) these heat transfer calculations might not be the most uncertain part and it is therefore useful to analyse the pool boiling correlations for pure liquids in more detail.

3.1 Heat transfer calculations

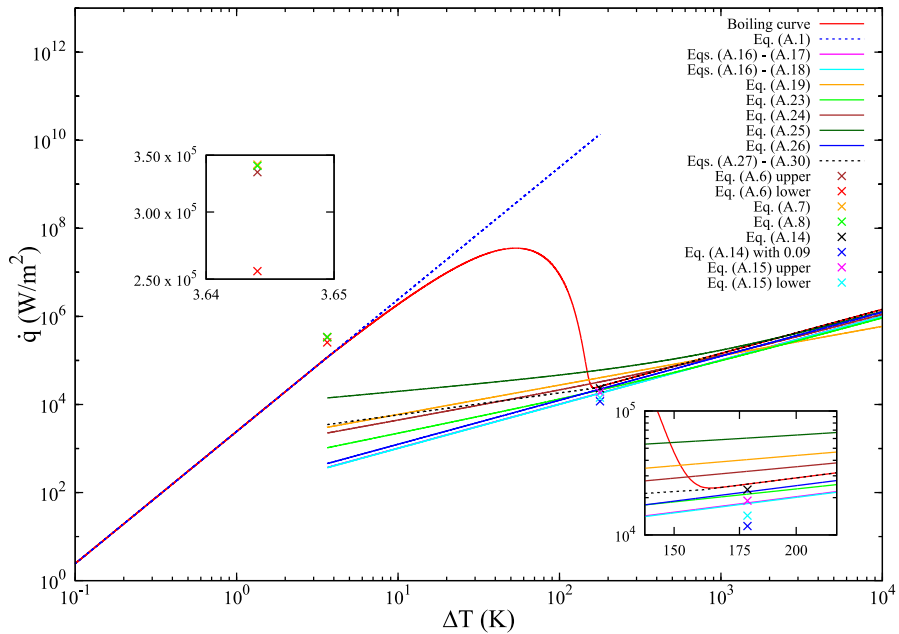
To perform calculations of the correlations given in App. A physical properties of the fluids are needed. In the current work, these properties are collected from the NIST database [21] except for the surface tension which is calculated by Eq. (B.1) [22] and the superheat limit temperature which is collected from [23]. Four fluids have been selected as a possible approximation for LNG (methane, ethane, propane and butane), whose physical properties are listed in App. B. These properties together with the pool boiling correlations in App. A are the basis of the calculations in this chapter.

3.1.1 Description of the calculations

Figure 3.1 shows the results of the calculations of all correlations in App. A for the selected fluids. The transition boiling heat flux is calculated by Eqs. (A.10) – (A.12). This method is an interpolation between the extrapolated curves for both the nucleate and the film boiling heat flux (see Fig. 2.3 on page 7), creating a smooth transition between the various boiling regimes and a qualitatively correct boiling curve. However, because of this interpolation of the extrapolated values, the maximum heat flux on the boiling curve exceeds the calculated values of \dot{q}_{cr} by approximately two orders of magnitude, obviously creating a source of error. The transition boiling regime is confined by the critical and the minimum heat flux, represented by the crosses in the figure.

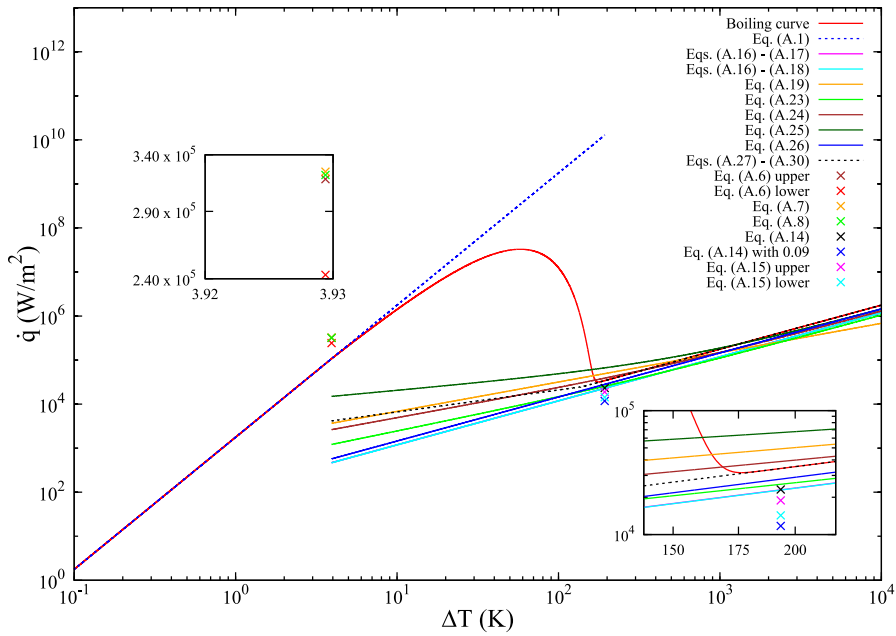


(a) Results of pool boiling calculations of methane at 111.0 K.

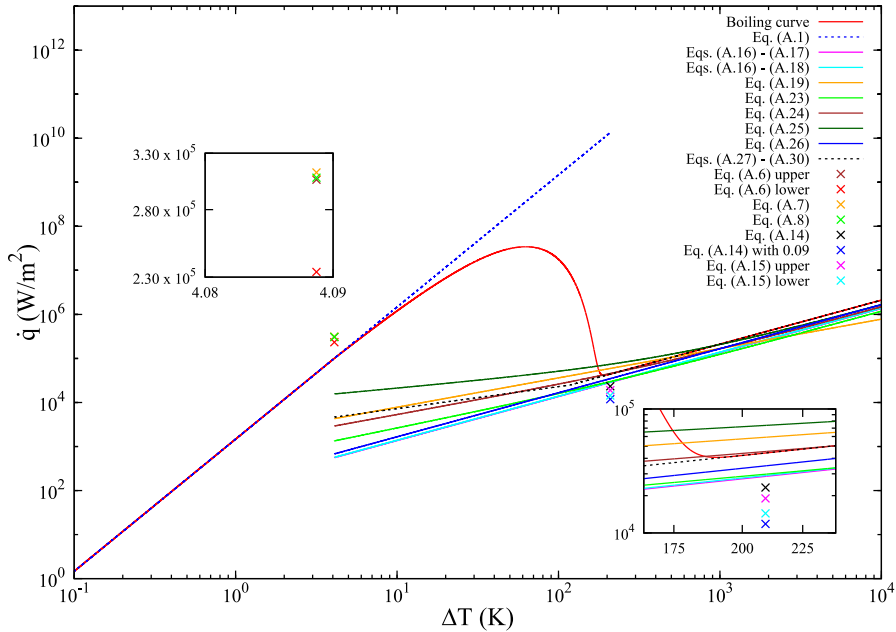


(b) Results of pool boiling calculations of ethane at 184.6 K.

Figure 3.1: Results of pool boiling calculations of methane, ethane, propane and butane at their boiling points. The physical properties used are given in App. B. The views show the critical point and the Leidenfrost point.



(c) Results of pool boiling calculations of propane at 231.1 K.



(d) Results of pool boiling calculations of butane at 273.0 K.

Figure 3.1: Results of pool boiling calculations of methane, ethane, propane and butane at their boiling points. The physical properties used are given in App. B. The views show the critical point and the Leidenfrost point.

Table 3.1: The largest \dot{q}_f divided by the smallest \dot{q}_f at both the Leidenfrost point and the largest calculated ΔT_w .

	Methane	Ethane	Propane	Butane
Leidenfrost point	3.210	3.376	2.909	2.579
$\Delta T_w = 10000$ K	2.317	2.427	2.586	2.707

The following method is used to establish the boiling curve (red) in Fig. 3.1:

1. Calculate ΔT_{cr} from Eq. (A.9) using Eq. (A.8) for \dot{q}_{cr} .
2. Calculate ΔT_{min} from Eq. (A.18).
3. Calculate \dot{q}_n from Eq. (A.1) for all ΔT s until ΔT_{min} .
4. Calculate \dot{q}_f from Eqs. (A.27) – (A.30) from ΔT_{cr} to an ending ΔT_w (10000 K was used here). Any other film boiling correlation could have been used as well.
5. Calculate \dot{q}_t using Eqs. (A.10) – (A.12).

The boiling curve is then connected by the calculated values for \dot{q}_n until ΔT_{cr} , \dot{q}_t between ΔT_{cr} and ΔT_{min} and \dot{q}_f from ΔT_{min} to the last ΔT_w , creating a smooth transition between all the boiling regimes. For the transition boiling regime, Eq. (A.12) is chosen instead of Eq. (A.13), simply because the latter imposes a discontinuity in the boiling curve.

The leftmost crosses in Fig. 3.1 represent the critical heat flux from Eqs. (A.6) – (A.8) at ΔT_w from Eq. (A.9). This point is where the boiling regime changes from nucleate boiling to transition boiling. The rightmost crosses, on the other hand, represent the change from transition boiling to film boiling. The minimum heat flux is calculated from either of Eqs. (A.14) – (A.16) at ΔT_{min} from Eq. (A.17) or (A.18).

Table 3.2: Calculated values of \dot{q}_{cr} (kW/m²).

	Methane	Ethane	Propane	Butane
Eq. (A.6) (upper)	286.67	334.20	317.53	305.46
Eq. (A.6) (lower)	219.11	255.44	242.70	233.48
Eq. (A.7)	292.74	341.23	324.27	312.01
Eq. (A.8)	290.39	340.04	321.23	307.29

It is clear from Fig. 3.1 that the various film boiling correlations match each other fairly well. The largest deviation between them are found near the Leidenfrost

point and at the highest temperature difference calculated, for all fluids, and is tabulated in Table 3.1. At the Leidenfrost point the factor separating the largest and the smallest calculations of \dot{q}_f are 3.210, 3.376, 2.909 and 2.579 for methane, ethane, propane and butane, respectively. Although there are some deviations between the correlations, they are the same order of magnitude throughout the entire calculated film boiling regime.

Klimenko [24] established a set of correlations, Eqs. (A.27) – (A.30), by assembling other film boiling correlations into a more general description and to fit more experimental data. Klimenko found that these correlations matched experimental data of nine different fluids within $\pm 25\%$. That Eqs. (A.27) – (A.30) work as an average of the other film boiling correlations is evident in the views of the Leidenfrost point in Fig. 3.1. This is applicable at least until about $\Delta T_w = 300$ K which is above the temperature differences obtainable in film boiling of methane, ethane, propane or butane on water. In other words, Klimenko’s correlations seem to serve their purpose by estimating the film boiling heat flux as an average of all the others in App. A. In the rest of this thesis it is therefore assumed that Klimenko’s correlations are the most general for calculating the film boiling heat flux.

3.1.2 The critical heat flux

Calculated values of \dot{q}_{cr} are given in Table 3.2. The lower limit of Eq. (A.6) gives values which deviate from the other correlations. Because of this, one can argue that the three other correlations are better estimations for the critical heat flux. Additionally, Eq. (A.8) gives values in between Eqs. (A.6) (upper) and (A.7), so using this correlation for the critical heat flux might be a good approximation.

The only use for \dot{q}_{cr} in the current work is to calculate ΔT_{cr} from Eq. (A.9). This enables the calculation of the transition boiling regime since it is then known at what ΔT_w the change from nucleate boiling to transition boiling occurs. Ideally, the critical heat fluxes should match the nucleate boiling part of the boiling curve, but different theoretical backgrounds and tuning to experimental data create some deviations.

Table 3.3: Calculated values of ΔT_{cr} (K).

	Methane	Ethane	Propane	Butane
Eqs. (A.6)(upper) and (A.9)	2.70	3.62	3.91	4.08
Eqs. (A.6)(lower) and (A.9)	2.47	3.31	3.58	3.73
Eqs. (A.7) and (A.9)	2.72	3.65	3.94	4.11
Eqs. (A.8) and (A.9)	2.71	3.64	3.92	4.09

3.1.3 The critical temperature difference

The critical temperature difference is calculated from Eq. (A.9) by using any of Eqs. (A.6) – (A.8) for \dot{q}_{cr} (results are given in Table 3.3). When using the lower limit of Eq. (A.6) for \dot{q}_{cr} , ΔT_{cr} deviates from the other calculated values in the same manner as it deviated for \dot{q}_{cr} . This will be the result since either of Eqs. (A.6) – (A.8) work as a constant input in Eq. (A.9). The impact on the calculated boiling curve (the red curve in Fig. 3.1) when choosing either of these correlations for ΔT_{cr} is negligible. It therefore seems plausible that using Eq. (A.8) together with Eq. (A.9) gives reliable results for ΔT_{cr} .

3.1.4 The minimum heat flux

Calculated values of \dot{q}_{min} are given in Table 3.4. The four correlations used are Eq. (A.14), Eq. (A.14) with 0.09 as constant instead of 0.177 [25] and both the upper and the lower limit of Eq. (A.15). In fact, all these equations simplifies to the same correlation since $\rho_l \gg \rho_v$, but with various constants because of different theoretical backgrounds and tuning to experimental data. The values of \dot{q}_{min} deviate more than the values for \dot{q}_{cr} and it is uncertain which correlation fits the actual boiling process best. \dot{q}_{min} is not used for any calculations, however, and is therefore merely a visual parameter in this work.

The view of the Leidenfrost point in Fig. 3.1 show that the four correlations for \dot{q}_{min} probably underestimates the value to some extent as they all lie below most of the curves for film boiling. It is worth to note that Zuber’s theoretical expression for the first stage of a Taylor instability, Eq. (A.14), seems to match the film boiling correlations better than the other ones. The values for \dot{q}_{min} should in principle match the chosen correlation for film boiling, but usually does not in the same manner as \dot{q}_{cr} does not.

3.1.5 The minimum temperature difference

There are few correlations established for the minimum temperature difference in the literature. The results given in Fig. 3.1 are based on the use of Eq. (A.18) for ΔT_{min} , but Eq. (A.17) could have been used as well. The values calculated from these two equations deviate much, as shown in Table 3.5. ΔT_{min} is a critical

Table 3.4: Calculated values of \dot{q}_{min} (kW/m²).

	Methane	Ethane	Propane	Butane
Eq. (A.14)	20.640	23.178	23.110	23.264
Eq. (A.14) with 0.09	10.495	11.786	11.751	11.829
Eq. (A.15) (upper)	16.826	18.893	18.841	18.970
Eq. (A.15) (lower)	12.735	14.301	14.261	14.359

Table 3.5: Calculated values of ΔT_{\min} (K).

	Methane	Ethane	Propane	Butane
Eq. (A.17)	71.65	167.52	189.29	229.23
Eq. (A.18)	123.21	178.28	193.26	209.15

parameter because it is used to estimate where the change from transition boiling to film boiling occurs and to calculate the transition boiling regime by inserting it into Eq. (A.11) to calculate ΔT^* . The resulting boiling curve may alter a lot by the choice of Eq. (A.17) or (A.18). This is evident in Fig. 3.2.

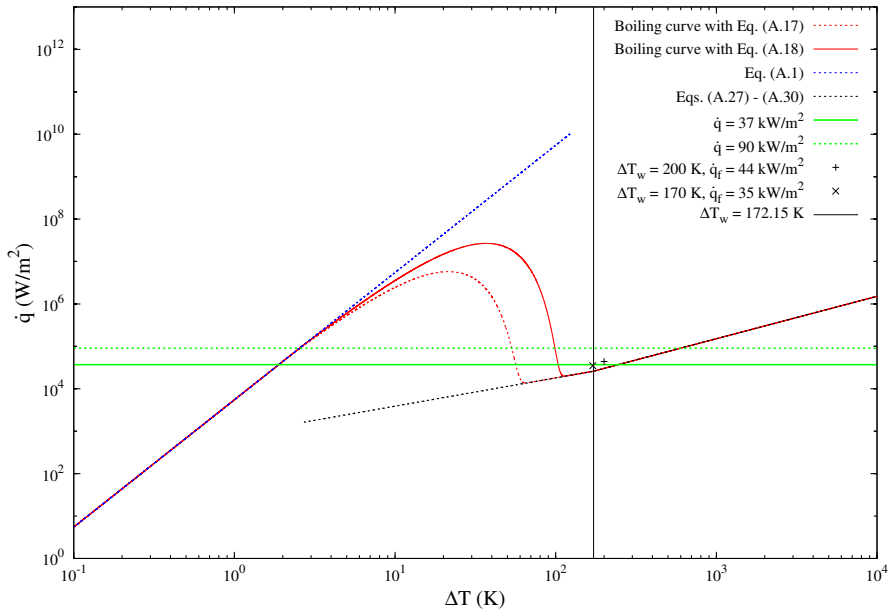
When choosing Eq. (A.18) for ΔT_{\min} for methane, the maximum heat flux on the boiling curve increases and the transition boiling regime stretches over a wider ranges of temperature differences than if Eq. (A.17) was chosen (see Fig. 3.2a). This is also the case for ethane, but to a lesser degree. For butane, on the other hand, using Eq. (A.17) gives higher maximum heat flux and wider transition boiling regime than using Eq. (A.18) for ΔT_{\min} . Choosing either Eq. (A.17) or (A.18) for ΔT_{\min} for propane has negligible impact on the result.

These results are directly linked to the values in Table 3.5. The largest calculated ΔT_{\min} results in the largest maximum heat flux and the widest transition boiling regime due to the method of interpolation in Eqs. (A.10) – (A.12). This is in turn linked to the physical properties of the chosen fluid (ΔT_{\min} in Eq. (A.18) is also dependent on the properties of liquid water which are nearly constant). Further investigations of which ΔT_{\min} estimate the real one best are conducted in Sec. 3.2.

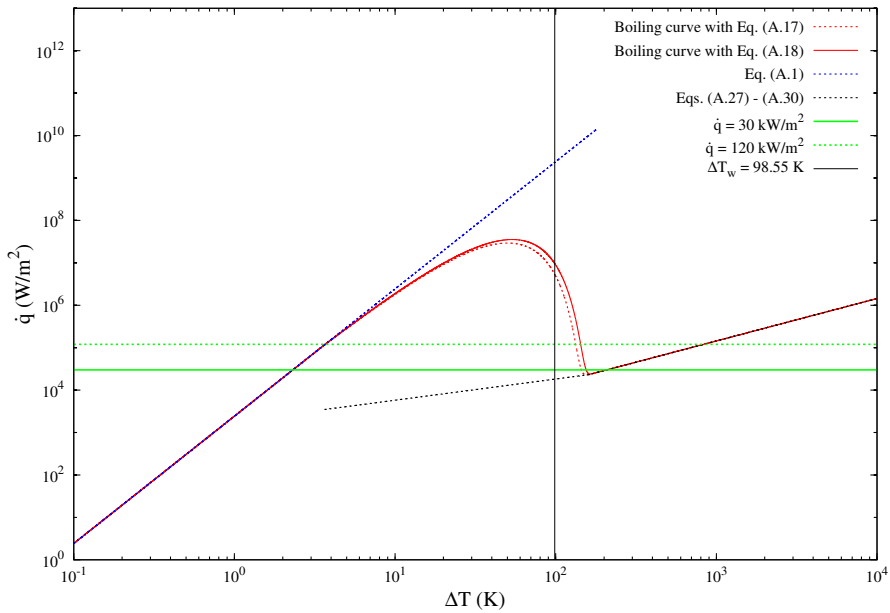
3.2 Comparison with experimental data for pure liquids

In the previous section, the results from calculations of the pool boiling correlations for pure liquids in App. A were presented. It was argued that Klimenko's correlations for film boiling are the best way to describe the film boiling heat flux in the possible intervals of ΔT_w for the selected hydrocarbon fluids. Additionally it was found that Eq. (A.18) is an adequate approximation for \dot{q}_{cr} and that combining this equation with Eq. (A.9) gives reliable results for ΔT_{cr} . To check the validity of these assumptions, it is important to compare them with experimental data. Table 3.6 lists some numbers and conclusions from various experimental data found in the literature which the calculations can be compared to.

An interesting investigation is to check which boiling regime the calculations give for the selected fluids. Fig. 3.2 shows the calculated boiling curves including lines representing the temperature difference between the boiling liquid and the water. Methane is found to boil in the film boiling regime while ethane boils in the

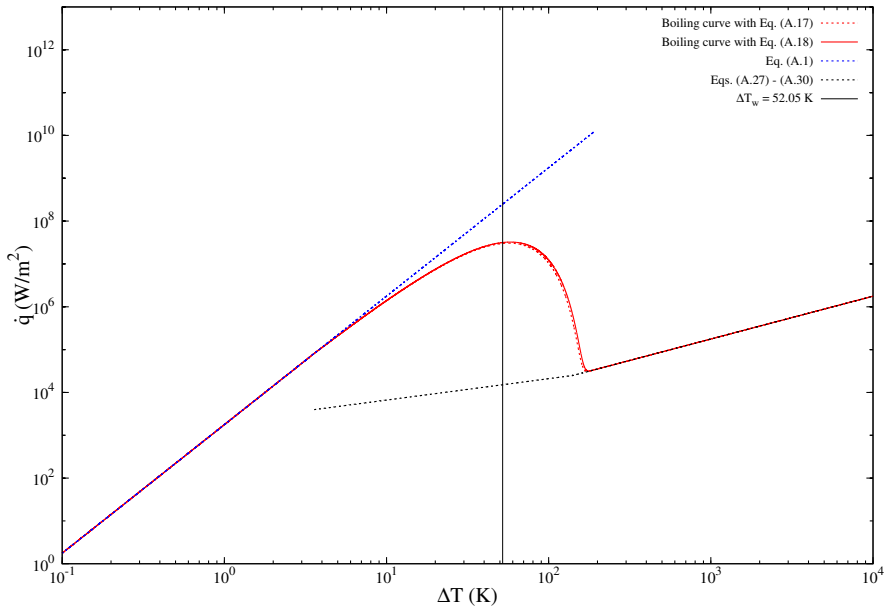


(a) Boiling regime and some experimental data for pure methane.

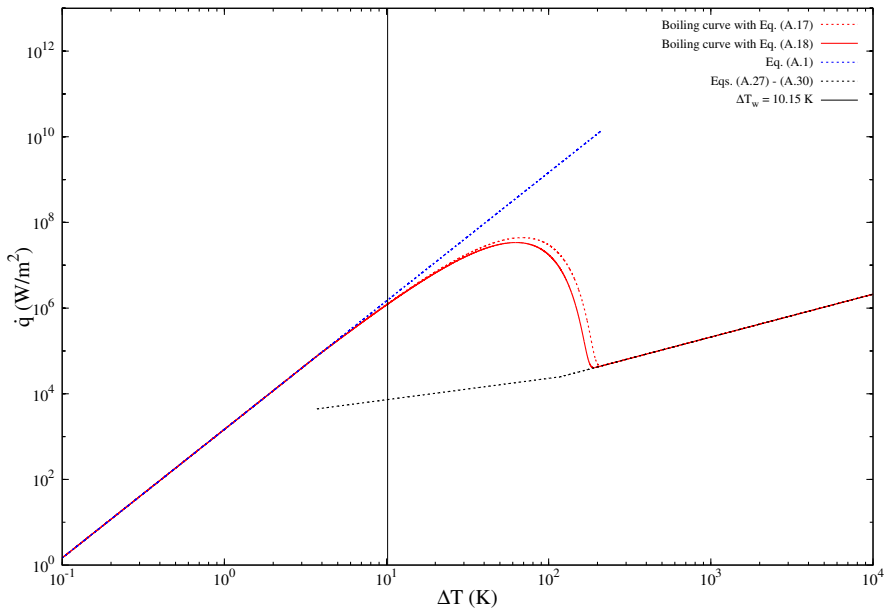


(b) Boiling regime and some experimental data for pure ethane.

Figure 3.2: Calculated boiling curves using both Eqs. (A.17) and (A.18) and consequently boiling regime. Some experimental data for pure methane and ethane are included in their plots.



(c) Boiling regime for propane.



(d) Boiling regime for butane.

Figure 3.2: Calculated boiling curves using both Eqs. (A.17) and (A.18) and consequently boiling regime. Some experimental data for pure methane and ethane are included in their plots.

transition boiling regime. These results are in accordance with the two first experimental observations in Table 3.6. Both propane and butane are calculated to be in the transition boiling regime, but butane is a lot closer to the nucleate boiling regime. There are no data supporting either of these results.

Table 3.6: Pool boiling data for pure liquids.

Data	Description	Reference
Pure methane boiling on water is in the stable film boiling regime.	Conclusion from experiments on a confined water surface of 200 cm ² .	Runar Bøe [8].
Pure ethane and ethane rich mixtures are in the transition boiling regime.	Conclusion from experiments on a confined water surface of 200 cm ² .	Runar Bøe [8].
$\dot{q}_f = 44$ kW/m ² for pure methane boiling at $\Delta T_w = 200$ K.	Reference to other work ^a . Calculated value is $\dot{q}_f = 30.24$ kW/m ² .	Runar Bøe [8].
Methane boiling on a solid surface at $\Delta T_w = 170^\circ\text{C}$ gives a heat flux of about 35 kW/m ² .	Reference to other experimental data ^b . Calculated value is $\dot{q}_f = 25.74$ kW/m ² .	Drake, Jeje and Reid [26].
The heat flux for pool boiling of methane on water varies from 37–90 kW/m ² .	Conclusion from experiments on a confined water surface of 77.3 cm ² .	Drake, Jeje and Reid [26].
The heat flux for pool boiling of pure ethane on water varies from 30–120 kW/m ² .	Conclusion from experiments on a confined water surface of 77.3 cm ² .	Drake, Jeje and Reid [26].

^a C.T. Sciance, C.P. Colver and C.M. Sliepcevich, Film boiling measurements and correlation for liquefied hydrocarbon gases, *Chemical Engineering Progress Symposium Series*, 1967, **63**(77), 115-119.

^b Drake, Jeje and Reid [26] refers to two papers for these numbers: C.T. Sciance, C.P. Colver and C.M. Sliepcevich, Pool boiling of methane between atmospheric pressure and the critical pressure, *Advances in Cryogenic Engineering* **12**, 390-408 (1966). C.M. Sliepcevich, H.T. Hashemi and C.P. Colver, Heat transfer problems in LNG technology, *Chem. Engng Prog. Symp. Ser.* **64**(87), 120-126 (1968).

If the water temperature in the calculations was to be increased, it would only result in shifting the temperature difference by as much as the water temperature was increased. This will never affect the boiling regime, except for ethane if the water temperature is increased to about 90°C which is not the case for a spill on

open sea.

Some available heat flux data for pool boiling of pure methane and ethane are reproduced in Table 3.6. The data for methane are plotted in Fig. 3.2a. Both the experimental data point where $\Delta T_w = 170$ K and $\dot{q}_f = 35$ kW/m² and the one where $\Delta T_w = 200$ K and $\dot{q}_f = 44$ kW/m² support the experimental conclusion that methane boils in the film boiling regime according, to the calculated boiling curve. The calculated values at $\Delta T_w = 170$ K and $\Delta T_w = 200$ K are 25.74 kW/m² and 30.24 kW/m², respectively, resulting in deviations of 26.5% and 31.3%. Bøe [8] refers to the work of Zuber for a theoretical value of 244 kW/m² for \dot{q}_{cr} . This value is in the interval of Eq. (A.6), but it deviates somewhat from the value used in these calculations which was 290.39 kW/m², calculated by Eq. (A.8).

Drake, Jeje and Reid's observation [26] that the heat flux for pool boiling of pure methane on water varied from 37 kW/m² initially to 90 kW/m² at the end of an experimental run (Table 3.6) may be concomitant with a shift from film boiling to transition boiling (see Fig. 3.2a). The calculated temperature difference matching a film boiling heat flux of 90 kW/m² is 595 K, which is impossible to obtain for pool boiling of methane on water (water evaporates at about 373 K), also suggesting a change to transition boiling.

In Drake, Jeje and Reid's experiments, 450–500 g of water was placed at the bottom of a cylinder of inner diameter of 9.92 cm. Such a small amount of water indicate a decrease in the water temperature (little space for natural convection) and that the temperature difference concurrently decreases. Therefore, a shift to transition boiling and an increase in the heat flux is imminent, a fact that was also discussed by the authors. This physical observation is in agreement with the calculated boiling curve methane. The calculated temperature difference for transition boiling heat flux of 90 kW/m² is approximately 99 K. There are obvious limitations in the calculations as this implies a water temperature of about -63°C when using Eq. (A.18) for ΔT_{\min} . Nevertheless, temperature differences well below 0°C were in fact reported as well as ice formation due to the small amount of water in a confined space.

Using Eq. (A.17) for ΔT_{\min} , on the other hand, suggests that the water temperature falls to almost -109°C for a transition boiling heat flux of 90 kW/m² which is an even more unlikely result. This indicates that applying Eq. (A.18) for ΔT_{\min} gives better results than using Eq. (A.17), at least for pure methane. This assumption is a possible source of significant errors, hence warranting further investigations. Experimental data are scarce, however, and Eq. A.18 seems to be the best option for calculating ΔT_{\min} for pool boiling of pure methane.

Available data for pool boiling of ethane is also limited. Drake, Jeje and Reid [26] report approximate heat transfer rates starting at 60 kW/m², quickly building up to 120 kW/m² before decreasing to about 30 kW/m² over time for initial water temperatures between 8°C and 49°C . The authors observed that an ice shield quickly formed on the water surface and discussed that this may have caused a shift into the nucleate boiling regime. Then, as the ice gets steadily colder, the heat flux decreases with the decreasing temperature difference. These experimental results and observations are not in agreement with the results in

Fig. 3.2b. This might be due to the ice shield that was formed; the correlations in App. A are based on experimental data where no ice was observed. The calculated temperature difference for the nucleate boiling regime for $\dot{q}_n = 120 \text{ kW/m}^2$ is 3.67 K, so even if there is a shift to nucleate boiling, the calculations seems to be in quite some error (the ice would have to have a temperature of about -85°C). These disagreements applies to calculations using both Eqs. (A.17) and (A.18).

As might have been expected, the least investigated boiling regime, transition boiling, seems to be the most uncertain part of these calculations. The method of calculating the transition boiling heat flux, Eqs. (A.10) – (A.12), is probably resulting in abnormally high heat fluxes near the maximum of the boiling curve, but there are no experimental data supporting or contradicting this. It is also clear that the nucleate boiling heat flux plays an important role in these calculations. If the slope of the nucleate part of the boiling curve was less steep, it would result in a decrease of the maximum calculated transition boiling heat flux. The nucleate boiling calculations (Eq. A.1) therefore play an important part of the overall calculations and represent a great deal of uncertainty.

The choice of a correlation for calculating ΔT_{\min} is also a source of uncertainty for the calculated transition boiling regime, both in heat flux values and the temperature differences it spans across. Experimental data used to establish Eqs. (A.12) and (A.13) include pool boiling of nitrogen on teflon, CCl_4 on copper, *n*-pentane on copper, Freon 113 on steel and Freon 113 on copper, so the interpolation curve for hydrocarbons on water may differ greatly from the one appearing using Eq. (A.12) or (A.13).

There are clear uncertainties in these calculations because only a limited amount of experimental data exist, theories are established on different bases and constants are tuned to various experimental data including lots of different fluids. Nevertheless, the correlations currently used seem to be the best there are today.

3.3 Comparison with experimental data for mixtures

To verify if the calculated boiling curve for pure methane can be used to approximate LNG, it has been plotted against some of the reported heat fluxes for methane-ethane and methane-propane mixtures from the experimental work of Bøe [8] in Fig. 3.3. The mole fractions of methane in the methane-ethane mixtures are between 0.75 and 0.85 and the ones in the methane-propane mixtures are between 0.50 and 0.70. The water temperature in the experimental runs varied between 25°C and 40°C . Collected experimental data are from very early in the runs, so no ice had been formed at that point.

As discussed in the previous section, the maximum point on the boiling curve is a lot higher than the theoretical maximum heat flux. It is clear from Fig. 3.3 that most of the experimental data are almost at or above the theoretical critical heat flux for pure methane. Other experiments on boiling of multicomponent liquids have reported this behavior as well, for both hydrocarbon mixtures and mixtures of other liquids; the heat flux in the boiling of mixtures is higher than that of the pure components (e.g. [14, 15, 7]).

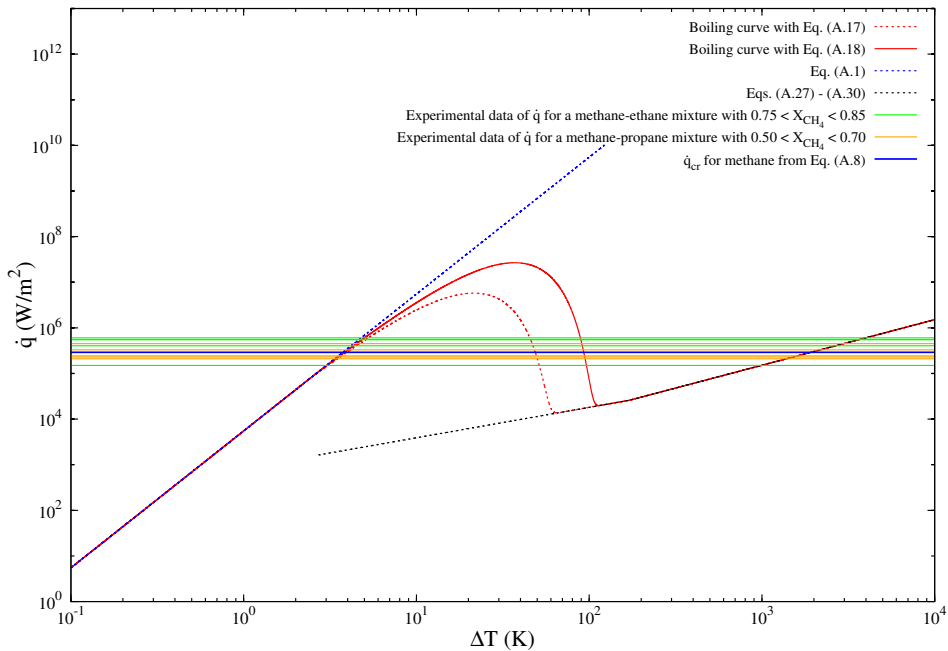


Figure 3.3: Calculated boiling curve for pure methane and experimental data [8] for methane-ethane and methane-propane mixtures.

The reason for this behavior is discussed in more detail in Ch. 4. This implies that it is not strictly correct to approximate an LNG mixture as methane by using the pool boiling correlations established for pure liquids (App. A). Conrado and Vesovic [3] concluded that doing this will result in wrong dynamics of the vapor formation. In order to account for this, the modeling of pool boiling of LNG on water must be done in a different way. Two such models are discussed in Ch. 5 and simulation results using these models are presented in Ch. 7.

3.4 Summary and conclusions

This chapter has investigated the pool boiling correlations for pure liquids given in App. A in more detail. Boiling curves have been established for methane, ethane, propane and butane in their pure forms to check the calculated values against experimental data for pure methane, pure ethane, methane-ethane mixtures and methane-propane mixtures. Physical data used for the hydrocarbons are given in App. B. The investigations have led to the following main conclusions:

- The highest calculated transition boiling heat fluxes on the boiling curve are abnormally high because of the method of interpolation. Both \dot{q}_n and \dot{q}_f are heavily influencing \dot{q}_t , but the correlations used for the film boiling heat flux,

Eqs. (A.27) – (A.30), are more validated than the one used for the nucleate boiling heat flux, Eq. (A.1), making further investigation of \dot{q}_n important.

- Klimenko’s film boiling correlations, Eqs. (A.27) – (A.30), work as an average of the others in App. A, and are therefore the preferred film boiling correlation for the rest of this thesis.
- The calculated values for ΔT_{cr} and \dot{q}_{cr} varies little with the choice of correlation and has therefore no visible effect on the boiling curve. There are no experimental data to validate these results against.
- Using either Eq. (A.17) or (A.18) for ΔT_{min} alters the calculated boiling curve by stretching or compressing the transition boiling regime over different rangers of ΔT s. Therefore, ΔT_{min} is a critical parameter in these calculations.
- Comparison of the calculated boiling curve for methane with experimental data shows good agreement. This is not the case for ethane, however, and there is little experimental data for validation.
- The pool boiling correlations for pure fluids cannot be used to approximate mixtures. Neither can an LNG mixture be approximated as pure methane.

4 Boiling of mixtures

Boiling of mixtures acts profoundly different from boiling of pure substances. The heat flux and the evaporation rate can be drastically different, a concentration and a temperature boundary layer is set up near the interface in the boiling liquid and mass transfer (diffusion) plays a role in the heat transfer mechanisms [27]. This chapter presents the properties in boiling of mixtures and ways to model this process when taking these properties into account.

4.1 Properties in boiling of mixtures

In the boiling process of a pure liquid, the mole and mass fractions of both the liquid and the vapor phase are always unity and there is virtually no change in the temperature through the boiling liquid. When considering a mixture, on the other hand, the concentrations of the different species will vary with time and position since the most volatile component evaporates faster, leaving the less volatile components behind, a process usually referred to as ageing. The ageing process is the source of the mixture effects of concentration and temperature boundary layers.

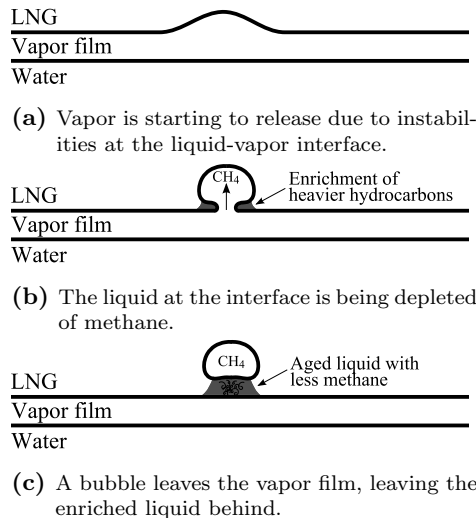


Figure 4.1: The process of ageing in the boiling of a mixture.

4.1.1 Concentration and temperature boundary layers

Consider an LNG mixture boiling in the film boiling regime upon water as shown in Fig. 4.1. When the most volatile component (i.e. the methane) evaporates at the liquid-vapor interface, the fractions of the heavier hydrocarbons in the liquid phase increase, thereby changing the concentrations of all liquid species in the vicinity. This establishes a concentration gradient often referred to as a concentration boundary layer. Although Fig. 4.1 implies that LNG boils in the film boiling regime, this is not necessarily the case; the ageing process that creates the concentration boundary layer applies to both nucleate boiling and transition boiling as well.

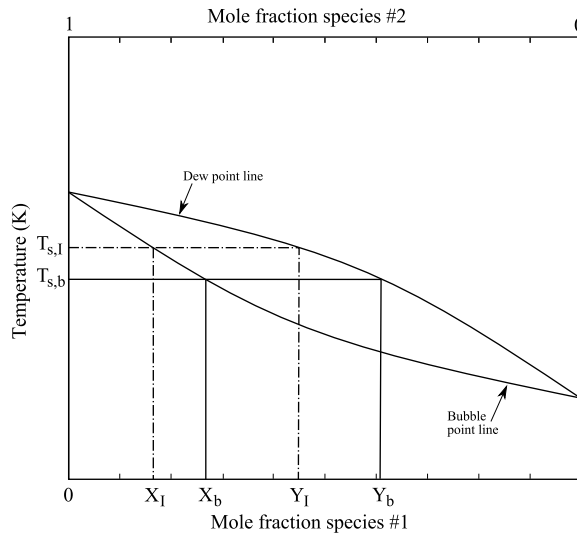


Figure 4.2: Phase equilibrium diagram for a binary mixture at constant pressure, showing the temperature response to a concentration change.

Concurrently with the change in concentrations, the boiling point of the mixture also changes. This can qualitatively be described by a liquid-vapor equilibrium approach, as shown in Fig. 4.2. Initially the temperature of the entire mixture will be at the bulk boiling point, $T_{s,b}$, but when the most volatile component evaporates, the molar concentrations near the hot surface (nucleate boiling) or vapor film (film boiling) changes from Y_b, X_b to Y_I, X_I , causing the liquid temperature to rise to $T_{s,I}$. This sets up a temperature gradient in the boiling liquid, usually called a temperature boundary layer. The temperature boundary layer is four to five times thicker than the concentration boundary layer for mixtures of high relative volatility [28].

4.1.2 Mass transfer

As described in Sec. 4.1.1, the concentrations in the liquid near the hot surface or at the liquid-vapor interface change as the most volatile component evaporates.

The established concentration differences allows for mass diffusion internally in the boiling liquid, where the most volatile component is transported from the bulk liquid to the interface and vice versa for the other components. Moving relatively hotter particles from the interface towards the bulk liquid might also contribute to the overall heat exchange, but diffusion of relatively colder particles the opposite way must also be considered.

4.1.3 *Conductive heat transfer*

Conductive heat transfer is described in Sec. 2.2.1. In the same way as the concentration boundary layer allows for mass diffusion internally in the boiling liquid, the temperature boundary layer allows for internal heat conduction. Due to the relatively higher temperature near the hot surface or liquid-vapor interface, heat will be conducted into the bulk liquid. This represents yet another path of heat transfer to the boiling liquid that can be a part of the explanation for the change in heat transfer in the boiling of mixtures.

As heat is conducted from the interface towards the bulk liquid, it will be superheated in the proximity. Superheating of the boiling liquid is part of the explanation for rapid phase transitions (Sec. 4.5) and the mixture effect of heat conduction might play a part in this phenomenon.

4.2 Nucleate boiling of mixtures

Experiments conducted on nucleate boiling of mixtures show that the heat transfer coefficient decreases compared to the one of pure substances. There are several theories as to why this is so [27, 29]: (1) the non-linear behavior in the physical properties of a mixture (e.g. viscosity) makes the heat transfer coefficient decrease; (2) a change in the mass transfer resistance for the most volatile component when diffusing into a growing bubble reduces the heat transfer coefficient; (3) preferential boiling of the most volatile component makes the liquid phase containing higher concentrations of the less volatile components clog the nucleation sites, thereby decreasing the vaporization rate; and (4) the increase in the boiling point in the microlayer near the hot surface reduces the temperature driving force. Several studies have been conducted to investigate these theories, only to find that all of them contribute to the decrease in the heat transfer coefficient to some extent.

An empirical model for the nucleate pool boiling heat flux of ternary mixtures was developed by Vinayak Rao and Balakrishnan [29]. It is developed on the basis of experimental data obtained for mixtures of acetone-isopropanol-water and acetone-methyl ethyl ketone-water, and takes the mixture effect of mass diffusion into account. Correlating these experimental data in terms of the Archimedes number, the Prandtl number, a surface-liquid interaction parameter, a modified Jakob number, a dimensionless surface roughness group, a properties-profile parameter

and an effective temperature driving force, they arrived at

$$\begin{aligned} \dot{q}_n &= 1.34 \cdot 10^{-5} (\text{Ar}_{\text{mix}})^{-0.95} (\text{Pr}_{\text{mix}})^{-0.9} (\gamma_{\text{mix}})^{1.3} (\text{Ja}_m)^{0.85} \\ &\times \left(\frac{R_a p}{\sigma_{\text{mix}}} \right)^{0.73} (\text{Bo}_{\text{mix}}^*)^{-1.36} (\Delta T_{\text{eff}})^2, \end{aligned} \quad (4.1)$$

where

$$\text{Ar} = \left(\frac{g}{\nu_l^2} \right) \left(\frac{\sigma}{\rho_l g} \right)^{1.5}, \quad (4.2)$$

$$\gamma = \sqrt{\frac{k_w \rho_w c_{pw}}{k_l \rho_l c_{pl}}}, \quad (4.3)$$

$$\text{Ja}_m = \frac{\rho_l c_{pl} \Delta T_{\text{eff}}}{\rho_v h_{\text{fg}}} \quad (4.4)$$

and

$$\text{Bo}^* = \frac{\rho_l R_a^2 g}{\sigma}. \quad (4.5)$$

The effective temperature difference for a ternary mixture is defined as

$$\Delta T_{\text{eff}} = \left[1 - \sum_{i=1}^2 \left((Y_i^* - X_i^*) \sqrt{\frac{(\bar{D})^{0.5}}{\alpha_{\text{mix}}}} \right)^{0.5} \right] \Delta T_w, \quad (4.6)$$

where \bar{D} is the determinant of the Fick matrix of diffusion coefficients, a parameter that greatly hampers calculations. If the system considered is a binary mixture,

$$\Delta T_{\text{eff}} = \left[1 - \left(|Y_i^* - X_i^*| \sqrt{\frac{D_{\text{AB}}}{\alpha_{\text{mix}}}} \right)^{0.5} \right] \Delta T_w \quad (4.7)$$

can be used to calculate ΔT_{eff} [29]. ΔT_{eff} describes the modified temperature driving force when mass diffusion is taken into account.

The center line average, R_a , is used to characterize the surface micro-roughness and will differ from material to material (teflon was used as the heater material in [29] with $R_a = 0.52 \mu\text{m}$). Y_i^* and X_i^* refers to the equilibrium vapor and liquid mole fractions, respectively. Eq. (4.1) was also found to match experimental data for other liquid mixtures good, as well.

R_a is an uncertain parameter as its value for pool boiling on water is unknown. Since $\dot{q}_n \sim R_a^{2.73}$, it might affect the calculated nucleate boiling heat flux a lot if it is chosen incorrectly. The rest of the model is simple, except for the diffusion coefficient, which might complicate calculations.

4.3 Film boiling of mixtures

In contrast to nucleate boiling of mixtures, the heat transfer coefficient in film boiling of mixtures is increased compared to the ones for the various pure components alone. Marschall and Moresco [30] concluded that the main reason for the increased heat transfer is because of the vapor film properties depend on the temperature at the liquid-vapor interface which in turn depends on the diffusion rate in the liquid phase. Such change in the vapor film properties will alter the heat transfer resistance in it, allowing more heat to pass through. This diffusion effect is heavily dependent on the relative volatility of the mixture because it determines the slope of the concentration gradient and therefore also the diffusion rate [28].

Several experimental studies have reached this conclusion [7, 8, 15]. In practice, this means that it is not plausible to use the mole or mass weighted averaged quantities of the heat transfer coefficients to describe film boiling of mixtures. The mixture effects are smaller in film boiling than in nucleate boiling for the same α_{rel} , however, a fact which is shown both experimentally and theoretically [27].

Another explanation for the increased heat transfer is that the heat conducted into the bulk liquid represents another route for heat removal, hence less heat is used to generate vapor at the liquid-vapor interface. This implies that the vapor film thickness in film boiling of mixtures is less than for film boiling of pure liquids, which in turn implies that the overall heat resistance in the vapor film is reduced. Therefore, the heat flux to a liquid mixture boiling in the film boiling regime is greater than its pure liquid counterparts [27].

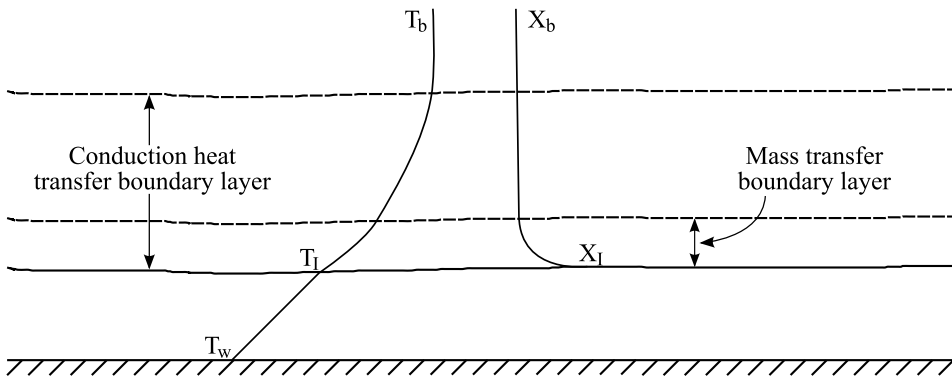


Figure 4.3: Temperature and concentration profiles in film boiling of mixtures. The temperature boundary layer is 4-5 times thicker than the concentration boundary layer [28].

Figure 4.3 can be used to follow such reasoning. When some of the most volatile component evaporates at the liquid-vapor interface, the boiling temperature of the liquid will increase, forcing the liquid interface temperature, T_I , to increase as well. This causes the temperature difference across the vapor film $\Delta T_w = T_w - T_I$ to decrease. Therefore, a liquid mixture boiling in the film boiling regime will receive more heat at a lower ΔT_w than its pure liquid counterpart, which

does not experience a reduction in ΔT_w . Since less heat is used for evaporation at the interface due to heat conduction into the liquid, the vapor film thickness decreases and the overall vapor film resistance is hence reduced, making the heat transfer increase subsequently. The heat conducted into the boiling liquid will also contribute to superheating of the bulk liquid, which is believed to be the source of rapid phase transitions (see Sec. 4.5).

Similarly to the heat conduction's contribution to the effective heat transfer, the mass transfer will also contribute by transporting hot liquid molecules of the less volatile components from the interface into the bulk liquid. Simultaneously, cold molecules of the most volatile component will diffuse back towards the liquid-vapor interface. This diffusive mixing of hot and cold molecules is also enhancing the overall heat exchange to the boiling liquid.

Yue and Weber [28] described film boiling of a binary mixture by a two-phase boundary layer approach including heat conduction and mass diffusion in the liquid phase. This was done using a similarity transform of the momentum and energy equations for both phases. They found that boiling theory for pure liquids described the boiling process of mixtures adequately for relative volatilities less than about four. For relative volatilities higher than four, on the other hand, those theories did not describe the physics well and the full two-layer boundary layer approach, or another approach which takes mixture effects into account, had to be applied. They also developed an expression for the Leidenfrost temperature difference for mixtures [31]. Because the liquid temperature at the liquid-vapor interface is higher for mixtures than for pure liquids, they correlated ΔT_{\min} as the sum of the vapor film temperature difference for pure liquids and the temperature difference in the liquid,

$$\Delta T_{\min, \text{mix}} = (T_w - T_I) + [T_I - T_s(X'_b)], \quad (4.8)$$

where the last term was modeled as

$$T_I - T_s(X'_b) = \frac{Y'^* - X'_b}{(Y'^* - X'_b)_{\max}} [T^* - T_s(X'_b)]. \quad (4.9)$$

To be able to perform calculations of Eq. (4.8), equilibrium data between the liquid and the vapor at the interface are required (see Sec. 2.5). The first term represents the temperature difference for pure liquids while the second represents the mixture part.

Yue and Weber [31] used an expression of their own to calculate $(T_w - T_I)$. This expression was developed for film boiling of pure liquids on a horizontal cylinder and therefore includes the cylinder diameter, rendering it useless for pool boiling ($\Delta T_{\min} \sim d^{1/3}$). However, their expression is very similar to Berenson's Eq. (A.17), so an assumption that either of Eqs. (A.17) and (A.18) can be used to estimate $(T_w - T_I)$ in Eq. (4.8) seems to be in order. Since they are developed to calculate $(T_w - T_s)$ in pool boiling of pure liquids, they might therefore estimate the difference $(T_w - T_I)$ adequately.

To model the film boiling heat flux, and taking both the mixture effects of heat conduction and mass diffusion into account, one could use the mindset in

Fig. 4.4 and model the total heat transfer as

$$\dot{q}_{f,\text{mix}} = \dot{q}_{\text{conv}} + \dot{q}_{\text{cond}} + \dot{q}_{\text{diff}}. \quad (4.10)$$

If \dot{q}_{conv} is modeled as the heat transfer for film boiling of a pure substance, $\dot{q}_{f,\text{mix}}$ can be calculated using Eq. (2.7) for \dot{q}_{cond} and Eq. (2.8) together with the definition of $c_{p,l}$ for \dot{q}_{diff} . To make calculations possible, the length of the temperature or the concentration boundary layer has to be known together with mass diffusion coefficients between the different hydrocarbons in the LNG.

Such approach would increase the heat transfer compared to film boiling of pure liquids, which is physically correct. It is not clear how large the contribution from \dot{q}_{cond} and \dot{q}_{diff} would be, however, and they would have to be analyzed in more detail if this model was to be applied.

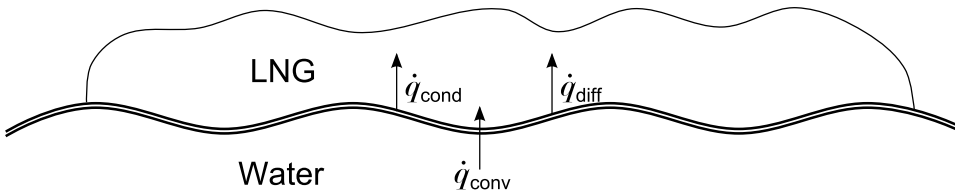


Figure 4.4: Qualitative overview of the heat transfer mechanisms in film boiling of mixtures.

4.4 Transition boiling of mixtures

For the calculation of the transition boiling heat flux in liquid mixtures, the same mindset as for pure liquids can be used. Eqs. (A.10) – (A.12) represent an interpolation between the extrapolated values for both the nucleate and the film boiling heat fluxes that establishes a smooth transition between the different boiling regimes. In Ch. 3 it was found that this method produces too high transition boiling heat fluxes for pool boiling of pure liquids. However, this might not be the case for pool boiling of mixtures since both the nucleate and the film boiling heat fluxes are quite different.

If the nucleate boiling part of the curve was less steep and the film boiling heat flux shifted upwards, which is the actual case for pool boiling of mixtures, this would cause the transition boiling part of the curve to be lowered. The principal result from such change is shown in Fig. 4.5. This would prevent the calculated transition boiling heat flux in mixtures from exceeding the real one by as much as was the case for pure liquids. To achieve this, the correlations in Sec. 4.2, Eqs. (4.8) – (4.9) and the method described earlier (Fig. 4.4) could be used together with a relation for \dot{q}_{cr} .

In Sec. 7.6 an analysis of the method of interpolation for the transition boiling regime is performed in an attempt to reduce the overestimations of the heat fluxes in the transition boiling regime.

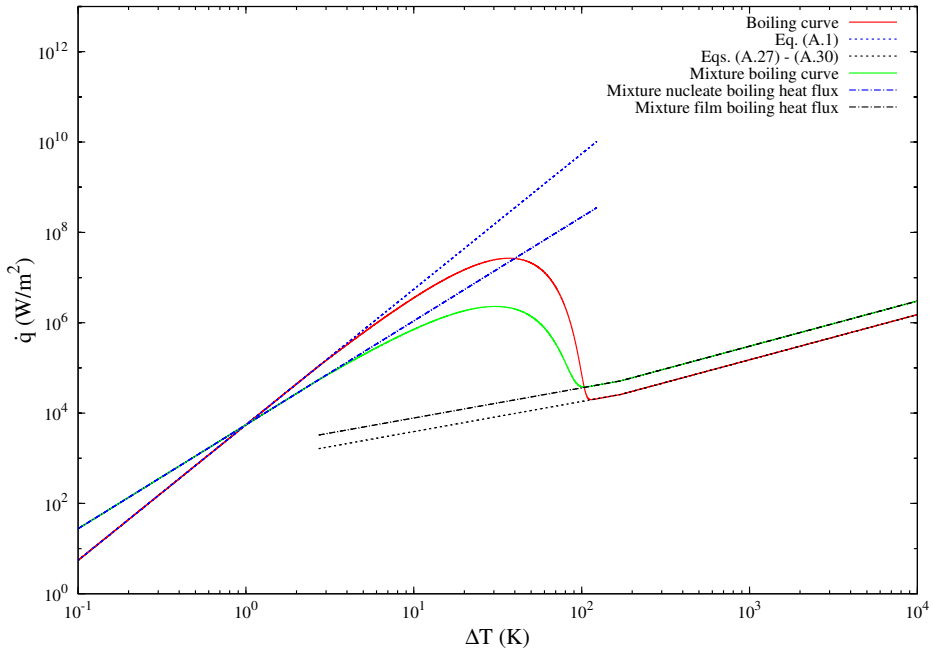


Figure 4.5: Principal change to the boiling curve when using pool boiling correlations for mixtures instead of for pure liquids.

4.5 Rapid phase transitions

A physical phenomenon called rapid phase transition (RPT) is sometimes observed in large scale experiments involving LNG spills on water (e.g. the Burro test series and the Coyote test series). RPTs are not combustion related and are therefore referred to as mechanical or physical explosions, because they release pressure built up in the LNG up to a maximum of 36 bars [1]. These explosions will also greatly affect other hazardous situations by changing the distance to the LFL and spread the cold LNG vapor in the ambience. An illustrative video of RPTs and fire in an LNG pool can be found on Youtube (www.youtube.com/watch?v=h-EY82cVKuA).

4.5.1 Description of RPTs

The main theory as to why RPTs occur uses the combined effect of two physical effects, namely changes in the boiling regime and the superheat limit (thermodynamic stability limit) [1]. When LNG is heated rapidly, any nucleation sites are rendered inactive since there is not enough time to generate the vapor bubbles. As the LNG is superheated to its superheat limit it resides in a state where it cannot exist in its liquid form, instantly flashing to vapor and increasing the local pressure. Fig. 4.6 shows this process for a standard LNG mixture. As the composition

changes, so do both the mixture superheat limit and the bulk boiling point, making the process of superheating LNG towards its superheat limit dynamic.

Film boiling is not likely to produce the heat fluxes needed to superheat the LNG to its superheat limit. When the composition of the LNG changes with time so does the boiling regime. A change from film boiling to transition boiling will promote liquid-liquid contact and a large increase in the heat flux from the water to the LNG, thereby enabling the heat transfer to increase to a level where the LNG can be heated to its superheat limit. The boiling regime of the LNG at a given point is also changing with time and composition, making the superheating towards the superheat limit is an even more dynamic process.

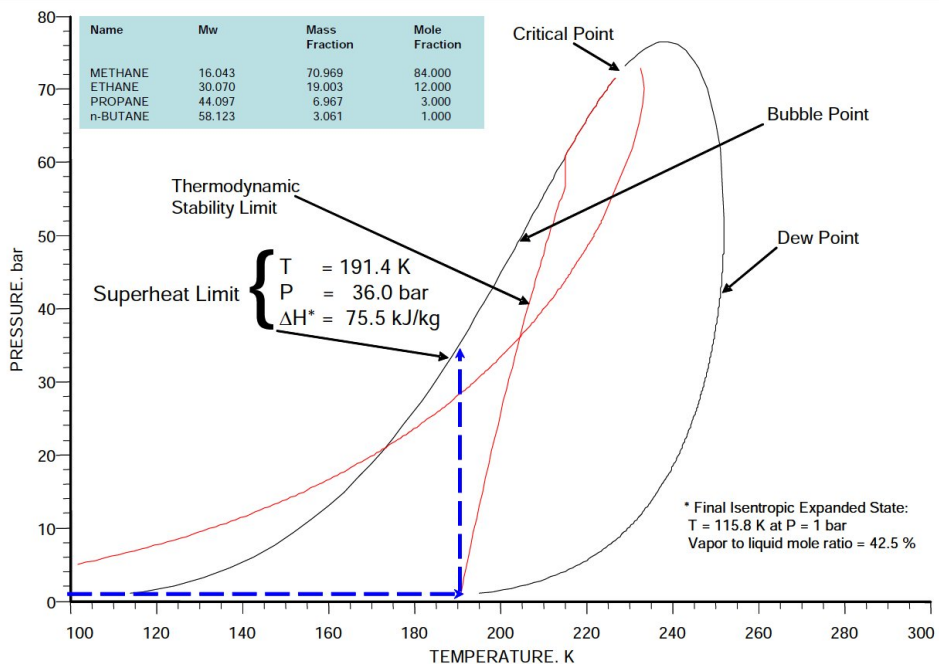


Figure 4.6: Superheat limit for a typical LNG mixture [1]. As the composition changes with time, so do the superheat limit and the boiling point.

In the Coyote test series, RPTs were observed in six of the runs. In five of these, RPTs occurred near the spill point while in two of them delayed RPTs at the outskirts of the LNG pool were detected. The early RPTs occurred immediately after LNG hit the water, sometimes continuing throughout the run, for the most part happening underwater. The delayed RPTs, on the other hand, generally occurred above the water surface in the later stages of the runs, at the outskirts of the LNG pool [32]. In the Burro test series several RPTs were also observed, both near the spill point and at the outskirts of the pool in the later stages [33].

Melhem *et al.* [1] found that for an LNG mixture initially consisting of 84% methane, 12% ethane, 3% propane and 1% nitrogen (mole fractions), the methane

concentration has to be less than 20% and the ethane concentration more than 50%, both by weight, for an RPT to occur. This theoretical finding was in accordance with observations in large scale experiments [1].

4.5.2 Early rapid phase transitions

Near the spill point there will be mixing between the water and the LNG, especially if the spill point is some distance above or below the water surface or if there are waves and currents in the water. This mixing will cause breakdown of any vapor film and promote liquid-liquid contact between the water and the LNG, even though the temperature difference implies film boiling, hence establishing good conditions for high heat transfer and evaporation rates. The high heat transfer might then lead to rapid superheating with a successive pressure buildup and release, observed as an RPT.

4.5.3 Delayed rapid phase transitions

In the regions where the LNG has aged for some time, generally at the outskirts of the pool, delayed RPTs are sometimes observed. As the LNG ages the mixture superheat limit changes accordingly. Porteous and Blander [23] found that the mixture superheat limit can be approximated by the mole fraction averaged quantity fairly well. This observation together with the criterion [34]

$$T_{SL} < T_w < 1.1T_{SL} \quad (4.11)$$

or

$$0.89T_c < T_w < 0.98T_c \quad (4.12)$$

for when an RPT can happen, can be used as a simple tool to investigate when and where RPTs are likely to occur in more comprehensive calculations of pool spreading and evaporation of LNG on water. This criterion is in accordance with the findings of Melhem *et al.* as described earlier; when the LNG ages and the composition changes to a certain level, RPTs can occur, a physical consideration also described by Eq. (4.11).

The superheating of the LNG will also be enhanced by the temperature and the concentration boundary layer established in it as heat is transported inwards and distributed more evenly (see Sec. 4.1.1). In Sec. 7.7 an in-depth analysis of RPTs using the theory described in this section is executed.

5 Pool boiling heat transfer models

Two models, LNGSIM1 and LNGSIM2, have been implemented in KFX to calculate the heat transfer to LNG pools on water and compare the results with experimental data. LNGSIM1 is based on the pool boiling heat transfer correlations for pure liquids given in App. A while LNGSIM2 is based on LNGSIM1 and a simple model for the concentration boundary layer (Sec. 4.1).

5.1 LNGSIM1

In Ch. 3 it was found that Klimenko's correlations, Eqs. (A.27) – (A.30), estimate the heat transfer in film boiling of pure liquids satisfactory. These correlations together with Eq. (A.1) for \dot{q}_n , Eqs. (A.10) – (A.12) for \dot{q}_t , Eq. (A.9) for ΔT_{cr} and Eq. (A.18) for ΔT_{min} are used to calculate the heat transfer coefficient from the water to the LNG pool in LNGSIM1. A flow chart of LNGSIM1 is shown in Fig. 5.1.

The physical properties used in the calculations are the mixture properties of the LNG, which are estimated by the correlations given in App. C. The only calculations differing from these are the ones of K_{vf} where the Prandtl number is assumed to be 0.8 for simplicity and the vapor densities ρ_v and ρ_{vf} which are calculated by a real gas relation with a manually calculated compressibility factor.

An important effect when using the mixture properties instead of approximating the liquid as a pure substance, is that the concentrations will change with time, making the calculated physical properties change with time as well. This further implies that the calculated boiling regime and thus the heat transfer to the liquid pool also change with time. Such time dependent heat transfer is physically correct, but as discussed in Ch. 3, the method of calculating the transition boiling heat flux may cause an abnormally high heat transfer in that regime. One possible side effect from this is that the calculated pool area might become limited if large portions of evaporate so rapidly that the pool cannot spread any further.

5.2 LNGSIM2

As described in Ch. 4, the heat transfer in film boiling of mixtures is greater than its pure liquid counterpart due to a decrease in the vapor film resistance because of internal heat conduction and mass diffusion. The heat transfer coefficient in nucleate boiling of mixtures is in a similar manner less than for pure liquids. It is therefore reasonable to believe that LNGSIM1 produces too low heat fluxes for

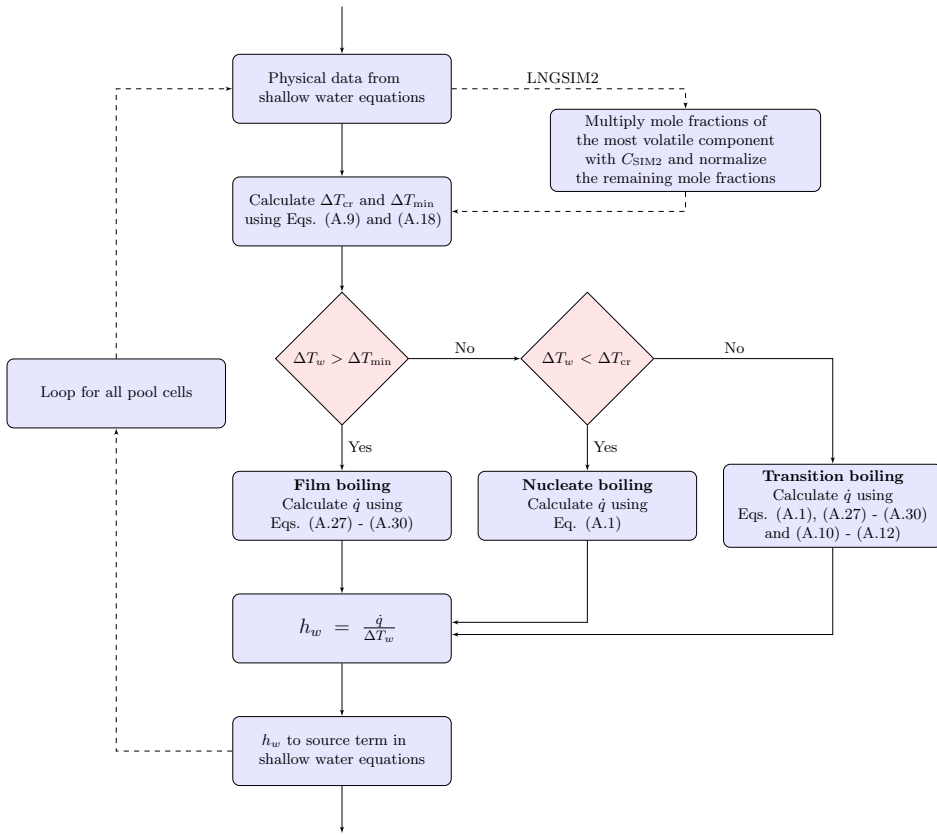


Figure 5.1: Flowchart for LNGSIM1 and LNGSIM2.

the film boiling regime and too high heat fluxes for the nucleate boiling regime, something which will also affect the calculated transition boiling heat flux.

To take the effect of the concentration boundary layer into account a simple model is proposed. In the current KFX version, only the bulk concentrations are calculated, thus the concentrations at the liquid-vapor interface are unknown. Fig. 5.2 shows the qualitative overview of the concentration boundary layer; X_I represents the interface concentrations and X_b represents the bulk concentrations. As the concentration of the most volatile component is less at the interface than in the bulk liquid, the approach is to use a factor to reduce the concentration of this species at the interface and then normalize the rest of the species accordingly.

The method of LNGSIM2 is based on LNGSIM1 and the use of a factor $0 < C_{SIM2} < 1$ to change the concentrations used in the calculations from the bulk concentrations to the (unknown) interface concentrations. The transformation is done in the following way:

1. Multiply the concentration of the most volatile component by C_{SIM2} ($0 <$

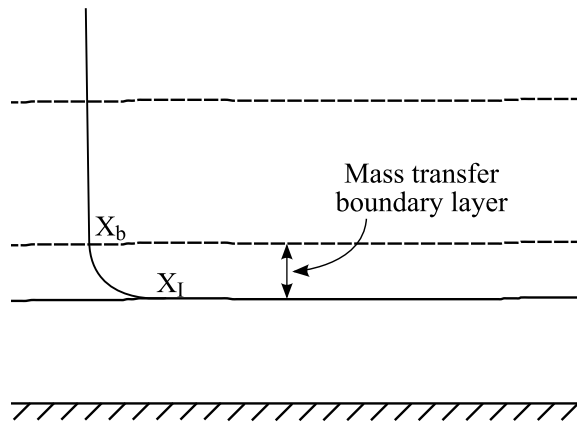


Figure 5.2: Qualitative overview of the concentration boundary layer.

$C_{SIM2} < 1$).

2. Normalize the remaining components so that they are mutually as large as they were in the bulk liquid.
3. Use these new concentrations instead of the bulk ones to calculate the heat transfer.

This is done in an attempt to increase the heat transfer to the liquid pool by changing the concentrations used in the calculations, thus simulating a concentration boundary layer. C_{SIM2} has to be given *a priori* and is therefore representing a source of uncertainty that has to be analyzed in more detail. This is done in Sec. 7.5.

6 Spreading of cryogenic liquid on water

Several models have been proposed for the pool spreading of a liquid on both water and solid grounds, most of them assuming a circular spread driven only by gravity and ignoring any effects from wind, waves or currents (e.g. [35, 36]). Modeling pool spreading in this way usually end up in one explicit equation for the pool radius. These assumptions usually work fairly well, but using such specific models might be erroneous for complex cases.

6.1 The Shallow Water Equations

A more general pool spreading model is the shallow water equations, which are based on the use of the incompressible Navier-Stokes equations in two dimensions. They are obviously more time-consuming than the previously mentioned models, as they take more physical effects (e.g. viscous forces) into account. The most fundamental simplification is that the length scale normal to the liquid pool (liquid height) is a lot less than the radial length scale (pool diameter), implying that the velocity scale in the z-direction is small compared to the velocity scale in the other directions. This allows for integration of the governing equations in the z-direction and the use of average quantities for the liquid height in the pool.

Vikan [37] compared the shallow water equations to the previous pool spreading model incorporated in KFX. He concluded that the KFX model failed to describe the spreading correctly in the early stages of a run because it did not include the inertia forces in the liquid. With respect to this, a new version of the shallow water equations has been implemented in KFX [38]:

$$\frac{\partial}{\partial t} (q_i) + \frac{\partial}{\partial x_j} (F_{ij}) = S_i, \quad (6.1)$$

where

$$q_i = \begin{pmatrix} m'' \\ m'' u_x \\ m'' u_y \\ m'' T_l \\ m''_k \end{pmatrix} \quad F_{ij} = \begin{pmatrix} m'' u_x, & m'' u_y \\ m'' u_x^2 + \frac{g}{2\rho} m''^2, & m'' u_x u_y \\ m'' u_y u_x, & m'' u_y^2 + \frac{g}{2\rho} m''^2 \\ m'' T_l u_x, & m'' T_l u_y \\ m''_k u_x, & m''_k u_y \end{pmatrix} \quad (6.2)$$

and

$$S_i = \begin{pmatrix} -\dot{m}''_{\text{vap}} \\ -\tau_x - gm'' \frac{\partial b}{\partial x} - \dot{m}''_{\text{vap}} u_x \\ -\tau_y - gm'' \frac{\partial b}{\partial y} - \dot{m}''_{\text{vap}} u_y \\ \frac{1}{c_{pl}} \left[E (\dot{q}_{\text{rad}} - \sigma_{\text{SB}} T_l^4) + h_{\text{amb}} (T_{\text{amb}} - T_l) + \right. \\ \left. h_w (T_w - T_l) - \sum_k h_{\text{fg},k} \dot{m}''_{\text{vap},k} \right] - T_l \dot{m}''_{\text{vap}} \\ \dot{m}''_{\text{vap}} \end{pmatrix}. \quad (6.3)$$

To verify this pool spreading model, stand-alone simulations have been conducted with realistic outcomes and comparisons of spreading time with experimental data give good results. The model is also found to be stable and robust [38]. It is an attractive model since it incorporates spreading of multicomponent liquids, including conservation equations for each species on a general basis. Discretization of Eqs. (6.1) – (6.3) are done using Rusanov’s method (Sec. 6.1.1).

In Eqs. (6.2) and (6.3) the subscripts i and j is part of the tensor notation while k is the index for the various liquid components. The last equation in Eqs. (6.2) and (6.3) thus represents as many equations as there are species in the liquid phase. The viscous drags, τ_x and τ_y , representing both the drag between the air and the liquid pool and between the water and the liquid pool, will affect the spread by slowing it down for relatively large values.

The spreading model should be tightly connected to the heat transfer model in order to describe the physics correctly. For correct physics, a high heat transfer coefficient between the ground or water to the liquid should imply that the spreading will subside quicker than for a low heat transfer coefficient. This behavior is incorporated in the source term, S_i , in Eq. (6.3) through the heat transfer coefficient h_w ; a large negative source due to a high heat transfer coefficient means that lots of liquid is evaporating, thereby preventing or slowing down the spread, while a low heat transfer coefficient promotes further spread.

This work focuses on determining h_w for insertion into Eq. (6.3). If h_w is known it is easy to calculate the heat transfer from the water to the LNG, represented by the term $h_w (T_w - T_l)$. Ch. 5 describes two heat transfer models implemented in KFX to calculate h_w . Simulations using these models are performed in Ch. 7 and the results are thereafter compared to experimental data from Burro 8 in the Burro test series. The other heat transfer mechanisms, radiation represented by the term $E (\dot{q}_{\text{rad}} - \sigma_{\text{SB}} T_l^4)$ and convective heat transfer from the air to the liquid pool represented by the term $h_{\text{amb}} (T_{\text{amb}} - T_l)$, are taken care of by other submodels in KFX.

6.1.1 Rusanov’s method

The shallow water equations for pool spreading are solved using Rusanov’s method (local Lax-Friedrich). This method is less numerical dissipative than Lax-Friedrich and other comparable methods. It is given by the set of equations [38]

$$\frac{dq_{i,p}}{dt} = \sum_j \frac{1}{\Delta x_j} (F_{ij-} - F_{ij+}) + S_i(q_m), \quad (6.4)$$

$$F_{ij+} = \frac{1}{2} [F_{ij}(q_{m,j+}) + F_{ij}(q_{l,p})] - |\Lambda_{ij+}| (q_{i,j+} - q_{i,p}), \quad (6.5)$$

$$F_{ij-} = \frac{1}{2} [F_{ij}(q_{l,j-}) + F_{ij}(q_{l,p})] - |\Lambda_{ij-}| (q_{i,p} - q_{p,j-}), \quad (6.6)$$

$$|\Lambda_{ij}| = \max_{x_{ij-}, x_{ij+}} \left(\max \left(\left| \lambda_1^{ij} \right|, \left| \lambda_2^{ij} \right| \right) \right), \quad (6.7)$$

and

$$\lambda_{1,2}^{ij} = u_{ij} \pm \sqrt{\frac{gm''}{\rho}}, \quad (6.8)$$

where - and + refers to the cell faces to the left and right, respectively. Rusanov's method is described in more detail in, for example, [20].

7 Simulations

Few large scale experiments have been conducted to investigate pool spreading, evaporation and vapor dispersion from an LNG pool on open water. Thyer [39] summarized the experimental data on spreading and evaporation of cryogenic liquids on different surfaces. Several experimental data types can be used as reference values in order to validate the heat transfer models described in Ch. 5, for example the temperature and the liquid concentrations just above the water surface. An interesting secondary value is the downstream concentration of hydrocarbons in the ambience due to dispersion of the vaporized LNG, as it can be used to estimate the distance to the LFL for risk assessment.

7.1 The Burro test series

In this work, experimental data from the Burro test series have been chosen as reference data. There were three types of gas sensors deployed in the Burro test series; one infrared type and two types of general hydrocarbon sensors. The infrared sensors were developed at the Lawrence Livermore Laboratory itself for use in dense fog areas, which is the case for an LNG spill. They were found to measure the gas concentrations better than the others, but they were expensive and therefore not used at all measurement towers. Six of the towers in the two first arrays (see Fig. 7.1) were equipped with the infrared sensors [40].

Some of the general hydrocarbon sensors' readings were affected by humidity, but this effect was corrected for by using other readings for humidity. Another effect affecting the readings was sensitivity to the heavier hydrocarbons ethane and propane. In the worst case, the readings was 40 times higher than in reality, nine of the sensors having sensitivity ratios of 17 or more. By investigating this effect in advance, the researchers were able to correct for this as well. The best estimate of the uncertainty for concentrations below 5% is 20 – 30% and for concentrations above 5% as much as 50%, varying greatly from sensor to sensor. Unfortunately it is not stated in [40] which towers had the infrared sensors and which had the general hydrocarbon sensors.

The water basin in the Burro test series had an average diameter of 58 m with an average water depth of approximately 1 m, the water line being 1.5 m below the surrounding ground level. This is likely to make the assumption of no ice formation coarse, but it is still an assumption in both LNGSIM1 and LNGSIM2. The terrain downwind of the spill point experienced a height increase to about 7 m above the water level 80 m downstream, remaining relatively level thereafter [33].

7.2 Setting up the Burro case

The Burro test series were conducted in order to investigate the dispersion of the vapor generated in a cryogenic liquid pool [40]. Instrumentation was distributed amongst several stations in the terrain where the LNG vapor was likely to arrive at regular wind conditions. Lots of data were acquired during the tests, including hydrocarbon concentrations, temperatures, wind field data, turbulence, humidity and heat flux from the ground to the cold vapor. The concentration data report only the total gas concentration at various points. Measurement towers were placed in the terrain as shown in Fig. 7.1. The first row is 57 meters downstream of the spill point, consisting of seven towers for concentration measurements (G09, G02, G05, T02, G04, G01 and G08), while the second row is 140 meters downstream, also consisting of seven towers for concentration measurements (G11, G07, T04, G06, T03, G03 and G12), both rows listed from the southernmost to the northernmost towers.

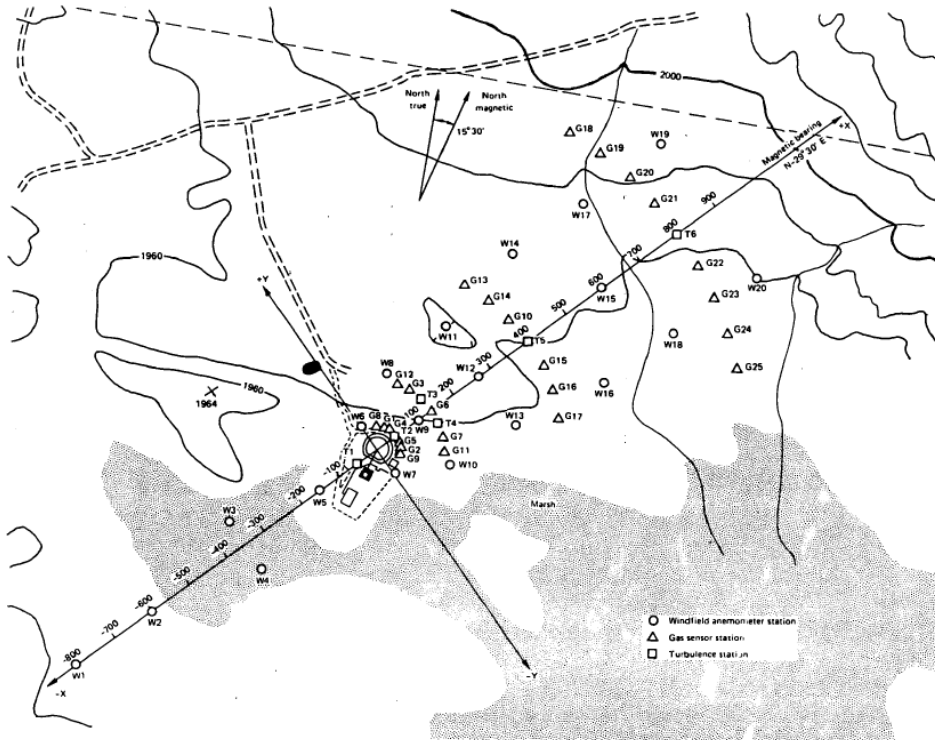


Figure 7.1: The terrain in the Burro test series as given in [40]. Measurement stations are placed along the likely wind direction.

The terrain in the Burro test series was imported into KFX as a geometry file to model the actual terrain, the orientation of it coinciding with the x- and y-axis used in the Burro test series. Fig. 7.2 shows how the relative directions and the

wind direction for Burro 8. This geometry together with an imposed wind field will determine the values of the hydrocarbon concentrations throughout the calculation domain.

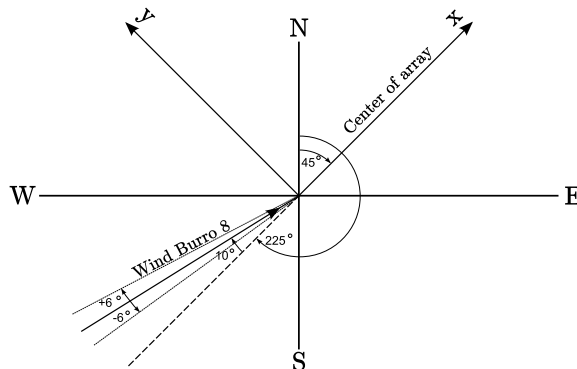


Figure 7.2: Relative directions in the Burro test series and the Burro 8 wind direction.

To initialize the wind field in KFX, the Obukhov length, the surface roughness, the surrounding temperature and the velocities in the x - and y -direction 10 meters above the surface have to be given. The Obukhov length describes stability of the wind field by relating the buoyancy forces and the inertia forces in the wind field [41]. If the Obukhov length has a small, negative value the wind surface layer is very unstable due to large buoyancy forces. Large, negative values describes slightly unstable situations and positive values describes stable situations. KFX can currently only handle positive values of the Obukhov length, which makes only Burro 8 applicable for reference data. The surface roughness length is stated to be approximately constant as 0.205 mm for all experiments [33].

7.3 Burro 8

Because of the relatively low wind speed, the Burro 8 gas cloud extended about 40 m upstream as well as beyond the outer towers of the array, but it was still centered in it. Several of the gas sensors at 3 m height did not measure any hydrocarbons before about 100 s, even though the corresponding at 1 m had readings at 20 s, indicating that the height of the gas cloud was relatively low. Table 7.1 summarizes the main parameters for the wind field and the LNG spill in the Burro 8 test case that were used in the simulations [33]. There are no experimental data for gas concentrations at tower G05 for Burro 8 and it is therefore disregarded in the simulations.

As KFX needs the velocity of the air in the x - and y -direction at $z = 10$ m the value given at $z = 8$ m (2.40 m/s) has been extrapolated to 2.50 m/s at $z = 10$ m. Decomposing this velocity in the x - and y -direction by an angle of 10° relative to the x -axis (see Fig. 7.2) results in $u_x = 2.462$ m/s and $u_y = 0.434$ m/s. This, together with the surface roughness length of 0.205 mm, the latitude of California

(36°), and the Obukhov length and the surrounding temperature from Table 7.1 gives the logarithmic velocity profile in KFX.

Table 7.1: Burro 8 summary sheet.

LNG composition	$X_{\text{CH}_4} = 87.4\%$	$X'_{\text{CH}_4} = 77.3\%$
	$X_{\text{C}_2\text{H}_6} = 10.3\%$	$X'_{\text{C}_2\text{H}_6} = 17.1\%$
	$X_{\text{C}_3\text{H}_8} = 2.3\%$	$X'_{\text{C}_3\text{H}_8} = 5.6\%$
Spill rate	16.0 m ³ /min = 116.268 kg/s	
Spill duration	107 s	
Average wind direction	235° ± 6°	
Average wind speed	1.8 ± 0.3 m/s	
Upwind vertical profile	At 1 m: 1.63 m/s	
	At 3 m: 1.94 m/s	
	At 8 m: 2.40 m/s	
Obukhov length	16.5 m	
Surrounding temperature	33.1°C	

The friction velocity calculated from the input to KFX is 0.075 whereas the one stated in [40] is 0.074, indicating that the input is correct. To ensure that the wind field is stabilized in the simulation, the spill is not started until 400 seconds have passed. This is important to get the dispersion of the LNG vapor correctly calculated and to minimize the errors from the wind field. The experimental data from the first two station rows at both 1 and 3 m have been chosen as reference values for the numerical results.

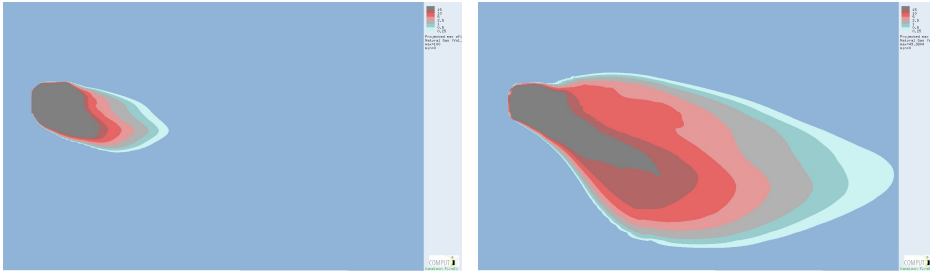
Some of the gas sensors reached saturation in some parts of the run and was therefore unable to report concentrations above a certain level (e.g. G09, G08 and G11, all at $z = 1$ m). After the 400 seconds have passed, the valve opens and the LNG is poured onto the water at a constant spill rate of 116.268 kg/s for 107 seconds, as was the case for Burro 8.

7.4 Simulations using LNGSIM1

LNGSIM1 is based on the equations for pool boiling heat transfer of pure liquids given in App. A and the use of the mixture properties of the LNG. The model is described in more detail in Sec. 5.1 and it is used as a reference model for the rest of the simulations in this chapter.

When LNGSIM1 is used to simulate the Burro 8 test case, the calculated vapor cloud becomes too narrow compared to the real one. Because of this, no

hydrocarbon vapor is detected at G03 or G12 in this simulation. Fig. 7.3 shows the vapor cloud 100 s and 300 s after the spill starts. The width of the vapor cloud is connected to the pool area, which in turn is connected to the heat transfer from the water to the LNG (see Sec. 6). Therefore, an increase in the heat transfer coefficient, h_w , causes the pool area to decrease and the vapor cloud to narrow and vice versa.



(a) 100 s after spill start.

(b) 300 s after spill start.

Figure 7.3: Calculated hydrocarbon concentrations in Burro 8 using LNGSIM1. Legend varies from 0.25% (light blue) to 100% (grey).

There are several possible reasons for the vapor cloud being too narrow: (1) the $k-\varepsilon$ model in KFX might produce too narrow clouds for large scale simulations; (2) the wind direction and velocity are always constant in the simulation whereas in reality they were not; (3) LNGSIM1 might produce incorrect pool areas due to inaccuracies in the calculations of h_w ; and (4) other things, for instance the model of the terrain might be in some error, thereby affecting the spreading direction of the cloud.

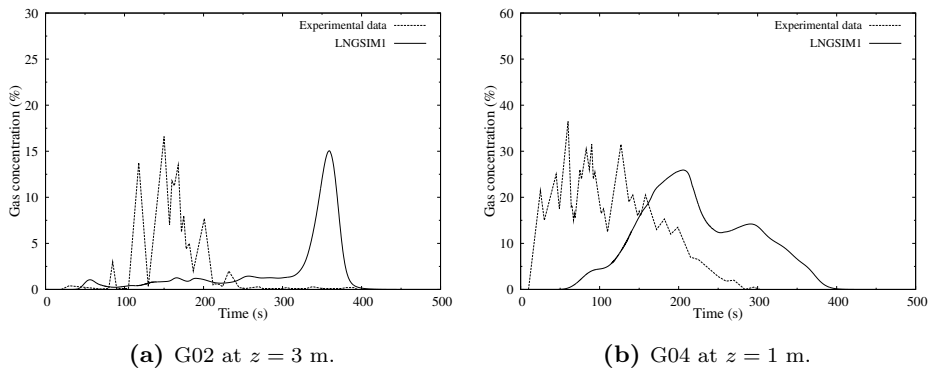
(a) G02 at $z = 3$ m.(b) G04 at $z = 1$ m.

Figure 7.4: Shapes of the concentration curves are similar to the experimental data but are often shifted in time when using LNGSIM1.

The calculations show that the shape of the concentration curves often are similar to the experimental data, but they are somewhat shifted in time. Fig. 7.4 gives two typical examples of this. At G02 the shape seems to have been shifted

about 200 seconds, while for G04 the time shift is near 100 seconds. Several other data acquisition nodes also experience such time shifting to a lesser degree, usually in the beginning of the run.

This time shifting might be a result of the heat transfer coefficient being too low. Both G02 and G04 are located in the first tower array which is more tightly connected to the vapor generation dynamics than the ones farther downstream. The farther away from the vicinity of the vapor generation one gets, the more important the vapor dispersion and the turbulence become.

Calculated boiling regimes are both film boiling and transition boiling. In the beginning of the simulation, the boiling regime for almost all cells are calculated to be film boiling, but when the LNG has aged for some time, generally at the outskirts of the liquid pool, the calculated boiling regime is usually transition boiling. This change is expected, since the concentration changes affect the calculations of ΔT_{CR} and ΔT_{min} and ΔT_w is decreased as the local boiling point increases. Because of the concentration changes, the calculated transition boiling heat fluxes are sometimes lower than the film boiling heat fluxes and vice versa.

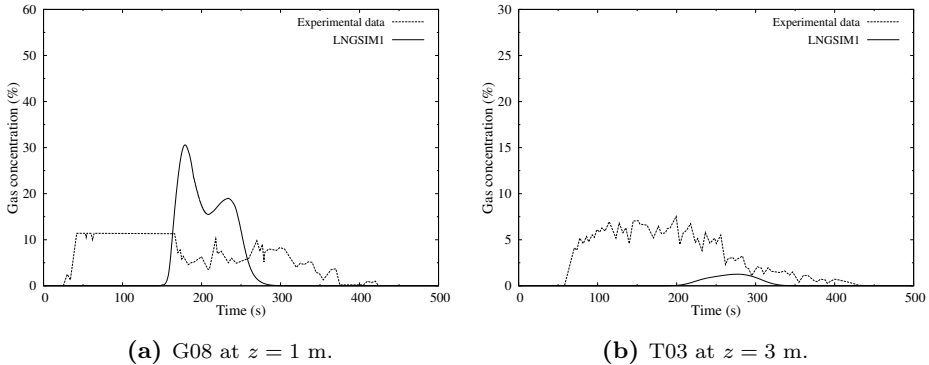


Figure 7.5: Results at the uppermost nodes in the vapor cloud using LNGSIM1.

Towards the end of the run, the overall heat flux increases drastically due to the boiling process tending towards the maximum point of the boiling curve. This forces a lot of LNG to evaporate at the end of the LNG pool's life. The overall evaporation rate is discussed in more detail in Sec. 7.8.

Since the vapor cloud does not cover towers G03 and G12, G08 and T03 are the uppermost nodes and G09 and G11 the lowermost nodes detecting any hydrocarbon vapor (see Fig. 7.1). The results at the uppermost nodes, G08 and G03, are in general matching the experimental data very poorly as shown in Fig. 7.5. Considering that the vapor cloud barely touches these locations, whereas in reality they were fully covered by it, this is not too surprising. Results at the lowermost nodes of G09 and G11 fit the experimental data a lot better, but the peak values are missed as shown in Fig. 7.6. The calculated concentrations at $z = 1$ m for these two nodes fits experimental data well, but any conclusions are uncertain due to the gas sensors reaching saturation. The good results for G09 and G11, compared to those of G08 and T03, are probably due to the vapor cloud fully covering the

towers. This is also the general case; the results from the towers where the vapor cloud fully covers it are better than the ones at the outskirts.

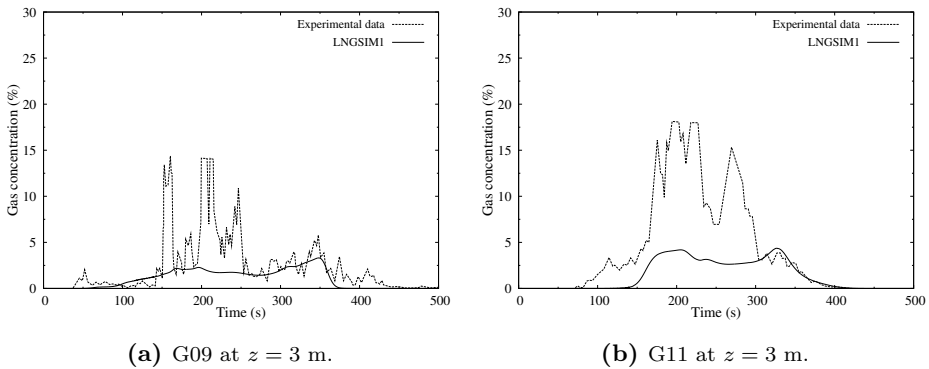


Figure 7.6: Results at the lowermost nodes in the vapor cloud using LNGSIM1.

At $z = 3$ m for some of the towers, the concentrations experience a peak towards the end of the run (see Fig. 7.7). This is likely to be a consequence of the rapid increase in the evaporation rate at the end of the LNG pool's life, something which is discussed in more detail in Sec. 7.8.

From the plots given here, it is clear that the concentrations at a given point oscillates somewhat with time. These oscillations origin not only from the dynamic nature of LNGSIM1, but also numerical issues. LNGSIM1 will produce heat transfer coefficients that vary a lot with time and concentrations for a given pool cell. The heat transfer coefficient affects the concentrations, which in turn affects the heat transfer coefficient and so forth. This behavior will create both a general trend and smaller oscillations within this trend. The numerical oscillations, on the other hand, will only contribute to the small oscillations. In Secs. 7.9.2 and 7.9.3 a short analysis of the simulations' sensitivity to a change in the time step and the grid cell sizes are presented. There, it is concluded that the general trend in the gas concentrations are likely to be little affected by the choice of gridding and time step, indicating that the general influence of any numerical oscillations are small.

At the second tower array, the gas concentration results are in general better than at the first one. This is not owed to the heat transfer model, but is rather a result of the $k-\varepsilon$ model capturing some of the real physics; the gas will be dispersed and diffused farther downstream, making the concentration curves smoother. Both the experimental results and the simulations more or less incorporate this effect. Since the first tower array is more sensitive to fluctuations in the calculated heat transfer coefficients, it is encouraging that the simulation results are not too far off, except at the outermost nodes.

LNGSIM1 produces decent results for the downstream gas concentrations at most data acquisition nodes, except for the ones barely covered by the vapor cloud. The most intriguing benefit from using LNGSIM1 is that the heat transfer coefficient does not need to be given *a priori*, which is the case for the current KFX model. The potential for improvement of LNGSIM1 is huge, however, which is why

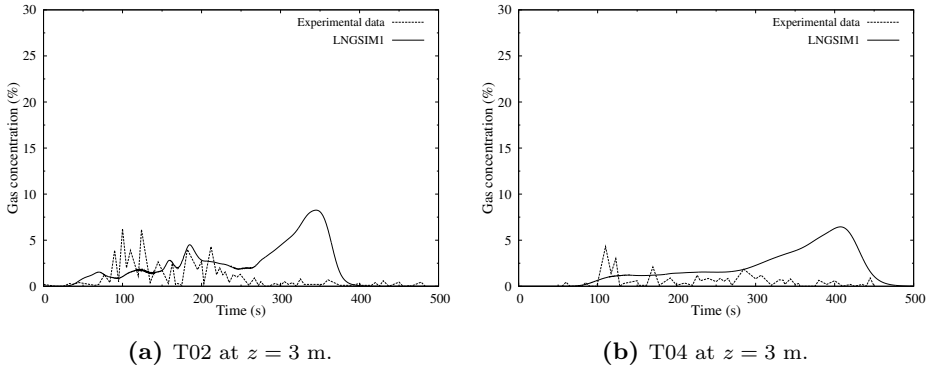


Figure 7.7: Some of the data acquisition nodes at $z = 3$ m experience a rise in concentrations towards the end of the run when using LNGSIM1.

simulations using LNGSIM2 have been conducted accordingly.

7.5 Simulations using LNGSIM2

Simulations using LNGSIM2 for various values of $C_{\text{SIM}2}$ have been conducted as an attempt to increase the heat flux compared to LNGSIM1. LNGSIM2 uses LNGSIM1 as a foundation and tries to take the the fact that LNG is a mixture into account by using a simple model for the concentration boundary layer (see Sec. 5.2 for more details). This model should increase the heat transfer compared to LNGSIM1 because it uses higher fractions of the heavy hydrocarbons to calculate the heat transfer coefficient h_w .

That the heat transfer in fact is increased in LNGSIM2 is apparent in Fig. 7.8; using $C_{\text{SIM}2} = 0.90$ makes the concentrations increase faster and earlier than for LNGSIM1 with a concurrent earlier decrease when the LNG spill reaches its end. These observations show that LNGSIM2 work as intended, at least to some extent, because an increase in the heat transfer coefficient will make the LNG evaporate faster, hence increasing the concentrations at the data acquisition nodes faster. Concurrently, a rapid decrease in the concentrations at the later stages is experienced because all the LNG has been evaporated faster than using LNGSIM1. Using $C_{\text{SIM}2} = 0.80$ further enhances this effect, as can be seen in Fig. 7.8.

This behavior continues for continuously decreasing $C_{\text{SIM}2}$, but only until about $C_{\text{SIM}2} = 0.50$. For $C_{\text{SIM}2} = 0.40$ and below, the increase in vaporization rate does not follow a decrease in $C_{\text{SIM}2}$ orderly. In fact, $C_{\text{SIM}2} = 0.40$ and below produce some unexpected results. The calculated heat transfer coefficients are extremely large and the heat transfer to the liquid pool becomes so large that it strictly confines the pool area to the one cell where there spill source is located. Confining the pool to one pool cell greatly affects the shape of the vapor cloud and the direction in which it spreads, an effect also counting for $C_{\text{SIM}2} = 0.30, 0.20$ and 0.10 . The gas concentrations detected at most acquisition nodes are thus artificially low for $C_{\text{SIM}2} \leq 0.40$. This is clear in the examples shown in Fig. 7.8.

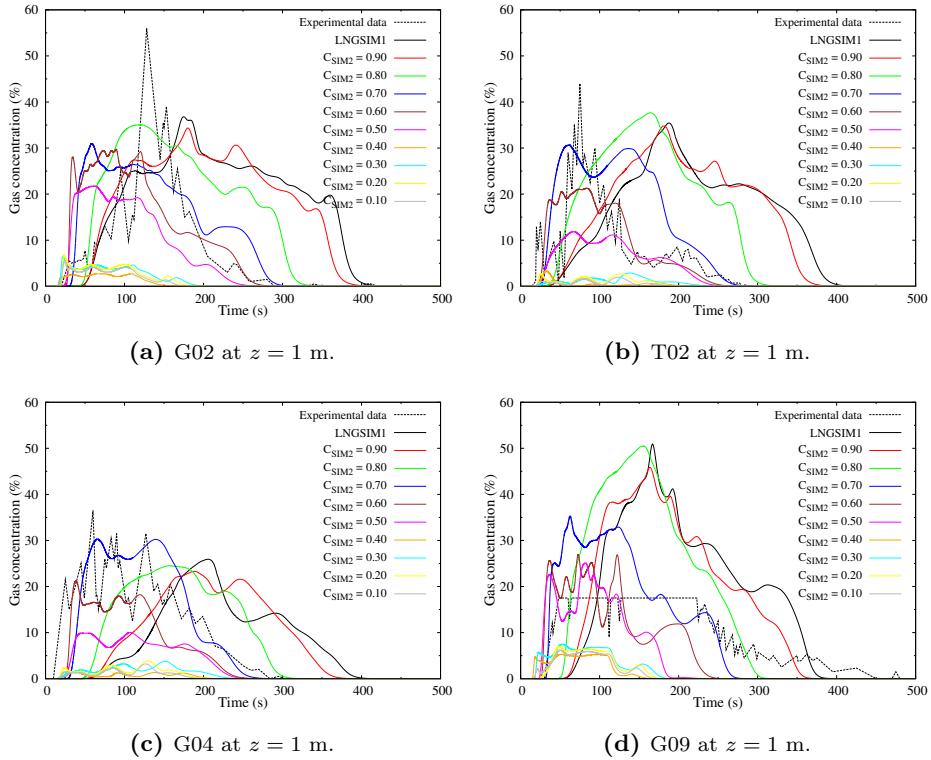


Figure 7.8: General results using LNGSIM2. $C_{SIM2} \leq 0.40$ produces artificially low concentrations at most data nodes.

Fig. 7.9 shows the vapor cloud generated for LNGSIM2 with $C_{SIM2} = 0.40$ and $C_{SIM2} = 0.30$ ($C_{SIM2} = 0.20$ and $C_{SIM2} = 0.10$ produce very similar results). As opposed to the gas cloud in Fig. 7.3, these gas clouds will obviously produce very low concentrations for several of the central nodes because of their x-shape. The reason for this shape is numerical problems combined with very large heat fluxes. Since the large heat flux strictly confines the LNG pool to one cell, lots of LNG vapor is spewed out at high velocities from that cell. These velocities will increase the numerical diffusion that leads to numerical errors, hence the peculiar x-shape arises. This could have been avoided by using a finer grid for the liquid pool. $C_{SIM2} \geq 0.50$ gives similar pool and gas cloud shapes as in Fig. 7.3. Therefore, $C_{SIM2} \leq 0.40$ is disregarded from the rest of the discussion.

Calculated boiling regimes using LNGSIM2 are almost solely transition boiling, expect for early in the run when $C_{SIM2} = 0.90$. Even though the calculations always give the same boiling regime, the change in C_{SIM2} makes the transition boiling fluxes for for instance $C_{SIM2} = 0.50$ over two orders of magnitude larger than for $C_{SIM2} = 0.80$. This happens because low values of C_{SIM2} enhance the influence of the physical properties of the heavier hydrocarbons, thereby increasing the calculated heat transfer coefficient.

Table 7.2: Agreement between experimental data and simulation data using LINGSIM2.

	Tower array 1												Tower array 2												Average
	C _{SIM2}	G09	G02	T02	G04	G01	G08	G11	G07	T04	G06	T03	G03	G12											
$z = 1 \text{ m}$	1.00 ^a	Poor*	Poor	Poor	Poor ^b	Poor	Poor*	Fair ^{b*}	Fair	Poor	Fair	Poor	NA	NA	Poor										
	0.90	Poor*	Poor	Poor	Poor ^b	Poor	Poor*	Fair ^{b*}	Fair	Poor	Fair	Poor	NA	NA	Poor										
	0.80	Fair*	Fair	Poor	Fair ^b	Fair	Poor*	Great*	Good	Fair	Fair	Poor	NA	NA	Fair										
	0.70	Fair*	Fair	Fair	Fair	Good	Poor*	Good*	Good	Good	Good	Fair	Poor	NA	Good										
	0.60	Poor*	Fair	Good	Fair	Great	Poor*	Fair*	Good	Good	Good	Good	Fair	NA	Good										
	0.50	Poor*	Poor	Fair	Fair	Poor	Poor*	Poor*	Good	Great	Great	Fair	Poor	NA	Fair										
$z = 3 \text{ m}$	1.00 ^a	Fair	Poor ^b	Poor	Fair	Fair	Poor	Poor	Poor	Poor	Fair	Poor	NA	NA	Poor										
	0.90	Fair	Poor ^b	Poor	Poor	Fair	Poor	Poor	Poor	Poor	Fair	Poor	NA	NA	Poor										
	0.80	Fair	Poor ^b	Poor	Poor	Fair	Poor	Fair	Poor	Poor	Poor	Poor	NA	NA	Poor										
	0.70	Fair	Poor	Poor	Fair	Poor	Poor	Poor	Poor	Fair	Fair	Fair	Fair	NA	Fair										
	0.60	Poor	Poor ^b	Poor	Fair	Poor	Poor	Poor	Poor	Fair	Fair	Fair	Fair	NA	Fair										
	0.50	Poor	Poor ^b	Fair	Poor	Poor	Poor	Poor	Poor	Fair	Fair	Good	Fair	NA	Fair										
Average	Poor	Poor	Poor	Fair	Fair	Poor	Fair	Fair	Fair	Fair	Fair	NA	NA	Fair											

^a C_{SIM2} = 1.00 gives LINGSIM1.

^b Results would be better if shifted in time.

* Gas sensor reached saturation. Evaluation is therefore uncertain.

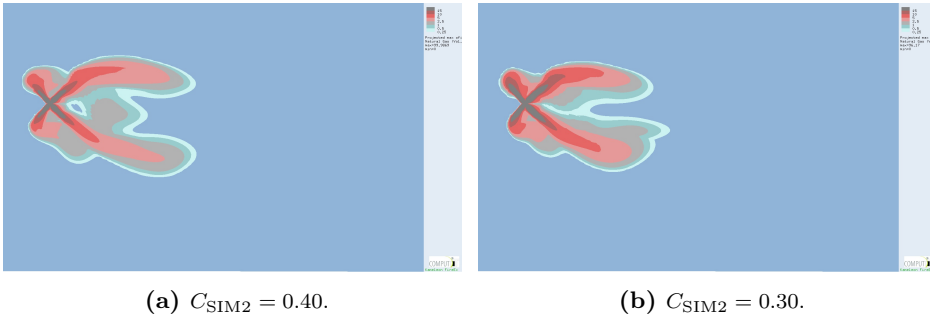


Figure 7.9: Contour plots of the vapor gas cloud when using $C_{SIM2} = 0.40$ and 0.30 , 50 seconds after the spill has commenced. Legend varies from 0.25% (light blue) to 100% (grey).

Table 7.2 summarizes how well the simulations fit experimental data at the chosen data nodes. The scale is based on visual observations of the resulting concentration graphs and how well these results fit general trends, beginnings and ends, concentration levels and maxima and minima of the experimental data, ranging from poor to great. It shows, as previously discussed for LNGSIM1, that the results in general are better and smoother at the second array than at the first array due to the dispersion and diffusion following the $k-\varepsilon$ model. Another general trend worth noting from Table 7.2 is that the results at $z = 3$ m deviate more from the experimental data than at $z = 1$ m. This likely originates in the turbulence model and the way the gas is dispersed in KFX, which is another ongoing field of study at ComputIT.

In order to find an optimized value of C_{SIM2} , more simulations have to be conducted and the results validated against more experimental data. As a preliminary conclusion, values of C_{SIM2} between 0.50 and 0.80 are subject to further investigations, based on the qualitative overview in Table 7.2. This is done in Sec. 7.10, where LNGSIM2 is combined with a factor ζ that is introduced in the next section to alter the transition boiling heat fluxes

7.6 Effect of changing the transition boiling heat flux

In Ch. 3 it was concluded that the method of interpolation for the transition boiling heat fluxes, Eqs. (A.10) – (A.12), produced abnormally large values. In an attempt to adjust this interpolation, Eq. (A.12) is written in the general form

$$\xi = (1 - \Delta T^*)^\zeta. \quad (7.1)$$

The aim of this section is thus to see how the factor ζ affects the simulation results of Burro 8.

Figure 7.10 shows boiling curves for methane using various values of ζ in Eq. (7.1). The calculations are otherwise conducted as in Ch. 3. There are two important things to note:

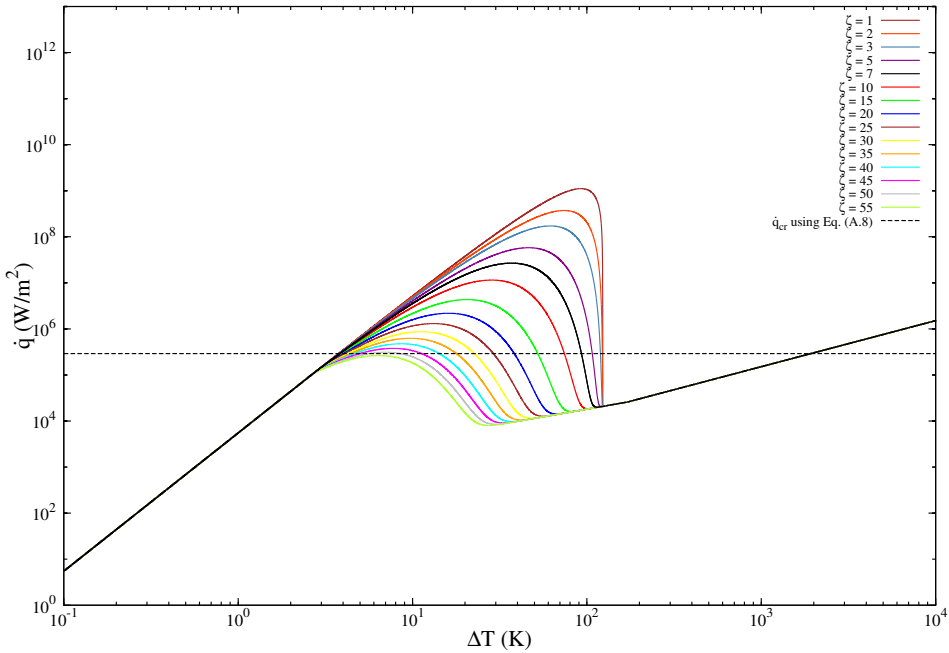


Figure 7.10: Calculated transition boiling regime for methane for different values of ζ .

1. $\zeta \approx 55$ forces the boiling curve's maximum point to coincide with the theoretical one calculated by Eq. (A.8).
2. Higher values of ζ makes the transition boiling regime more narrow and the film boiling regime wider. This will heavily influence the overall heat transfer as the heat flux decreases a lot over a wide range.

Calculations have also been conducted for ethane, propane and butane, resulting in the same conclusions as for methane. Thus, the choice of ζ is a trade-off between correcting the maximum point of the boiling curve to the theoretical value of \dot{q}_{cr} and forcing the film boiling regime start at a too low ΔT_w . Since the value given by Kalinin *et al.* [42] is 7, the interesting interval to investigate is from $\zeta = 7$ to $\zeta = 55$ (the values below 7 make the maximum point of the boiling curve even higher).

Figure 7.11 shows some general results using LNGSIM1 and varying ζ . The general trend is that the higher the value of ζ , the more alike the concentration curves become. For the standard $\zeta = 7$, $\zeta = 10$ and $\zeta = 15$ there are at some nodes clear deviations from the general trend, while for other nodes the trend is the same for all values of ζ . Figs. 7.11a and 7.11b are examples where the trend is the same for all ζ -values, while two examples of the deviating trends are given in Figs. 7.11c and 7.11d.

The size of the gas cloud varies little with ζ . For $\zeta = 15$ and $\zeta = 20$, however,

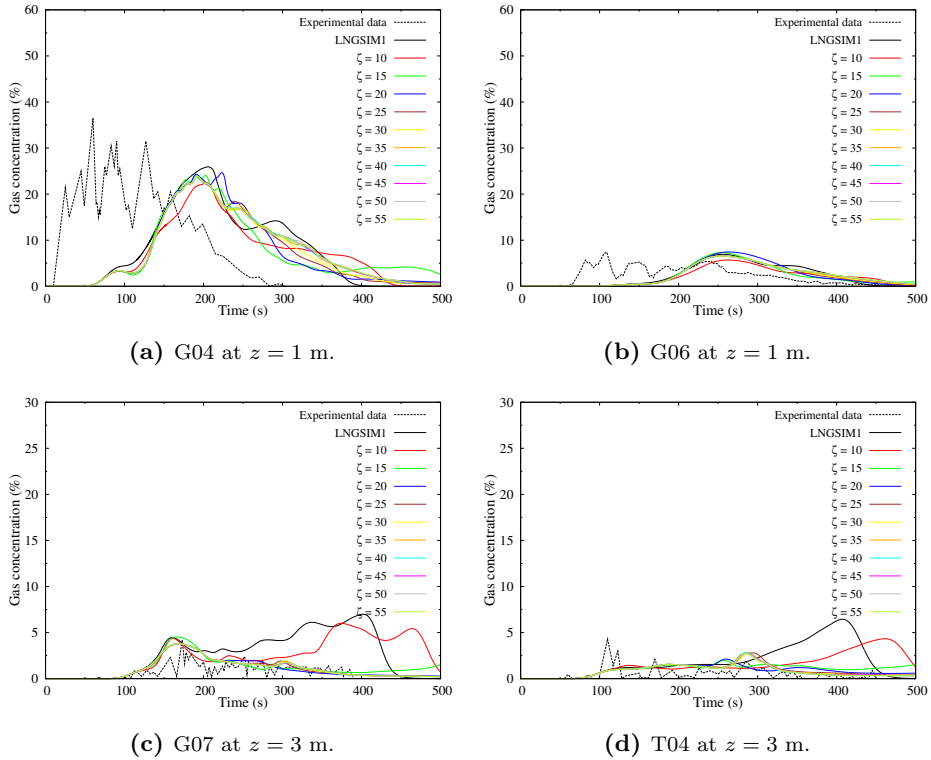


Figure 7.11: Simulation results using LNGSIM1 and varying ζ .

it barely touches the G03 node around 300 seconds after the spill start ($Y \approx 0.1\%$), indicating that there is at least some influence on it, but very small.

Considering Fig. 7.10, it can be argued why the results become more similar for increasing ζ . The higher the value of ζ , the wider the linear film boiling regime becomes, hence making the active calculation interval more and more linear, as well as forcing the maximum point on the boiling curve lower. This forces the overall heat transfer to tend towards the same values for increasing ζ . However, the higher ζ becomes, the farther away from the original model one gets and the more likely one is to produce unphysical results. The original model value of $\zeta = 7$ is adjusted to experimental data for nitrogen boiling on a Teflon surface, CCl_4 , n -pentane and Freon 113 boiling on a copper surface and Freon 113 boiling on a steel surface [42], so the possibility of ζ differing from 7 for hydrocarbon cryogenic liquids boiling on water is present.

As discussed in Sec. 7.4, LNGSIM1 produced some peaks in the concentrations towards the end of the run (see Fig. 7.7). Higher values of ζ seems to smooth out these peaks, thereby making the calculated concentration curves fit the experimental data better. It is important to note, however, that very high values of ζ prevent the concentrations from reaching zero at the proper times because the overall heat

flux is reduced a lot. Since increasing ζ seems to stabilize and smoothen the concentration curves at about $\zeta = 20$, the region between $\zeta = 7$ and $\zeta = 30$ is subject to a more in-depth investigation.

In Sec. 7.10, LNGSIM2 is combined with these values of ζ in an attempt to optimize the heat transfer model. The LNG pool area and evaporation rate are also influenced by ζ , which is discussed in Sec. 7.8.

7.7 Rapid phase transitions

As described in Sec. 4.5, rapid phase transition occurs because the LNG reaches its superheat limit. The superheat limit of a mixture can be adequately described by the mole fraction averaged quantity [23]. As the LNG composition changes, so does both the superheat limit and the boiling regime, further enhancing the superheating with an increase in the heat flux.

7.7.1 Rapid phase transitions using Burro 8 concentrations

To investigate this, the criterion for when an RPT can happen (Eq. (4.11) on page 44) has been implemented in the heat transfer models. The superheat limit is always approximated by the mole fraction averaged quantity of the bulk liquid. Several simulations have been used to investigate when the criterion is fulfilled. Table. 7.3 gives some values from three of the simulations. It is clear that the methane concentration has to fall a lot compared to the others before the criterion is satisfied.

Melhem *et al.* [1] found theoretically that for an RPT to occur in an LNG pool, the methane concentration at a given point had to be less than 0.3475 (0.2000 on mass basis). For LNGSIM1 the maximum methane concentration that produced a possible RPT was 0.3825, for LNGSIM2 with $C_{\text{SIM}2} = 0.90$ it was 0.3885 and for LNGSIM2 with $C_{\text{SIM}2} = 0.80$ it was 0.3869, which are not too far off. Fig. 7.12 shows histograms of the methane concentrations when RPTs are found to occur together with the theoretical finding of 0.3475. Practically all detections of possible RPTs are at methane concentrations lower than 0.3475. Therefore, Eq. (4.11) connects the results from the simulations and the findings from experiments and theory. One must bear in mind, however, that the theoretical value of 0.3475 was found with a different initial composition than the one used here and that this might affect the theoretical concentration limit. Results from a simulation using the initial composition in [1] are presented in Sec. 7.7.2.

The frequency of Eq. (4.11) being fulfilled is very high, which is probably a consequence of no RPTs being released. If one RPT was to be set off it would greatly affect the local composition and therefore also the rate succeeding detections. Even though RPTs are known to happen in series (e.g. in Burro 9 [33]), this is not the general case. Therefore, one should not aim to model every instance of RPTs intercepted by Eq. (4.11) as a pressure wave.

What is more intriguing is that the occurrence of an RPT is always connected to the transition boiling regime and very high heat transfer coefficients, which implies that the boiling regime has shifted some distance into the transition boiling

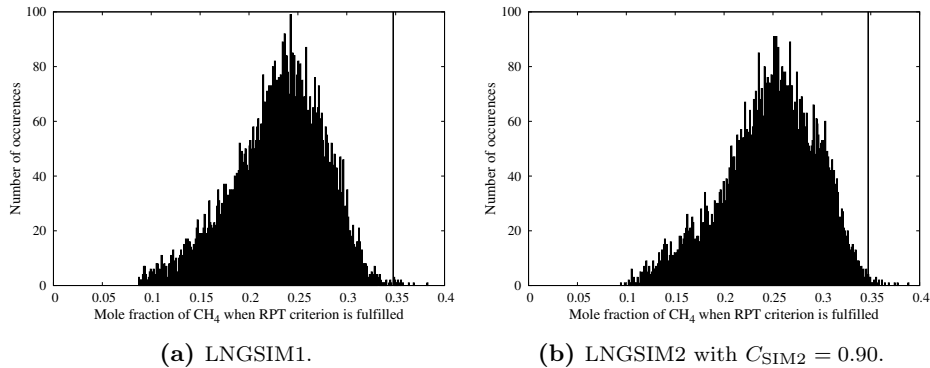


Figure 7.12: Histogram of methane concentrations when Eq. (4.11) is fulfilled.

regime from the film boiling regime. This is completely in accordance with the discussion of RPTs in Sec. 4.5.3.

A general trend to note from Table 7.3 is that the less the concentration of methane is, the higher the heat calculated transfer coefficient becomes. The calculated h_w is dependent on the concentration of the other components as well, however, making this trend diffuse. Nevertheless, this is how the model should work; the more methane that has evaporated, the higher the physical properties of the mixture becomes, thereby increasing the heat transfer coefficient and changing the boiling regime.

The simulations have not captured exactly where the possible RPTs occur, but the concentration of methane will generally be large near the spill point, and the RPTs are therefore likely to happen at the outskirts of the liquid pool where the LNG has aged for some time. This is also discussed by Melhem *et al.* [1]; longer spill durations are more likely to produce RPTs because of the ageing of the LNG.

7.7.2 RPT for a different initial composition

Since the initial LNG composition of Burro 8 differs from the one in the work of Melhem *et al.* [1], a simulation using LNGSIM1 with this initial composition has been conducted. This composition consisted of 84% methane, 12% ethane, 3% propane and 1% *n*-butane, whereas the Burro 8 composition was 87.4% methane, 10.3% ethane and 2.3% propane (all mole fractions).

Figure 7.13 shows the RPT results in the same way as in Fig. 7.12. The maximum methane concentration for a fulfilled RPT criterion was in this case 0.4378. Visual comparison between Figs. 7.12 and 7.13 shows that more RPT occurrences are above the theoretical value of 0.3475 for this initial composition, actually rendering these results in more error than the previous ones. The results are still quite good and the corresponding values of h_w are in the same order of magnitude as for the Burro 8 composition with transition boiling always being the case.

The reason for this is the following: Eq. (4.11) is only based on the mixture

Table 7.3: Typical bulk concentrations and heat transfer coefficients when Eq. (4.11) on page 44 is fulfilled.

	X_{CH_4}	$X_{\text{C}_2\text{H}_6}$	$X_{\text{C}_3\text{H}_8}$	h_w (kW/m ² K)
LNGSIM1	0.268	0.171	0.561	445552
LNGSIM1	0.287	0.262	0.451	238717
LNGSIM1	0.315	0.246	0.439	175663
LNGSIM1	0.321	0.338	0.341	95563
LNGSIM1	0.334	0.313	0.353	89143
LNGSIM2, $C_{\text{SIM}2} = 0.90$	0.172	0.352	0.476	589547
LNGSIM2, $C_{\text{SIM}2} = 0.90$	0.275	0.163	0.562	427058
LNGSIM2, $C_{\text{SIM}2} = 0.90$	0.307	0.242	0.451	199063
LNGSIM2, $C_{\text{SIM}2} = 0.90$	0.313	0.349	0.338	106428
LNGSIM2, $C_{\text{SIM}2} = 0.90$	0.357	0.265	0.378	76174
LNGSIM2, $C_{\text{SIM}2} = 0.80$	0.162	0.390	0.448	685398
LNGSIM2, $C_{\text{SIM}2} = 0.80$	0.250	0.326	0.424	441580
LNGSIM2, $C_{\text{SIM}2} = 0.80$	0.313	0.123	0.564	563297
LNGSIM2, $C_{\text{SIM}2} = 0.80$	0.315	0.367	0.318	208263
LNGSIM2, $C_{\text{SIM}2} = 0.80$	0.363	0.213	0.424	246245

superheat limit, which is approximated by the mole fraction averaged quantity in these calculations. The initial composition of Burro 8 consisted of more methane than the study in [1]. Because of this, the methane concentration has to be brought to a lower level for Burro 8 since the initial fractions of the heavier hydrocarbons are relatively lower. As an extreme example, an LNG mixture initially consisting of 99% methane and 1% propane would have to age until it consists of 27.8% methane before Eq. (4.11) is fulfilled.

Although the results in this section are encouraging it is important to remember that the RPT criterion and the heat transfer coefficients calculations are completely decoupled. That they match the physics of RPTs together is merely a consequence of the composition changes affecting both calculations. Yet, it is good that they actually do fit each other this way, making it possible that they can be used together as a simple model for when the pressure wave of an RPT should be released.

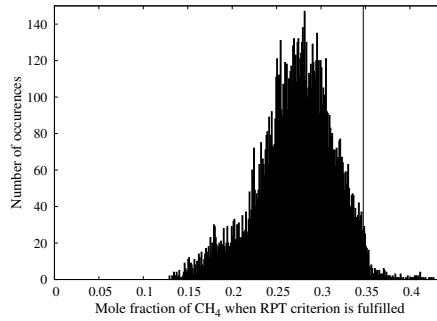


Figure 7.13: Histogram of methane concentrations when Eq. (4.11) is fulfilled using LNGSIM1 and the initial composition of [1].

7.8 Pool area and evaporation rate

The liquid pool in the current KFX version is a submodel below the calculation domain for the free flow. There, the pool area is calculated by summing up the area of any grid cells containing liquid, using the same grid as for the domain above. This implies that the calculated pool area might experience some fluctuations when the liquid spreads to another cell where the LNG instantly evaporates. Such fluctuations are apparent in Fig. 7.14.

There are little information given about the pool area of Burro 8 in neither reports from the Burro test series [33, 40]. The only information is about Burro 9 where a pool diameter of about 10 m was observed, resulting in a pool area of almost 80 m². As the authors point out, however, Burro 9 consisted of a series of RPTs and this pool area is therefore not likely to be as large as the pool area in the other tests. The area of the test basin in the Burro test series can be approximated as circular with an average diameter of 58 m, making the maximum achievable pool area 2642 m².

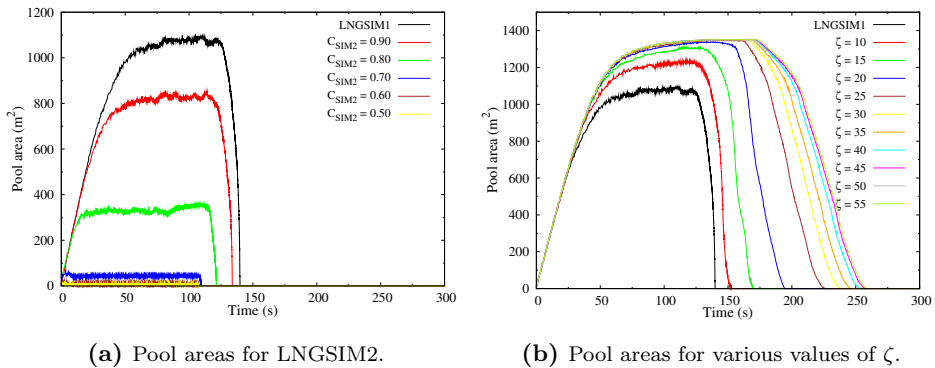


Figure 7.14: Pool areas for various values of C_{SIM2} and ζ .

Figure 7.14 shows the calculated pool areas for LNGSIM2 with various values

of $C_{\text{SIM}2}$ and for LNGSIM1 using various values of ζ . In Sec. 7.5 the simulations for $C_{\text{SIM}2} \leq 0.40$ were found to behave in unexpected ways and were therefore omitted from the discussion there. The pool areas for these simulations are virtually non-existent because of large evaporation rates and they are therefore omitted from the discussion here as well. The heat transfer rates are simply so large that the LNG flashes instantly, preventing further pool spread.

As shown in Fig. 7.14a, decreasing values of $C_{\text{SIM}2}$ make the pool area decrease as well. The vaporization rates corresponding to the pool areas using LNGSIM2 are plotted in Fig. 7.15a. As expected, and desired, the heat transfer rates in LNGSIM2 increase with decreasing $C_{\text{SIM}2}$. This is in accordance with the purpose of the model as discussed in Sec. 5.2, and it greatly affects the gas concentration calculations in Sec. 7.5. $C_{\text{SIM}2} = 0.50 - 0.60$ produces extremely high evaporation rates, an effect which confines the LNG pool to the one cell where the spill source is located. This unphysical result renders any use of $C_{\text{SIM}2} < 0.70$ useless and these values are therefore not considered when optimizing the heat transfer model in Sec. 7.10. The heavy oscillations in the evaporation rate origin from concentration changes in the liquid pool affecting the heat transfer coefficient at all pool cells for all time steps, which is then fluctuating accordingly.

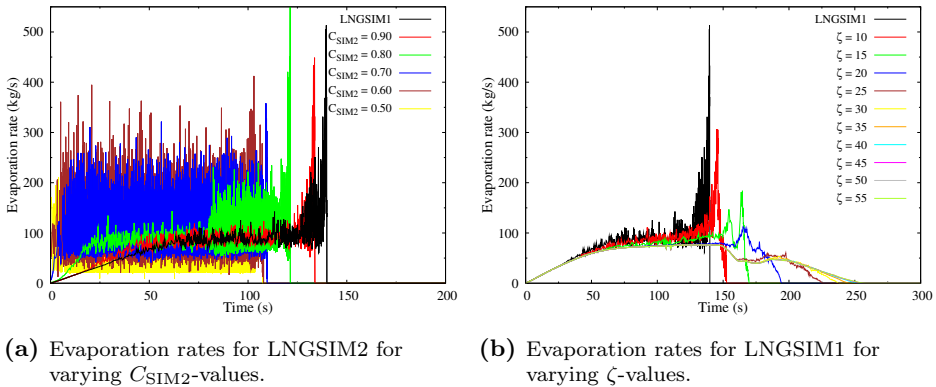


Figure 7.15: Vaporization rates for LNGSIM2 for various $C_{\text{SIM}2}$ -values and LNGSIM1 for various ζ -values.

Calculated pool areas for LNGSIM1 for various values of ζ show an increase in the pool area for increasing ζ -values (Fig. 7.14b). As discussed in Sec. 7.6 the film boiling regime stretches over a wider range of ΔT s for increasing values of ζ and the slope of this part of the boiling curve is not very steep. This makes the heat transfer coefficient tend towards a constant value and the pool areas towards the same steady state values accordingly, an effect seen as generally low evaporation rates in Fig. 7.15b. The life of the LNG pool is also extended with increasing ζ -values because the overall heat transfer coefficient is decreased due to a wider film boiling regime. This also counts for increasing values of $C_{\text{SIM}2}$; the calculated heat transfer coefficients decrease and the pool area and its life is thus increased.

Oscillations of the evaporation rate are dampened by increasing ζ -values as

shown in Fig. 7.15b. This happens, as discussed earlier, due to the linear film boiling regime being stretched over a wider range of ΔT s. As it is desired to decrease C_{SIM2} in order to increase the heat flux and increase ζ to force the maximum point on the boiling curve to decrease, these two parameters might work well together in stabilizing the overall boiling process, a study performed in Sec. 7.10.

7.9 Sensitivity analyses

In this section, some sensitivity analyses of LNGSIM1 and LNGSIM2 are presented. These include studies of steady state, changes in the maximum allowed time step and number of grid cells, how a constant h_w and treating LNG as pure methane affects the results and changes in the surface roughness of the solid construction cells forming the terrain.

7.9.1 Steady state

Two simulations with the aim to investigate how the heat transfer models acts towards steady state have been conducted by the use of LNGSIM1 and LNGSIM2 with $C_{\text{SIM2}} = 0.90$ (because of limited time, the simulation with LNGSIM2 had to be stopped after 1100 seconds). Fig. 7.16 shows some regular gas concentrations at the first tower array. For LNGSIM1, the concentrations (the gas cloud) do only reach a quasi-steady situation within the chosen limit of 3500 seconds. When using LNGSIM2 with $C_{\text{SIM2}} = 0.90$, on the other hand, the concentrations at a given point fluctuate a lot less than for LNGSIM1. It is uncertain how the concentration trends would be for LNGSIM2 after $t = 1100$ s (the gas concentrations at some nodes started to fluctuate more at about this time for LNGSIM1).

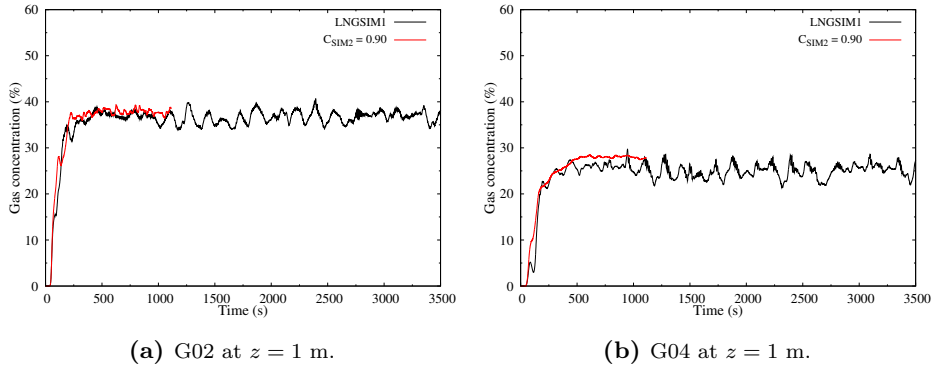


Figure 7.16: Gas concentration results for steady state simulations.

LNGSIM1 produces a steady pool area whereas the one for LNGSIM2 resides in a quasi-steady state (Fig. 7.17a). These differences occur due to the evaporation rate for LNGSIM2 fluctuating a lot more than for LNGSIM1 (Fig. 7.17b), which in turn occurs because the heat transfer coefficient fluctuates more for LNGSIM2 due to the model being closer to or in the transition boiling regime most of the time.

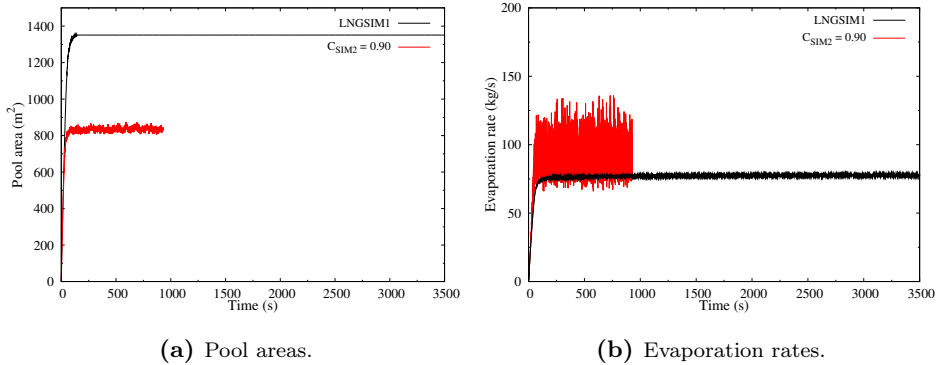


Figure 7.17: Pool areas and evaporation rates for steady simulations.

It is unclear why the downstream gas concentrations fluctuate more when using LNGSIM2 with $C_{\text{SIM2}} = 0.90$ than LNGSIM1. For LNGSIM2 the evaporation rate fluctuates a lot, thereby forcing the pool area to fluctuate a lot, and the downstream gas concentrations should therefore also fluctuate a lot, yet they do not. For LNGSIM1 the opposite is true. The steady pool area and quasi-steady evaporation rate produce lots of fluctuations in the downstream gas concentrations. This might indicate that the concentrations within the liquid pool do not reach a steady state even though the pool area does. Hence, the heat flux and evaporation rate will fluctuate in different areas of the pool, making the downstream concentrations fluctuate for a given point as well (only the total evaporation rate from the pool is reported in Fig. 7.17b).

7.9.2 Changing the maximum time step

Before running a simulation in KFX, the maximum Courant number (Sec. 2.10.3) and the maximum and the minimum time steps have to be set. In all the simulations in this chapter the maximum Courant number is 4, the maximum time step is 0.4 s and the minimum time step is 5 ms. To validate whether these values are chosen too coarse or if the results in this chapter are influenced by numerical issues, two simulations using LNGSIM1 with maximum time steps of 0.2 s and 0.1 s with a corresponding maximum Courant number of 4 have been conducted. If the grid is adequately fine, shorter time steps are usually resulting in better numerical stability, but only until the extent where lowering the time step further produces the same results.

Figure 7.18 shows two of the concentration curves that deviate the most from the original results of LNGSIM1. It is clear that both halving and quartering Δt_{max} gives the very same trends as LNGSIM1 does, which is also the general result at all the data nodes.

These results show that the general trends in the concentrations plots are not much affected by the choice of maximum time step. Some local deviations must be expected, however, but as long as the maximum time step and the maximum

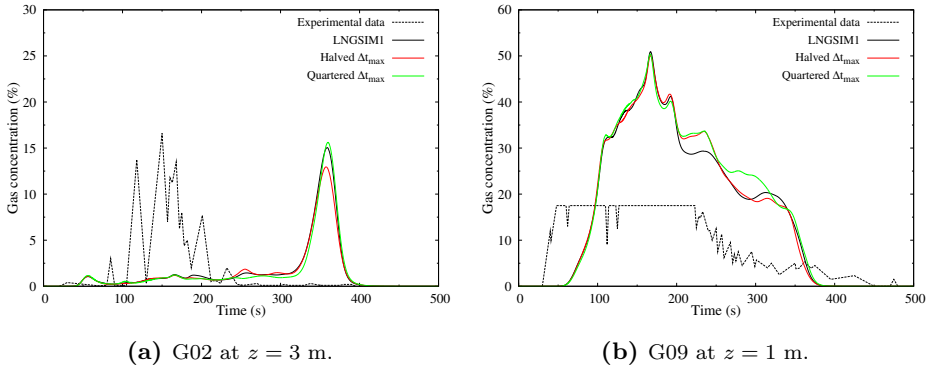


Figure 7.18: Some simulation results for halved and quartered maximum time step.

Courant number are chosen properly, the general results and trends will be clear. These findings are likely to be applicable to the rest of the simulations in this chapter as well.

Increasing the time steps, on the other hand, might lead to numerical instabilities, which is why two simulations for both double and triple maximum Courant numbers and maximum time steps were conducted as well. These simulations faltered, however, due to numerical issues. It therefore seems that the chosen values of $C = 4$ and $t_{\max} = 0.4$ is adequate for the chosen grid.

7.9.3 Reducing number of grid cells

To see how the model is affected by a coarser grid, a simulation where the number of grid cells have been halved in every direction, thereby reducing the total number of grid cells by a factor of eight, has been executed.

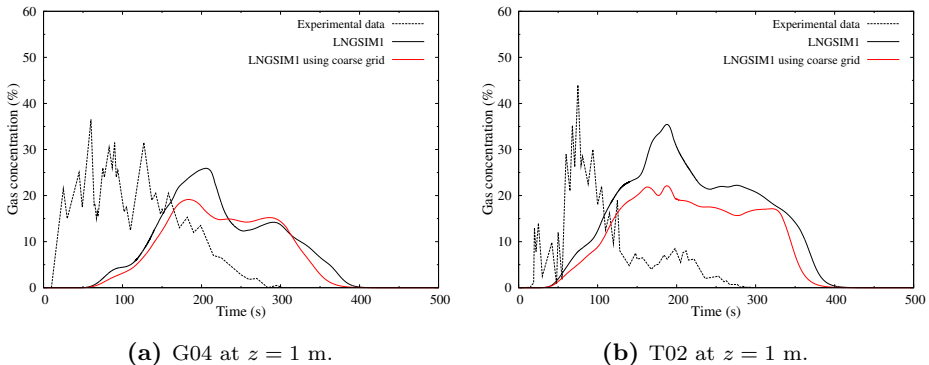


Figure 7.19: Results using a coarse grid with LNGSIM1.

Figure 7.19 shows two examples for the coarse grid compared to the regular, finer one. The trends in gas concentrations are similar for the two runs, which

is also the general result at all nodes. Both the trend of time shifting and rise in concentrations towards the end of a run, as discussed in Sec. 7.4, are reproduced on the coarse grid. This indicates that the general trend in downstream gas concentrations is little affected by the size of the grid cells.

This result together with the results from Sec. 7.9.2, indicate that LNGSIM1 is relatively unaffected by the numerics, always producing the same general trends in gas concentrations. More simulations have to be done with other grids and time steps to make this statement clearer.

7.9.4 Constant h_w

Since both LNGSIM1 and LNGSIM2 are dynamic models that calculate the heat transfer from the water to the LNG based on the composition at a given time and place, it is interesting to see how the downstream concentrations in Burro is affected by setting the heat transfer coefficient as a constant. For this purpose, the value of $165 \text{ kW/m}^2\text{K}$ has been chosen, since this was a regular value of the heat transfer coefficient when using LNGSIM1.

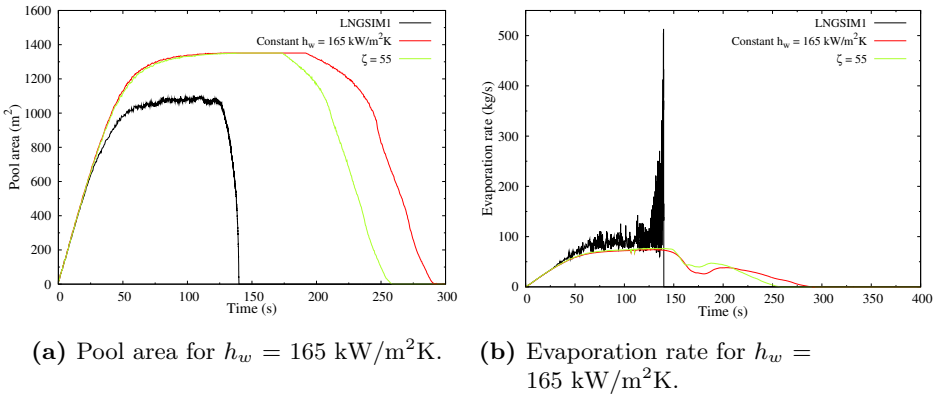


Figure 7.20: Pool area and evaporation rate for constant h_w and LNGSIM1 with $\zeta = 55$.

Figure 7.20 shows the calculated pool area and evaporation rate for constant h_w and the previous calculations for LNGSIM1 with $\zeta = 55$. There are clear similarities between these calculations. The pool areas peak at the same value and declines at almost the same rate and the evaporation rates follow the same progression. As discussed in Sec. 7.6, the boiling curve becomes more linear for a wider interval of ΔT s for greater values of ζ . The slope of the film boiling part of the boiling curve is gentle and a large value of ζ will therefore force the boiling process towards an almost constant heat flux. This will also affect the pool area, which is shown in Fig 7.20a.

The reason for the shape of the evaporation rate curve (Fig. 7.20b) lies in the KFX model of heating up and evaporating of the liquid and the constant heat transfer coefficient. First there is a stage of an increase in the pool area and therefore also the total evaporation rate from it. Then, when the pool area has

stabilized at a steady state, the evaporation rate remains constant until most of the methane has evaporated. This is followed by a period where the energy transferred to the pool partly heats it up to the continually increasing boiling point and partly evaporates more methane, hence the overall evaporation rate decreases. When the temperature has increased to the boiling temperature of ethane, little energy goes to heating of the LNG and the total evaporation increases. After this increase, the pool area starts to decline and the evaporation rate concurrently decline towards zero.

There is no change in the boiling regime in this process since the heat transfer coefficient is constant. This makes the calculations decoupled from any physical effects regarding boiling regimes.

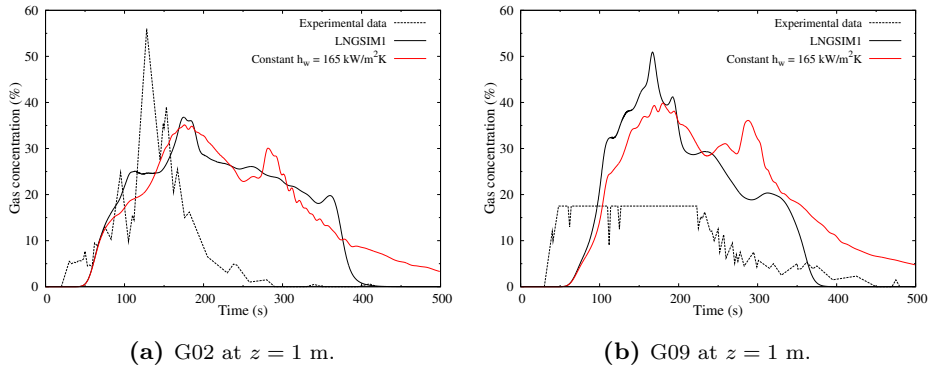


Figure 7.21: Simulations using constant h_w shows oscillations in gas concentrations at some of the nodes.

Because the constant value of h_w is chosen to be near the film boiling heat transfer coefficients calculated by LNGSIM1, the results become similar. An important thing to note from Fig. 7.21 is that using a constant heat transfer make the gas concentration struggle to reach a zero value. This happens as a consequence of h_w being constant, since the heat flux tends towards zero when the temperature difference does. In LNGSIM1 the heat transfer is increased towards the end of the LNG pool's life, a behavior that forces the concentrations to reach zero relatively quickly in accordance with the experimental data. Therefore, a constant h_w will produce an erroneous vapor cloud towards the end of a run.

Large values of ζ make the boiling process behave in the same way. This is previously noted in Sec. 7.6 and is further discussed in Sec. 7.10 where C_{SIM2} is combined with ζ .

As before, the concentrations oscillate less at the second tower array due to turbulent diffusion affecting the downstream gas concentrations. Since h_w is constant, it is easy to imagine the resulting concentration curves becoming smoother at the first array than when using LNGSIM1. However, Fig. 7.21 shows that this is clearly not the case. There are small oscillations in the gas concentrations general trend after the maximum concentration has been reached. This effect likely origins in numerical issues or rapid changes in the pool temperature or concentrations at

certain points, but a precise cause has not been found.

7.9.5 Increasing the heat transfer coefficient with a factor

To see how sensitive LNGSIM1 is to large increases in the heat transfer coefficient, simulations where it has been multiplied by factors of 10, 50 and 100 have been executed.

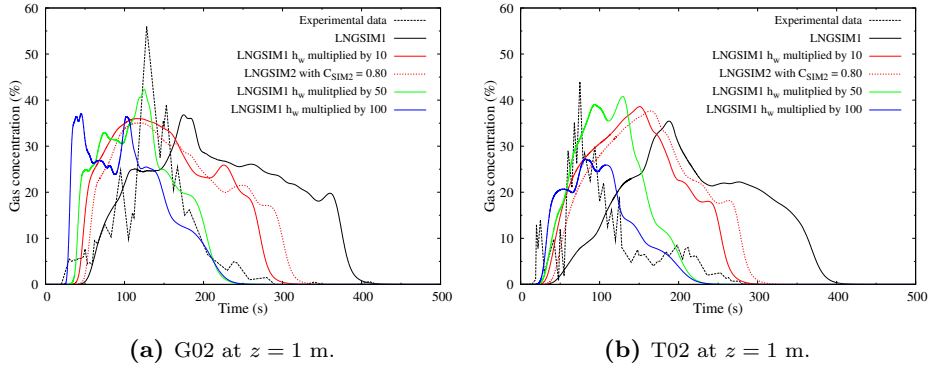


Figure 7.22: Results from multiplying h_w with various factors using LNGSIM1.

Figure 7.22 shows some results from these simulations. The effect of doing this is similar to the that of LNGSIM2; the heat flux is increased and the gas concentrations are thereby shifted earlier in time at all data nodes. Calculated concentration curves for a multiplication factor seems to resemble one of the curves for LNGSIM2 (also plotted in Fig. 7.22) in some cases. For example at T02 for $z = 1$ m, the multiplication factor of 10 makes the concentration curve very alike LNGSIM2 with $C_{SIM2} = 0.80$.

This is actually the general case; the emerging gas concentration curves when multiplying h_w with a factor of 10 resembles the ones of LNGSIM2 with $C_{SIM2} = 0.80$ with a slight time shift. The resemblance is clear at both $z = 1$ m and $z = 3$ m for all data nodes. This is an interesting result as it questions how good a model LNGSIM2 is, as multiplying the heat transfer coefficient produced by LNGSIM1 with a factor gives the same results. It is unknown which multiplication factors would fit other values of C_{SIM2} , or if any would, but 50 and 100 is not one of them.

The evaporation rates of multiplying the heat transfer coefficient of LNGSIM1 with 10 and LNGSIM2 with $C_{SIM2} = 0.80$ become similar as well, except that the LNGSIM2 run peaks at a later time and at a lot higher rate. This is a consequence of LNGSIM2 originally producing transition boiling fluxes more than one order of magnitude above LNGSIM1. The LNG pool area for the two simulations become quite different, however, an effect owing to the transient development of the evaporation rates.

Multiplying h_w with different factors does not seem to affect the overall results in any way. Neither of the chosen multiplication factors produce results that can be regarded as a lot better or worse than either LNGSIM1 or LNGSIM2.

7.9.6 Approximating LNG as pure methane

In the literature, it is sometimes suggested to approximate LNG as pure methane. Regarding this, one simulation using pure methane instead of the Burro 8 concentrations has been conducted. Fig. 7.23 shows the results from two nodes at the first tower array. At G02 (Fig. 7.23a), the concentration oscillates violently, even a lot more than the simulation with constant h_w did. At G09 the oscillations are similar to G02, otherwise they are like the ones at T02 (Fig. 7.23b). These oscillations are likely to occur from some numerical issues, which are currently unknown.

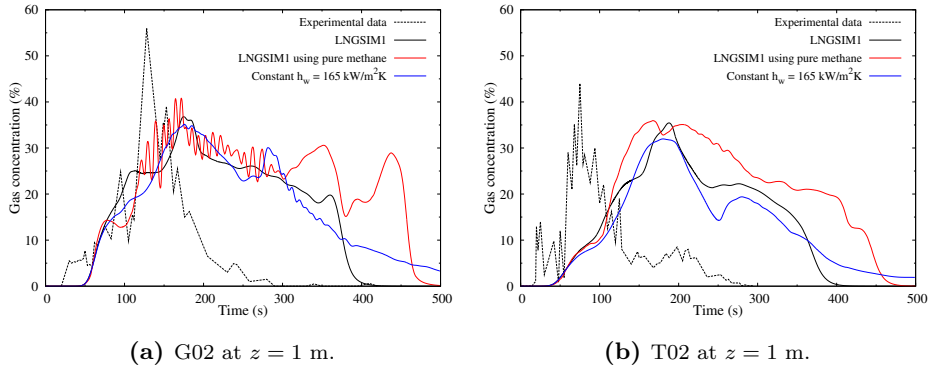


Figure 7.23: Results from approximating LNG as pure methane.

When approximating the LNG as pure methane, the boiling regime, the temperature driving force and the heat flux will remain constant throughout the entire run. The resulting boiling regime was always film boiling and the temperature difference and the heat flux were 168.4°C and 27.36 kW/m^2 , respectively, rendering h_w constant and 162.46 kW/m^2 . Drake, Jeje and Reid [26] observed experimentally that methane boiling on a solid surface at $\Delta T_w = 170^\circ$ gave heat fluxes of about 35 kW/m^2 and Bøe [8] found that methane boils in the stable film boiling regime. The results using pure methane for LGN are relatively good in this sense; the boiling regime is correct and the calculated heat flux is about 22% off for approximately the same temperature driving force.

In Ch. 3 it was found that methane boiling on water at 10°C resulted in $h_w = 25.74\text{ kW/m}^2$, which is about 6% away from the heat transfer coefficient of 27.36 kW/m^2 when using LNGSIM1. Considering the likelihood of difference in physical properties used, this is not too far off either.

Although h_w becomes constant for pure methane, the results are different from that of constant h_w with the Burro 8 composition (see Fig. 7.23), even though the heat transfer coefficients are practically the same (162.46 and 165 kW/m^2). There is a fundamental difference when the LNG consists of several components; the concentrations will change with time, making the pool temperature change with time as well due to changes in the boiling point. This makes the heat flux vary a lot, even though the heat transfer coefficient does not. Both LNGSIM1 with constant heat transfer coefficient and the concentrations from Burro 8 and LNGSIM1 with

pure methane, are more erroneous compared to the experimental than the regular LNGSIM1 is.

7.9.7 Roughness length

The average roughness length in the Burro test series was $205 \mu\text{m}$ [33]. This parameter is used to generate the wind profile and the given friction velocity has been used as a reference value to validate the inputs. The solid construction cells which represents the terrain in the Burro test series have not been initialized with a roughness scale, which might affect the vapor dispersion and thus the concentration at the data nodes. To check if this roughness scale influences the results to any extent, a simulation with the standard value for the roughness of 30 times the wind profile roughness length has been executed with LNGSIM1.

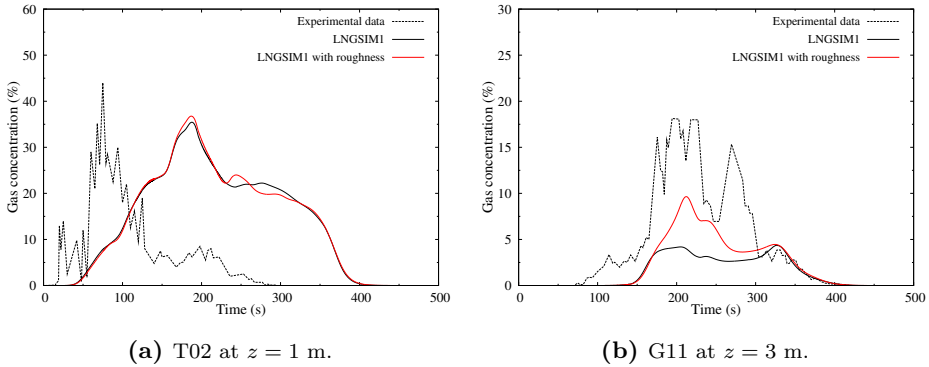


Figure 7.24: Effect of adding roughness to the solid construction cells.

Generally, the results with roughness are as shown in Fig. 7.24a. The surface roughness has little effect on the general trend of the concentrations in one point. There are deviations at some nodes, however, but these do not make the results any better or worse, except for the one in Fig. 7.24b. At this specific point, the added roughness has made the trend of the concentration profile follow the experimental data better. That G11 is at the outskirts of the second tower array, indicates the vapor cloud is somewhat affected by the roughness. The surface roughness will enhance the turbulence near the ground, which might lead to a wider and thicker gas cloud. Still, the overall results indicate that the surface roughness in general has little effect on the overall results.

7.10 Optimizing the heat transfer model

Analyses of LNGSIM2 for different values of $C_{\text{SIM}2}$ and LNGSIM1 for different values of ζ have been conducted in Secs. 7.5 and 7.6, respectively. This section explores how these factors can be combined in order to find an optimum model. To find the optimum combination of $C_{\text{SIM}2}$ and ζ , the resulting physical parameters from the simulations have to be as good as possible; the calculated pool area should

have a physically plausible value, the downstream gas concentrations should agree fairly well with experimental data and the change from film boiling to transition boiling should not occur at too low ΔT s.

In Sec. 7.5 it was concluded that values of $C_{\text{SIM}2}$ between 0.50 and 0.80 gave fair agreement with experimental data of downstream gas concentrations. A further analysis of the pool area calculations in Sec. 7.8 showed that the pool area of LNGSIM2 using $C_{\text{SIM}2} = 0.50$ and 0.60 made the heat transfer so large that the pool area became virtually zero. Furthermore, in Sec. 7.6 it was found that ζ -values in the range of 20 – 30 smoothed out some of the seemingly irregular maxima and minima in the concentration curves while not stretching the film boiling regime over a too long range of ΔT s. Therefore, the 18 combinations of $C_{\text{SIM}2} = 0.70, 0.75$ and 0.80 and $\zeta = 8, 10, 12, 20, 25$ and 30 have been chosen to investigate the combined effect of LNGSIM2 and ζ .

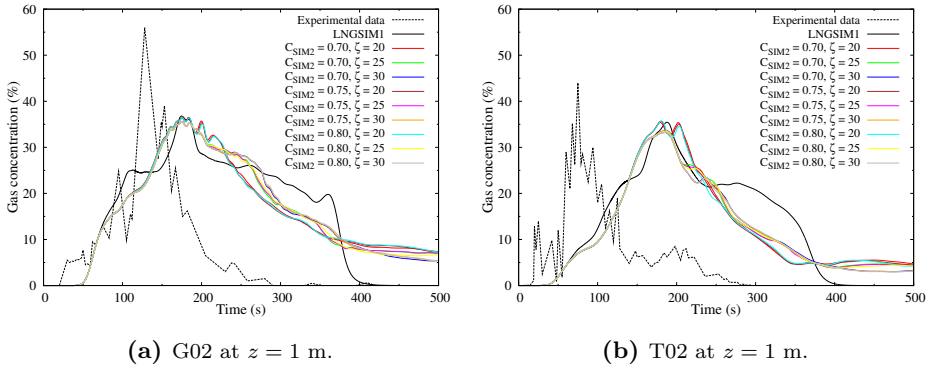


Figure 7.25: Simulations using combinations of $C_{\text{SIM}2}$ and ζ .

Figure 7.25 shows some results from the simulations using $C_{\text{SIM}2} = 0.70 - 0.80$ and $\zeta = 20 - 30$. There are two important things to note from these results:

1. The effect of ζ seems to be stronger than the one of $C_{\text{SIM}2}$, making the simulations for the same ζ -values, but different $C_{\text{SIM}2}$ -values follow each other closely.
2. As mentioned earlier, high values of ζ prevent the gas concentrations from reaching zero within the experimental time interval due to overall lower heat transfer coefficients. This unwanted effect is strongly present for $\zeta = 20 - 30$ when combined with LNGSIM2.

In other words, ζ between 20 and 30, combined with LNGSIM2, kills the effect of increased heat transfer wanted from $C_{\text{SIM}2}$. Therefore, $\zeta = 20 - 30$ are omitted from the further discussion.

For $\zeta = 8 - 12$, on the other hand, the effect of ζ becomes small enough so the gas concentrations do reach a zero value within reasonable times. In Fig. 7.26 it is clear, however, that $\zeta = 12$ makes the time interval of gas concentration readings the widest, followed by $\zeta = 10$ and $\zeta = 8$, regardless of the value of $C_{\text{SIM}2}$. Because

of this, $\zeta = 8$ provides the best matching to the experimental data of Burro 8 for both $C_{\text{SIM}2} = 0.70, 0.75$ and 0.80 .

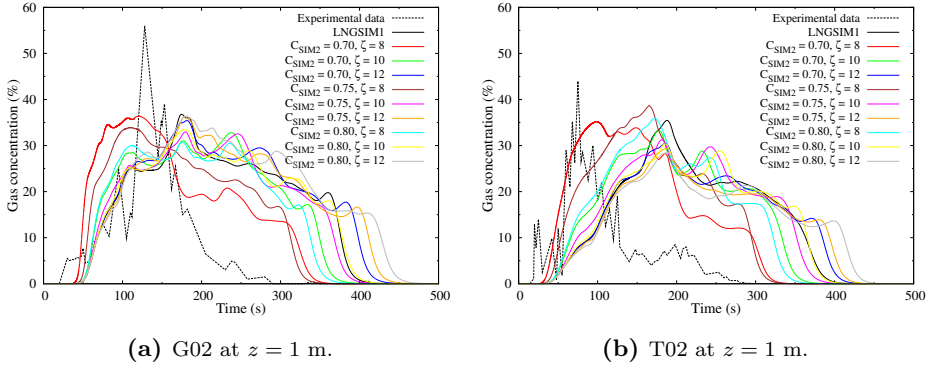


Figure 7.26: Simulations using combinations of $C_{\text{SIM}2}$ and ζ .

The results for LNGSIM2 with $C_{\text{SIM}2} = 0.70$ are in general fitting the experimental data better than when it is combined with $\zeta = 8$. This indicates that tuning of ζ might not be the right way to approach the issue of too high transition boiling heat fluxes. Furthermore, in Sec. 7.9.5 it was found that multiplying the heat transfer coefficients from LNGSIM1 by a factor of 10 gives approximately the same results as for LNGSIM2 with $C_{\text{SIM}2} = 0.80$, a result that questions the physical validity of LNGSIM2. Therefore, other means of calculating the heat transfer coefficient between water and LNG should be considered.

One such consideration is presented in Sec. 4.4. For mixtures, the heat transfer coefficient in nucleate boiling is smaller than for pure liquids, whereas in film boiling the opposite is true. If decent models are proposed and implemented for both nucleate boiling and film boiling of mixtures, it will alter the boiling curve a lot and likely increase the overall heat transfer compared to LNGSIM1. Such approach might capture the physics in boiling of mixtures better than LNGSIM2 does and still achieve the increased heat transfer that was originally aimed for.

When constructing a heat transfer model and validating the results against experimental data for downstream gas concentrations, it is important to take the effects the turbulence model imposes on the spreading into account. Even though the heat transfer model is perfect, the turbulence model might not be, thereby affecting the downstream concentrations. Therefore, the validation of the heat transfer model should be done concurrently with validation of dense gas dispersion.

8 Conclusions and further work

This chapter summarizes the main conclusions and results in this work and suggests further work to improve the heat transfer models in the future.

8.1 Conclusions

The analysis of the pool boiling correlations for pure liquids in Ch. 3 concluded that the way of calculating the transition boiling heat fluxes, Eqs. (A.10) – (A.12) [42], produces too high heat fluxes in that regime. Comparison with experimental data showed good agreement for pure methane, but not for pure ethane. Klimeko’s film boiling correlations, Eqs. (A.27) – (A.30) [24], were found to work as an average of the other film boiling correlations in App. A, and they were therefore chosen to calculate film boiling heat fluxes in the rest of the thesis. Other part conclusions from Ch. 3 are found in Sec. 3.4 on page 33.

Results from simulations using the two heat transfer models LNGSIM1 and LNGSIM2 are presented and discussed in Ch. 7. LNGSIM1 is based on pool boiling correlations for pure liquids and the use of mixture properties. The model is shown to produce downstream gas concentrations in the correct order of magnitude and often also correct trends through time. The concentration profiles are, however, sometimes shifted in time compared to the experimental data of the Burro test series. Results at the first tower array are worse than at the second, indicating that the model is inaccurate, since the results at the second array are heavily influenced by the turbulence model in KFX. Nevertheless, LNGSIM1 removes the requirement to state a constant heat transfer coefficient constant beforehand, which is a huge advantage over today’s KFX model.

When using a constant heat transfer coefficient with the Burro 8 concentrations, the resulting evaporation rates at later stages become too low, making the data nodes read hydrocarbon gas over a too long time interval. This occurs as a result of the LNG being heated up towards a continuously changing boiling point, thereby reducing the temperature driving force towards the end of the LNG pool’s life. When approximating the LNG as pure methane, on the other hand, the heat flux and the pool temperature remains constant throughout the entire run, since the pool does not get heated above the boiling point of methane. Both approaches render the downstream gas concentrations in quite some error and it is therefore not advised to do such simplifications.

Since LNGSIM1 was found unable to provide hydrocarbon vapor at the correct times, simulations using LNGSIM2 were conducted. LNGSIM2 takes the mixture

effect of a concentration boundary layer into account by modeling it through a constant, C_{SIM2} . This model was implemented to increase the heat transfer compared to LNGSIM1 by tuning C_{SIM2} , and thereby shift the concentration profiles in time. When using C_{SIM2} between 0.50 and 0.80, LNGSIM2 is found to give more accurate results than LNGSIM1. $C_{\text{SIM2}} = 0.50$ and 0.60 were found to produce unphysical small pool areas, however, and the range of $0.70 - 0.80$ was therefore chosen for more in-depth investigations. As for LNGSIM1, the results are in better agreement with experimental data farther downstream, due to the gas dispersion and the diffusion smoothing out the results.

Simulations where the calculated heat transfer coefficients from LNGSIM1 were multiplied by factors of 10, 50 and 100, showed that the factor of 10 produced approximately the same results as LNGSIM2 with $C_{\text{SIM2}} = 0.80$. This questions how good a model LNGSIM2 is, as it was supposed to include more physical effects through the concentration boundary layer. It is unknown, however, if any other multiplication factors would produce results similar to other values of C_{SIM2} and, if so, what they would be and which values of C_{SIM2} they would resemble.

In an attempt to further enhance LNGSIM2 through the conclusion that the calculated transition boiling heat fluxes are too large, ζ was introduced to tune the magnitude of the boiling curve's maximum point. The trade-off was a wider film boiling regime, thereby also reducing the overall heat transfer to the LNG pool. High ζ -values were found to tend toward results similar to those of a constant heat transfer coefficient. This happens because the film boiling regime becomes extremely wide, producing a nearly constant heat transfer coefficient throughout the entire run. Therefore, the ζ -values of 8, 10, 12, 20, 25 and 30 were chosen to be combined with LNGSIM2 for $C_{\text{SIM2}} = 0.70, 0.75$ and 0.80 .

These combinations clearly showed that the effect of large ζ -values completely override the effect from C_{SIM2} . The results fitting the experimental data best were the ones that used $\zeta = 8$. Clearly, this way of tuning the transition boiling regime is not the appropriate way to face the issue of too large transition boiling heat fluxes, thereby warranting new approaches. One such approach is to develop models for both nucleate boiling and film boiling of mixtures. Since the heat transfer coefficient in nucleate boiling of mixtures is lower than for pure liquids, and the one in film boiling is larger, this will alter the boiling curve a lot and decrease the heat transfer coefficients in the transition boiling regime. The overall heat transfer is likely to increase, however, hence such approach will produce similar effects to that of LNGSIM2, but with a more physical approach.

A study of rapid phase transitions has been performed as well. By using a simple criterion for when an RPT can happen [34], the hydrocarbon concentrations at these instances were logged. The results agree well with another theoretical study [1] in that the LNG has to age for some time before an RPT can occur. Even though the amount of times the RPT criterion is fulfilled is huge, nearly all occurrences are within the theoretical limit of [1], making the results encouraging. The occurrences of RPTs are always connected to a shift to the transition boiling regime and therefore also very large heat fluxes, both for LNGSIM1 and LNGSIM2, making the simple RPT criterion capture the physics of when and why RPTs occur

very well. Nevertheless, it is important to have in mind that the RPT criterion and the heat transfer calculations are completely decoupled.

8.2 Further work

In order to continue the work executed in this thesis, several things can be done:

- Develop and implement models for nucleate boiling and film boiling of mixtures. This will reduce the maximum point on the boiling curve as shown in Fig. 4.5 on page 42, thus removing the need to optimize ζ . Such change will alter the boiling curve a lot and full analyses with these changes must be performed.
- In this study, only experimental data from Burro 8 have been used as reference values. To further validate LNGSIM1, LNGSIM2 or any future heat transfer model, validation against more experimental data is required.
- The simulations show that the generated vapor clouds are too narrow compared to the real one. Therefore, further investigations into heavy gas dispersion should be carried out and validated against experimental data.
- The interaction between the heat transfer models and other KFX models should be investigated in more detail. For example, it is unknown how the model for heating up and evaporating the liquid pool performs with the rapid changes in the heat transfer coefficient.
- Analyze the numerical stability of the heat transfer models in more detail.
- Investigate steady state situations in more detail. Validate whether the liquid composition reach a steady situation for the different heat transfer models.

References

- [1] G.A. Melhem, S. Saraf, and H. Ozog. LNG Properties and Hazards: Understand LNG Rapid Phase Transition (RPT). Technical report, ioMosaic Corporation, 2006.
- [2] Ø. Myrmo. Numerical modeling of pool spreading, heat transfer and evaporation in liquefied naturals (LNG), December 2010.
- [3] C. Conrado and V. Vesovic. The influence of chemical composition on vaporisation of LNG and LPG on unconfined water surfaces. *Chemical Engineering Science*, 55:4549–4562, February 2000.
- [4] Y.A. Cengel. *Heat and Mass transfer - A Practical Approach*. McGraw-Hill, 2006.
- [5] J. Warnatz, U. Maas, and R.W. Dibble. *Combustion*. Springer-Verlag Berlin Heidelberg, 2006.
- [6] B.E. Poling, J.M. Prausnitz, and J.P. O’Connell. *The properties of gases and liquids*. McGraw-Hill, 5th edition, 2001.
- [7] D.E. Kautzky and J.W. Westwater. Film boiling of a mixture on a horizontal plate. *International Journal of Heat and Mass Transfer*, 10(2):253–256, 1967.
- [8] R. Bøe. Pool boiling of hydrocarbon mixtures on water. *International Journal of Heat and Mass Transfer*, 41:1003–1011, July 1997.
- [9] D.W. Schmitt. Heat Transfer in Boiling of Multicomponent Mixtures. *Chemical Engineering & Technology*, 10:242–248, 1987.
- [10] G. Taylor. The instability of liquid surfaces when accelerated in a direction perpendicular to their planes. I. *Mathematical and Physical Sciences*, 201, No. 1065:192–196, 1950.
- [11] D.J. Lewis. The instability of liquid surfaces when accelerated in a direction perpendicular to their planes. II. *Mathematical and Physical Sciences*, 202, No. 1068:81–96, 1950.
- [12] Yan-Po Chang. Wave Theory of Heat Transfer in Film Boiling. *Journal of Heat Transfer*, 81:1–12, 1959.
- [13] M.J. Moran and H.N. Shapiro. *Fundamentals of Engineering Thermodynamics*. John Wiley & Sons, Inc., 5th edition, 2006.
- [14] J.A. Valencia-Chavez and R.C. Reid. The Effect of Composition on the Boiling Rates of Liquefied Natural Gas for Condensed Spills on Water. *International Journal of Heat and Mass Transfer*, 22:831–838, 1979.

-
- [15] E.M. Drake, A.A. Jeje, and R.C. Reid. Transient Boiling of Liquefied Cryogens on a Water Surface. II. *International Journal of Heat and Mass Transfer*, 18:1369–1375, 1975.
- [16] I.J. Halvorsen. *Minimum Energy Requirements in Complex Distillation Arrangements*. PhD thesis, Norwegian University of Science and Technology, Faculty of Natural Sciences and Technology, 2001.
- [17] I.S. Ertesvåg. *Turbulent strøyming og forbrenning*. Tapir akademisk forlag, 2000.
- [18] B.E. Vembe, K.E. Rian, J.K. Holen, N.I. Lilleheie, B. Grimsmo, and T. Myhrvold. *Kameleon FireEx 2001 Theory Manual*. ComputIT AS, June 2001.
- [19] H.K. Versteeg and W. Malalasekera. *An Introduction to Computational Fluid Dynamics*. Pearson Education Limited, 2nd edition, 2007.
- [20] R.J. LeVeque. *Finite Volume Methods for Hyperbolic Problems*. Cambridge University Press, 2007.
- [21] National Institute of Standards and Technology. NIST chemistry webbook. <http://webbook.nist.gov/chemistry/>, 2011.
- [22] G.R. Somayajulu. A generalized equation for surface tension from the triple point to the critical point. *International Journal of Thermophysics*, 9:559–566, 1988.
- [23] W.M. Porteous and M. Blander. Limits of superheat and explosive boiling of light hydrocarbons, halocarbons, and hydrocarbon mixtures. *Advances in Chemical Engineering*, 21(3):560–566, 1975.
- [24] V.V. Klimenko. Film boiling on a horizontal plate - new correlation. *International Journal of Heat and Mass Transfer*, 24:69–79, February 1980.
- [25] P.J. Berenson. Film-Boiling Heat Transfer From a Horizontal Surface. *Journal of Heat Transfer*, 83:351–358, August 1961.
- [26] E.M. Drake, A.A. Jeje, and R.C. Reid. Transient Boiling of Liquefied Cryogens on a Water Surface. I. *International Journal of Heat and Mass Transfer*, 18:1361–1368, 1975.
- [27] J.R. Thome and R.A.W. Shock. Boiling of multicomponent liquid mixtures. *Advances in Heat Transfer*, 16:59 – 156, 1984.
- [28] P.L. Yue and M.E. Weber. Film boiling of saturated binary mixtures. *International Journal of Heat and Mass Transfer*, 16(10):1877–1888, 1973.
- [29] G. Vinayak Rao and A.R. Balakrishnan. Nucleate pool boiling heat transfer of multicomponent mixtures. *Chemical Engineering Research and Design*, A1(82):43–52, January 2004.

- [30] E. Marschall and L.L. Moresco. Analysis of binary film boiling. *International Journal of Heat and Mass Transfer*, 20:1013 – 1018, 1977.
- [31] P.L. Yue and M.E. Weber. Minimum film boiling flux of binary mixtures. *Trans. Instn Chem. Engrs*, 52:217–221, 1974.
- [32] H.C. Goldwire Jr., H.C. Rodean, R.T. Cederwall, E.J. Kansa, R.P. Koopman, J.W. McClure, T.G. McRae, L.K. Morris, L.M. Kamppinen, R.D. Kiefer, P.A. Urtiew, and C.D. Lind. Coyote series data report LLNL/NWC 1981 LNG spill tests dispersion, vapor burn, and rapid-phase-transition. Technical report, Lawrence Livermore Laboratory, October 1983.
- [33] R.P. Koopman, R.T. Cederwall, D.L. Ermak, H.C. Goldwire Jr., W.J. Hogan, J.W. McClure, T.G. McRae, D.L. Morgan, H.C. Rodean, and J.H. Shinn. Analysis of burro series 40-m³ LNG spill experiments. *Journal of Hazardous Materials*, 6:43–83, 1982.
- [34] W.M. Porteous and R.C. Reid. Light hydrocarbon vapor explosions. *Chemical Engineering Progress*, 72:83–89, 1976.
- [35] T.A. Cavanaugh, J.H. Siegell, and K.W. Steinberg. Simulation of vapor emissions from liquid spills. *Journal of Hazardous Materials*, 38(1):41 – 63, 1994.
- [36] G. Opschoor. The spreading and evaporation of LNG- and burning LNG-spills on water. *Journal of Hazardous Materials*, 3(3):249 – 266, 1980.
- [37] A.W. Vikan. Numerisk modellering av dam-spredning, varmeoverføring og brann i flytende naturgass (LNG). Master’s thesis, Norwegian University of Science and Technology, Faculty of Engineering Science and Technology, June 2009.
- [38] N.I. Lilleheie. *Extended Shallow-Layer Pool Model in KFX 2010 LNG*. ComputIT AS, January 2011.
- [39] A.M. Thyer. A review of data on spreading and vaporisation of cryogenic liquid spills. *Journal of Hazardous Materials*, A99:31–40, 2003.
- [40] R.P. Koopman, J. Baker, R.T. Cederwall, H.C. Goldwire Jr., W.J. Hogan, L.M. Kamppinen, R.D. Kiefer, J.W. McClure, T.G. McRae, D.L. Morgan, L.K. Morris, M.W. Spann Jr., and C.D. Lind. Burro series data report llnl/nwc 1980 LNG spill tests. Technical report, Lawrence Livermore Laboratory, 1982.
- [41] M.Z. Jacobson. *Fundamentals of Atmospheric Modeling*. Cambridge University Press, 2nd edition, 2005.
- [42] E.K. Kalinin, I.I. Berlin, V.V. Kostyuk, and E.M. Nosova. Heat Transfer in Transition Boiling of Cryogenic Liquids. *Advances in Cryogenic Engineering*, 21:273–277, 1975.
- [43] N. Zuber. *Hydrodynamic Aspects of Boiling Heat Transfer*. PhD thesis, University of California, June 1959. United States Atomic Energy Commission.

-
- [44] D.W. Hissong. Keys to modeling LNG spills on water. *Journal of Hazardous Materials*, 140(3):465 – 477, 2007.
- [45] T.D. Hamill and K.J. Baumeister. Film boiling heat transfer from a horizontal surface as an optimal boundary value process. Technical report, American Institute of Chemical Engineers, August 1966.
- [46] T.H.K. Frederking, Y.C. Wu, and B.W. Clement. Effects of Interfacial Instability on Film Boiling of Saturated Liquid Helium I Above a Horizontal Surface. *Advances in Chemical Engineering*, 12:238–244, March 1966.

A Heat transfer correlations for pool boiling of pure liquids

This appendix lists correlations for pool boiling of pure liquids found in a previous study [2]. By having the various boiling regimes given in Fig. 2.3 on page 7 in mind, the insight into the following formulas may be enhanced.

A.1 Nucleate boiling heat transfer

For nucleate boiling heat transfer Kalinin et al. [42] suggest using an empirical formula by Grigoryev et al.¹:

$$\dot{q}_n = \frac{4.1 \left[1 + 10 \left(\frac{\rho_v}{\rho_l - \rho_v} \right)^{2/3} \right]^3 \Delta T_w^3}{\sigma T_s \left[\frac{\sqrt{v_l}}{K_l} + \frac{10}{\sqrt{\rho_w c_{pw} K_w}} \right]^2 \left(1 + \frac{10}{\gamma} \right)}. \quad (\text{A.1})$$

A.1.1 Limits for sustaining bubbles in nucleate boiling

The superheat needed to maintain bubbles created at the heater surface can be found by utilizing Clapeyron's equation,

$$\left(\frac{dp}{dT} \right)_s = \frac{h_{fg}}{T(v_v - v_l)}, \quad (\text{A.2})$$

and assume ideal gas behavior and $v_v \gg v_l$. It can then be shown that the superheating of the vapor needed to sustain a bubble is given by

$$T_v - T_s = \frac{2R_u T_s^2 \sigma}{h_{fg} M_v p_v R}. \quad (\text{A.3})$$

The vapor pressure needed to sustain the bubble can be found by the force balance

$$\pi R^2 (p_v - p_l) = 2\pi R \sigma, \quad (\text{A.4})$$

which gives

$$p_v - p_l = \frac{2\sigma}{R}. \quad (\text{A.5})$$

¹V.A. Grigorev, Yu.M. Pavlov & E.V. Ametistov, *Teplotenergetika* (Thermal Engineering), 1973, 9:57-63

Eqs. (A.3) and (A.5) thus give the vapor pressure and temperature needed for a bubble to exist in nucleate boiling. Superheating of the liquid in nucleate boiling implies that a small temperature boundary layer is established.

A.2 Critical heat flux

The critical heat flux is the maximum heat flux obtained in the nucleate boiling regime before the bubble formation rate becomes so high that the heat flux is reduced by the emerging vapor film. This is visualized by point C in Fig. 2.3 on page 7. Zuber [43] derived an interval in which the critical heat flux must be:

$$\begin{aligned} 0.157h_{fg}\rho_v \left[\frac{\sigma g(\rho_l - \rho_v)}{\rho_v^2} \right]^{1/4} \left[\frac{\rho_l}{\rho_l + \rho_v} \right]^{1/2} &\geq \dot{q}_{cr} \\ &\geq 0.120h_{fg}\rho_v \left[\frac{\sigma g(\rho_l - \rho_v)}{\rho_v^2} \right]^{1/4} \left[\frac{\rho_l}{\rho_l + \rho_v} \right]^{1/2}. \end{aligned} \quad (\text{A.6})$$

Another correlation used for the critical heat flux is the Kutateladze formulation [4, 42]

$$\dot{q}_{cr} = 0.16h_{fg}\sqrt{\rho_v}[\sigma g(\rho_l - \rho_v)]^{1/4} \quad (\text{A.7})$$

where the constant 0.16 is tuned to experimental data. Hissong [44]¹ uses Eq. (A.7) and another correlation,

$$\dot{q}_{cr} = 0.18 \frac{h_{fg}\rho_v [\sigma g(\rho_l - \rho_v)]^{1/4}}{1 + 2\sqrt{\frac{\rho_v}{\rho_l} + \frac{\rho_v}{\rho_l}}} \sqrt{\frac{\rho_l - \rho_v}{\rho_l\rho_v}}, \quad (\text{A.8})$$

for the critical heat flux and suggests using the smallest of those. The critical temperature difference can be calculated by rearranging Eq. (A.1) to

$$\Delta T_{cr} = 0.625 [\dot{q}_{cr}\sigma T_s]^{1/3} \frac{\left[\frac{\sqrt{\nu_l}}{K_l} + \frac{10}{\sqrt{\rho_w c_{pw} K_w}} \right]^{2/3} \left(1 + \frac{10}{\gamma} \right)^{1/3}}{\left[1 + 10 \left(\frac{\rho_v}{\rho_l - \rho_v} \right)^{2/3} \right]} \quad (\text{A.9})$$

and insert either of Eqs. (A.6) – (A.8) for \dot{q}_{cr} .

A.3 Transition boiling heat transfer

Transition boiling is the least understood boiling regime and is usually modeled as a mixture between nucleate and film boiling. Such mindset is utilized by Kalinin et al. [42]; they extrapolated heat flux correlations for the nucleate and film boiling regime, Eqs. (A.1) and (A.26) into the transition boiling regime and used a fraction

¹Hissong refers to P.J. Waite, R.J. Whitehouse, E.B. Winn, *The spread and vaporization of cryogenic liquids on water*, Journal of Hazardous Materials, 8 (1983) 165-184 for Eqs. (A.7) and (A.8).

ξ to describe how much of the boiling process is the nucleate boiling regime (see Fig. 2.3 on page 7). Then it is possible to calculate the transition boiling heat flux by

$$\dot{q}_t = \dot{q}_n \xi + \dot{q}_f (1 - \xi). \quad (\text{A.10})$$

To calculate ξ Kalinin et al. suggest to use a dimensionless temperature, defined as

$$\Delta T^* = \frac{\Delta T_w - \Delta T_{\text{cr}}}{\Delta T_{\text{min}} - \Delta T_{\text{cr}}}, \quad (\text{A.11})$$

together with either of the empirical formulas

$$\xi = (1 - \Delta T^*)^7 \quad (\text{A.12})$$

and

$$\xi = e^{-9.2\Delta T^*}. \quad (\text{A.13})$$

The way to calculate q_t can then be summarized as:

1. Calculate ΔT_{cr} with Eq. (A.7) in Eq. (A.1).
2. Calculate ΔT_{min} from Eq. (A.17) or (A.18).
3. Calculate ΔT^* from Eq. (A.11). ΔT_w is given by the problem.
4. Calculate ξ from either Eq. (A.13) or (A.12).
5. Calculate \dot{q}_t with Eq. (A.10) using any film boiling correlation (Eqs. (A.27) – (A.30) are used in this thesis).
Eq. (A.1) and Eq. (A.16), (A.23) or (A.26).

A.4 Minimum heat flux

At the point where the heater surface is fully covered by a vapor film, the boiling regime is said to change from transition boiling to film boiling. This particular point is called the minimum point or Leidenfrost point in the boiling curve (point D on Fig. 2.3 on page 7).

Several correlations have been developed for both the heat flux, the temperature difference and the heat transfer coefficient at the Leidenfrost point. An early attempt by Zuber [43] in his doctoral thesis resulted in the following correlation for the minimum heat flux:

$$\dot{q}_{\text{min}} = 0.177 h_{\text{fg}} \rho_v \left[\frac{\sigma g (\rho_l - \rho_v)}{(\rho_l + \rho_v)^2} \right]^{1/4}. \quad (\text{A.14})$$

Berenson [25] used 0.09 in Eq. (A.14), instead of 0.177, to match experimental data for n-pentane and carbon tetrachloride ($T_{\text{boil}} = 36^\circ\text{C}$ and 76°C , respectively). Eq. (A.14) is developed for the first stage of a perturbation affecting the liquid-vapor interface (i.e. until the amplitude of the disturbance has reached 0.4λ [11]). For the last (third) stage of the instability process (i.e. when the vapor penetrates

the liquid and accelerates upwards with a velocity proportional to $\sqrt{a-g}$, Zuber [43] established the following interval in which the minimum heat flux must be:

$$0.109h_{fg}\rho_v \left[\frac{\sigma g(\rho_l - \rho_v)}{\rho_l^2} \right]^{1/4} \leq \dot{q}_{min} \leq 0.144h_{fg}\rho_v \left[\frac{\sigma g(\rho_l - \rho_v)}{\rho_l^2} \right]^{1/4}. \quad (\text{A.15})$$

Berenson [25] established both a correlation for the heat transfer coefficient,

$$h_{min} = 0.425 \left[\frac{K_v^3 h'_{fg} \rho_v g(\rho_l - \rho_v)}{\mu_v \Delta T_{min} \sqrt{\frac{\sigma}{g(\rho_l - \rho_v)}}} \right]^{1/4}, \quad (\text{A.16})$$

and for the temperature difference at the Leidenfrost point:

$$\Delta T_{min} = 0.127 \frac{\rho_{vf} h'_{fg}}{K_{vf}} \left[\frac{g(\rho_l - \rho_v)}{\rho_l + \rho_v} \right]^{2/3} \left[\frac{\sigma}{g(\rho_l - \rho_v)} \right]^{1/2} \left[\frac{\mu_{vf}}{\rho_l - \rho_v} \right]^{1/3}. \quad (\text{A.17})$$

Kalinin *et al.* [42], on the other hand, suggest the use of the relation

$$\Delta T_{min} = (T_c - T_s) \left[0.16 + \frac{2.4}{\gamma^2} \right] \quad (\text{A.18})$$

for the minimum temperature difference, where subscript *c* refers to the critical point (triple point).

A.5 Film boiling heat transfer

Beyond the Leidenfrost point (to the right of point D in Fig. 2.3 on page 7) the vapor film covers the whole heater surface. The heat transfer to the boiling liquid has decreased a lot compared to nucleate boiling due to the vapor film acting as a thermal shield. This boiling regime is therefore usually avoided in industrial applications where high heat fluxes are desired.

In 1959 Chang released the wave theory for film boiling where the Nusselt number was found to be:

$$\text{Nu} = 0.234(\text{Pr}^* \text{Gr}^*)^{1/3}. \quad (\text{A.19})$$

Eq. (A.19) has the same form as a Nusselt number for natural convection [12]. The generalized Prandtl number and Grashof number are defined by

$$\text{Pr}^* = \frac{\nu_v}{\alpha_e} = \text{Pr} \left(\frac{2h_{fg}}{c_{pv} \Delta T_v} \right) \quad (\text{A.20})$$

and

$$\text{Gr}^* = \frac{g \rho_v^2 L^3}{\mu_v^2} \frac{\rho_l - \rho_v}{\rho_v}. \quad (\text{A.21})$$

The equivalent thermal diffusivity is given by

$$\alpha_e = \frac{K_v \Delta T_w}{2h_{fg}\rho_v}. \quad (\text{A.22})$$

Hamill and Baumeister [45] approached the problem by assuming that the film boiling process realizes the maximum heat transfer and therefore the maximum entropy production. The expression for the film boiling heat transfer coefficient is found to be

$$h_f = 0.410 \left[\frac{K_{vf}^3 h_{fg}'' \rho_{vf} g(\rho_l - \rho_{vf})}{\mu_{vf} \Delta T_w \sqrt{\frac{\sigma}{g(\rho_l - \rho_{vf})}}} \right]^{1/4}. \quad (\text{A.23})$$

Frederking, Wu and Clement [46] described four extreme possibilities in film boiling: laminar vapor film and regularly distributed vapor cells, turbulent vapor film and regularly distributed vapor cells, laminar vapor film and randomly distributed vapor cells and turbulent vapor film and randomly distributed vapor cells. The two last possibilities are found to approximate film boiling heat transfer by

$$\dot{q}_f = 0.20 (K_{vf} \Delta T_w)^{2/3} \left[\frac{g(\rho_l - \rho_{vf}) \rho_{vf} h_{fg}'}{\mu_{vf}} \right]^{1/3} \quad (\text{A.24})$$

and

$$\dot{q}_f = 0.30 \left(\frac{K_{vf} \Delta T_w g(\rho_l - \rho_{vf})}{\rho_{vf}} \right)^{1/3} \left(\rho_{vf} h_{fg}' \right)^{2/3}, \quad (\text{A.25})$$

respectively. The physical properties with subscript vf in Eqs. (A.24) and (A.25) are evaluated at the arithmetic mean vapor film temperature.

Kalinin *et al.* [42] use an expression developed by themselves for the film boiling regime:

$$\dot{q}_f = 0.18 K_{vf} \Delta T_w \left[\frac{g}{\nu_{vf} \alpha_{vf}} \left(\frac{\rho_l}{\rho_{vf}} - 1 \right) \right]^{1/3}. \quad (\text{A.26})$$

With all the various expressions for the film boiling regime above, Klimenko [24] tried to merge all of them into a more compact form. The laminar region, $\text{Ga} [(\rho_l/\rho_{vf}) - 1] < 10^8$, is described by

$$\text{Nu} = 0.19 \left[\text{Ga} \left(\frac{\rho_l - \rho_{vf}}{\rho_{vf}} \right) \right]^{1/3} \text{Pr}^{1/3} \cdot f_1 \left(\frac{h_{fg}}{c_{p,vf} \Delta T_w} \right) \quad (\text{A.27})$$

where

$$f_1 = \begin{cases} 1 & \text{if } \frac{h_{fg}}{c_{p,vf} \Delta T_w} \leq 1.4 \\ 0.89 \left(\frac{h_{fg}}{c_{p,vf} \Delta T_w} \right)^{1/3} & \text{if } \frac{h_{fg}}{c_{p,vf} \Delta T_w} > 1.4 \end{cases} \quad (\text{A.28})$$

and the turbulent region, $\text{Ga} [(\rho_l/\rho_v) - 1] > 10^8$, is described by

$$\text{Nu} = 0.0086 \left(\text{Ga} \frac{\rho_l - \rho_{vf}}{\rho_{vf}} \right)^{1/2} \text{Pr}^{1/3} \cdot f_2 \left(\frac{h_{fg}}{c_{p,vf} \Delta T_w} \right) \quad (\text{A.29})$$

where

$$f_2 = \begin{cases} 1 & \text{if } \frac{h_{fg}}{c_{pvf}\Delta T_w} \leq 2.0 \\ 0.71 \left(\frac{h_{fg}}{c_{pvf}\Delta T_w} \right)^{1/2} & \text{if } \frac{h_{fg}}{c_{pvf}\Delta T_w} > 2.0 \end{cases} \quad (\text{A.30})$$

The functions f_1 and f_2 can be regarded as friction at the vapor-liquid interface. Ga is the Galileo number, defined as

$$\text{Ga} = \frac{g\lambda_{\text{crit}}^3}{\nu^2}. \quad (\text{A.31})$$

Thermal properties of vapor are calculated at $T_v = T_s + 0.5\Delta T_w$.

B Physical properties of selected fluids at T_{boil}

This appendix lists physical properties of the hydrocarbons selected for calculations in Ch. 3 at their boiling point. All data is collected from [21] except for surface tension which is calculated from the equation [22]

$$\sigma = C_1 T_\sigma^{5/4} + C_2 T_\sigma^{9/4} + C_3 T_\sigma^{13/4}, \quad (\text{B.1})$$

where T_σ is a reduced temperature, defined as

$$T_\sigma = \frac{T_c - T}{T_c}. \quad (\text{B.2})$$

C_1 , C_2 and C_3 are fluid specific constants given in [22]. The resulting dimensions of σ in Eq. (B.1) are $\frac{\text{dynes}}{\text{cm}} = 10^{-3} \frac{\text{N}}{\text{m}}$.

B.1 Physical properties of methane

Table B.1: Physical properties of methane at 111.0 K [21].

P (kPa)	ρ ($\frac{\text{kg}}{\text{m}^3}$)	c_p ($\frac{\text{kJ}}{\text{kgK}}$)	μ ($\frac{\text{kg}}{\text{ms}}$)	K ($\frac{\text{W}}{\text{mK}}$)	h ($\frac{\text{kJ}}{\text{kg}}$)	Phase
60	1.0657	2.1544	0.00000443	0.011359	512.04	Vapor
70	1.2480	2.1697	0.00000443	0.011392	511.4	Vapor
80	1.4318	2.1856	0.00000443	0.011428	510.76	Vapor
90	1.6170	2.2023	0.00000443	0.011466	510.1	Vapor
96.874	1.7266	2.2126	0.00000443	0.011489	509.71	Vapor
96.874	423.33	3.4763	0.00011857	0.1848	-2.3293	Liquid
100	423.33	3.4762	0.00011857	0.1848	-2.3233	Liquid
110	423.34	3.4761	0.00011859	0.1841	-2.3088	Liquid
120	423.35	3.476	0.0001186	0.18483	-2.2942	Liquid
130	423.36	3.4759	0.00011862	0.18484	-2.2796	Liquid

$$T_c = 190.6 \pm 0.3 \text{ K}, p_c = 46.1 \pm 0.3 \text{ bar}$$

$$T_{\text{SL}} = 165.5 \text{ K}^a$$

$$T_{\text{boil}} = 111 \pm 2 \text{ K}$$

$$h_{\text{fg}} = 511.94293 \frac{\text{kJ}}{\text{kg}}$$

$$M = 16.0425 \frac{\text{kg}}{\text{kmol}}$$

$$C_1 = 30.8936, C_2 = 24.9105, C_3 = -6.8276$$

$$\sigma = 0.0135 \frac{\text{N}}{\text{m}}^b$$

^a Data from reference [23], $p = 1 \text{ atm}$.

^b Calculated by Eq. (B.1).

B.2 Physical properties of ethane

Table B.2: Physical properties of ethane at 184.6 K [21].

P (kPa)	ρ ($\frac{\text{kg}}{\text{m}^3}$)	c_p ($\frac{\text{kJ}}{\text{kgK}}$)	μ ($\frac{\text{kg}}{\text{ms}}$)	K ($\frac{\text{W}}{\text{mK}}$)	h ($\frac{\text{kJ}}{\text{kg}}$)	Phase
70	1.4032	1.3598	0.00000588	0.0093952	490.88	Vapor
80	1.6091	1.3539	0.00000588	0.0094227	490.44	Vapor
90	1.8163	1.347	0.00000588	0.0094504	490.01	Vapor
100	2.0251	1.339	0.00000589	0.0094784	489.59	Vapor
101.59	2.0584	1.3377	0.00000589	0.0094829	489.52	Vapor
101.59	543.91	2.4266	0.00016645	0.16709	0.11646	Liquid
110	543.91	2.4265	0.00016646	0.1671	0.12528	Liquid
120	543.92	2.4265	0.00016648	0.1671	0.13577	Liquid
130	543.93	2.4264	0.00016649	0.16711	0.14626	Liquid
140	543.94	2.4263	0.00016651	0.16712	0.15675	Liquid

$$T_c = 305.3 \pm 0.3 \text{ K}, p_c = 49.0 \pm 1.0 \text{ bar}$$

$$T_{\text{SL}} = 269.7 \text{ K}^a$$

$$T_{\text{boil}} = 184.6 \pm 0.6 \text{ K}$$

$$h_{\text{fg}} = 489.40354 \frac{\text{kJ}}{\text{kg}}$$

$$M = 30.0690 \frac{\text{kg}}{\text{kmol}}$$

$$C_1 = 53.6025, C_2 = -7.6050, C_3 = 3.0714$$

$$\sigma = 0.0160 \frac{\text{N}}{\text{m}}^b$$

^a Data from reference [23], $p = 1 \text{ atm}$.

^b Calculated by Eq. (B.1).

B.3 Physical properties of propane

Table B.3: Physical properties of propane at 231.1 K [21].

P (kPa)	ρ ($\frac{\text{kg}}{\text{m}^3}$)	c_p ($\frac{\text{kJ}}{\text{kgK}}$)	μ ($\frac{\text{kg}}{\text{ms}}$)	K ($\frac{\text{W}}{\text{mK}}$)	h ($\frac{\text{kJ}}{\text{kg}}$)	Phase
70	1.6473	1.4212	0.00000633	0.011592	527.61	Vapor
80	1.8898	1.4269	0.00000632	0.011586	527.11	Vapor
90	2.1342	1.4328	0.00000632	0.01158	526.6	Vapor
100	2.3806	1.4389	0.00000631	0.011575	526.08	Vapor
101.62	2.4208	1.4399	0.00000631	0.011574	525.99	Vapor
101.62	580.85	2.2532	0.00019715	0.12917	100.14	Liquid
110	580.86	2.2532	0.00019717	0.12918	100.15	Liquid
120	580.87	2.2531	0.00019719	0.12919	100.16	Liquid
130	580.89	2.2531	0.00019721	0.12919	100.17	Liquid
140	580.9	2.253	0.00019723	0.1292	100.18	Liquid

$$T_c = 369.9 \pm 0.2 \text{ K}, p_c = 42.5 \pm 0.1 \text{ bar}$$

$$T_{\text{SL}} = 328.5 \text{ K}^a$$

$$T_{\text{boil}} = 231.1 \pm 0.2 \text{ K}$$

$$h_{\text{fg}} = 425.85 \frac{\text{kJ}}{\text{kg}}$$

$$M = 44.0956 \frac{\text{kg}}{\text{kmol}}$$

$$C_1 = 55.1756, C_2 = -7.8600, C_3 = 2.1428$$

$$\sigma = 0.0154 \frac{\text{N}}{\text{m}}^b$$

^a Data from reference [23], $p = 1 \text{ atm}$.

^b Calculated by Eq. (B.1).

B.4 Physical properties of butane

Table B.4: Physical properties of butane at 273.0 K [21].

P (kPa)	ρ ($\frac{\text{kg}}{\text{m}^3}$)	c_p ($\frac{\text{kJ}}{\text{kgK}}$)	μ ($\frac{\text{kg}}{\text{ms}}$)	K ($\frac{\text{W}}{\text{mK}}$)	h ($\frac{\text{kJ}}{\text{kg}}$)	Phase
70	1.8439	1.6235	0.00000678	0.014182	586.87	Vapor
80	2.1163	1.6293	0.00000677	0.01418	586.32	Vapor
90	2.3911	1.6352	0.00000677	0.014178	585.77	Vapor
100	2.6685	1.6413	0.00000677	0.014176	585.21	Vapor
102.64	2.7422	1.643	0.00000676	0.014175	585.06	Vapor
102.64	600.89	2.3112	0.00020279	0.11538	199.65	Liquid
110	600.9	2.3111	0.00020281	0.11538	199.66	Liquid
120	600.92	2.3111	0.00020283	0.11539	199.67	Liquid
130	600.93	2.311	0.00020286	0.11539	199.68	Liquid
140	600.94	2.311	0.00020288	0.1154	199.68	Liquid

$$T_c = 425 \pm 1 \text{ K}, p_c = 38.0 \pm 0.1 \text{ bar}$$

$$T_{\text{SL}} = 378.3 \text{ K}^a$$

$$T_{\text{boil}} = 273 \pm 1 \text{ K}$$

$$h_{\text{fg}} = 385.41 \frac{\text{kJ}}{\text{kg}}$$

$$M = 58.1222 \frac{\text{kg}}{\text{kmol}}$$

$$C_1 = 55.0822, C_2 = -2.5019, C_3 = -3.7758$$

$$\sigma = 0.0149 \frac{\text{N}}{\text{m}}^b$$

^a Data from reference [23], $p = 1 \text{ atm}$.

^b Calculated by Eq. (B.1).

B.5 Physical properties of the vapor film

Table B.5: Physical properties of the vapor film in film boiling [21]. Data are evaluated at the mean temperature difference between the hot surface and the liquid-vapor interface.

	$\rho_{\text{vf}} \left(\frac{\text{kg}}{\text{m}^3} \right)$	$c_{p,\text{vf}} \left(\frac{\text{kJ}}{\text{kgK}} \right)$	$\mu_{\text{vf}} \left(\frac{\text{kg}}{\text{ms}} \right)$	$K_{\text{vf}} \left(\frac{\text{W}}{\text{mK}} \right)$
Methane (197 K)	0.95493	2.1045	0.0000076992	0.021588
Ethane (234 K)	1.5959	1.5358	0.0000074238	0.013779
Propane (257 K)	2.1528	1.5251	0.0000070273	0.014025
Butane (273 K)	2.7422	1.643	0.0000067600	0.014175

C Thermodynamic properties of mixtures

It is usually tempting to use either a weight or mole fraction averaged quantity when dealing with mixtures. For specific heat capacity, for example, such approach is physically correct. For surface tension, viscosity and thermal conductivity, on the other hand, this is not necessarily the case. This appendix lists some simple correlations to estimate different physical properties for mixtures.

An adequate approximation for the superheat limit of a mixture is to use the mole weight averaged quantity

$$T_{\text{SL,mix}} = \sum_i X_i T_{\text{SL}i} \quad (\text{C.1})$$

for liquid mixtures and

$$T_{\text{SL,mix}} = \sum_i Y_i T_{\text{SL}i} \quad (\text{C.2})$$

for vapor mixtures [23]. To calculate the mixture value for h_{fg} the simple relation

$$h_{\text{fg,mix}} = \sum_i X_i h_{\text{fg}i} \quad (\text{C.3})$$

is used.

C.1 Thermodynamic properties of liquid mixtures

The mass density of a liquid mixture is calculated by:

$$\rho_{\text{mix}} = \frac{1}{v_{\text{mix}}} = \frac{1}{\sum_i X'_i v_i} = \frac{1}{\sum_i \frac{X'_i}{\rho_i}}. \quad (\text{C.4})$$

The specific heat capacity of a liquid mixture is estimated by the mass fraction averaged quantity:

$$c_{p,\text{mix}} = \sum_i X'_i c_{pi}. \quad (\text{C.5})$$

The surface tension of a hydrocarbon liquid mixture can be approximated by the mole fraction averaged quantity [6]:

$$\sigma_{\text{mix}} = \sum_i X_i \sigma_i. \quad (\text{C.6})$$

The thermal conductivity of a liquid mixture is usually less than the weight or mole fraction averaged quantity. Deviations are often small, however, so an approximation to the thermal conductivity of a liquid mixture is [6]:

$$K_{\text{mix}} = \sum_i X'_i k_i. \quad (\text{C.7})$$

The viscosity of a liquid mixture is an uncertain quantity because it is heavily dependent on the molecules involved. A small dilution of a pure substance may therefore change the viscosity drastically [6]. To keep it simple, however, this work uses the mole fraction averaged quantity as an approximation:

$$\mu_{\text{mix}} = \sum_i X_i \mu_i. \quad (\text{C.8})$$

C.2 Thermodynamic properties of vapor mixtures

The ideal gas relation for the density of component i in a vapor mixture is given by:

$$\rho_i = \frac{p_i M_i}{R_u T}. \quad (\text{C.9})$$

The mass density of a vapor mixture is calculated by:

$$\rho_{\text{mix}} = \frac{1}{v_{\text{mix}}} = \frac{1}{\sum_i Y'_i v_i} = \frac{1}{\sum_i \frac{Y'_i}{\rho_i}}. \quad (\text{C.10})$$

The specific heat capacity of a vapor mixture is estimated by the mass fraction averaged quantity:

$$c_{p,\text{mix}} = \sum_i Y'_i c_{pi}. \quad (\text{C.11})$$

The surface tension of a hydrocarbon vapor mixture can be approximated in the same manner as for a liquid mixture [6]:

$$\sigma_{\text{mix}} = \sum_i Y_i \sigma_i. \quad (\text{C.12})$$

The thermal conductivity of a vapor mixture can be approximated by the following equation within an error of $\pm 10 - 20\%$ [5]:

$$K_{\text{mix}} = \frac{1}{2} \left[\sum_i Y_i k_i + \left(\sum_i \frac{Y_i}{k_i} \right)^{-1} \right]. \quad (\text{C.13})$$

The viscosity of a vapor mixture can be approximated in the same manner as the thermal conductivity within an error of $\pm 10\%$ [5]:

$$\mu_{\text{mix}} = \frac{1}{2} \left[\sum_i Y_i \mu_i + \left(\sum_i \frac{Y_i}{\mu_i} \right)^{-1} \right]. \quad (\text{C.14})$$

